Adhesion and Adsorption Energetics of Late Transition Metal Nanoparticles on Oxide and Carbon Supports for Predicting Catalyst Behavior and Enabling Catalyst Design

Nida Janulaitis

A dissertation

submitted in partial fulfillment of the

requirements for the degree of

Doctor of Philosophy

University of Washington

2024

Reading Committee:

Charles T. Campbell, Chair

David S. Bergsman

Daniel T. Schwartz

Program Authorized to Offer Degree:

Chemical Engineering

University of Washington

Abstract

Adhesion and Adsorption Energetics of Late Transition Metal Nanoparticles on Oxide and Carbon Supports for Predicting Catalyst Behavior and Enabling Catalyst Design

Nida Janulaitis

Chair of the Supervisory Committee:

Charles T. Campbell

Heterogeneous catalysts are a critical part of many important industries and fields and are used in the production of most of today's chemicals worldwide. They also play a critical role in enabling clean technologies, reducing our reliance on fossil fuels, and environmental remediation. Most heterogeneous catalysts (including electrocatalysts) consist of metal nanoparticles on a high surface area catalytic support, which is usually an oxide or carbon-based material. This dissertation seeks to understand fundamental metal nanoparticle / catalytic support system energetics to provide information that can accelerate catalysis research and improve catalyst design.

A key descriptor for metal / support system energetics is the metal atom chemical potential versus particle size, because the chemical potential determines catalyst reactivity and stability. The chemical potential also plays a key role in governing the sintering resistance of these systems, which is crucial because sintering poses one of the greatest challenges to

preserving the activity of industrial catalysts over time. As shown here, the adhesion energy of a bulk metal / support system directly gives the chemical potential versus particle size of a system, and the adsorption energies of the metals to the support versus metal coverage also directly provide their chemical potential versus size. The best method for measuring metal adsorption and adhesion energies to well-defined solid surfaces is single-crystal adsorption calorimetry (SCAC), because it directly measures the heat of adsorption of metal atoms on an ordered support surface with known atomic structure. In this work, SCAC is used to measure the adhesion and adsorption energies of multiple systems, in a directed effort to predict the energetics of metal / support systems and provide benchmarks for improving theoretical methods.

The first system studied here is Pd / graphene / Ni(111). Although most preceding SCAC measurements were made on systems involving oxide surfaces, carbon-based supports have gained much attention and have become very important in industry as well as very promising in catalysis research for a large variety of applications. The adsorption energies and chemical potential as a function of Pd nanoparticle size are reported, and the adhesion energy of Pd / graphene / Ni(111) is found to be 3.5 J/m^2. The growth morphology of the Pd nanoparticles was investigated using He^+ low-energy ion scattering spectroscopy (LEIS). Because the adhesion energy of two other metals, Ag and Ni, had been previously measured using SCAC, this Pd data reveals a new trend correlating the adhesion energies of metals to graphene / Ni(111). A linear trend is observed between the adhesion energy of a metal to graphene / Ni(111) and the carbophilicity of the metal, which is estimated here based on DFT calculations.

The next system studied here is Cu / rutile-TiO_2(100). The Cu adsorption energies and Cu chemical potential versus Cu nanoparticle size are reported. The Cu particle size versus coverage was measured using He^+ LEIS. The growth of the particles was initially modeled using the

hemispherical cap model (HCM), and then that model was converted to the recently developed spherical cap model (SCM), which can determine the contact angle of metal nanoparticles. The contact angle of the Cu nanoparticles on rutile-TiO_2(100) is 67°. We also show that the recently-published mathematical shortcut, by which the SCM can be determined from the HCM, is accurate. The adhesion energy of Cu / rutile-TiO_2(100) is found to be 2.5 J/m^2, from the SCM. The adhesion energy is also compared to previous measurements on rutile-TiO_2(100), and the adhesion energy of metals to this surface tends to linearly correlate with the metal oxophilicity.

For oxides, linear proportionalities between the adhesion energy of the metal to a given surface and the oxophilicty of the metal have been previously observed for two surfaces: MgO(100) and CeO_2(111). In the next part of this work, we show that this proportionality between the oxophilicity of a metal and the adhesion energy of that metal to the oxide surface also holds for rutile-TiO_2(100), a third proportionality of this kind. Although these proportionalities are great for predicting the adhesion energies of late transition metals on the three surfaces mentioned, there was still lack of knowledge when it comes to predicting adhesion energies of these metals across other oxide supports. This work shows that the slope of the adhesion energy versus oxophilicity proportionality for a given oxide surface can be predicted based on its surface oxygen vacancy formation energy and/or the heat of reduction of the bulk oxide to its next lower oxidation state. The ability to predict these adhesion energy values is a valuable tool for catalyst design, since it allows predicting metal chemical potential versus particle size for different oxide supports.

Table of Contents

List of Figures viii

List of Tables xiv

Chapter 1. Introduction 1

Chapter 2. Experimental Methods 11

2.1 Metal Vapor Adsorption Calorimeter 11

2.2 Sample Preparation 13

2.3 Calorimetry Measurement 15

2.4 Growth Morphology Measurement with LEIS 17

2.5 Figures 18

Chapter 3. Size-Dependent Energy and Adhesion of Pd Nanoparticles on Graphene on Ni(111) by Pd Vapor Adsorption Calorimetry 19

3.1 Introduction 20

3.2 Experimental Methods 22

3.3 Results 24

3.3.1 Pd Sticking Probability on Graphene/Ni(111) 24

3.3.2 Pd Growth Morphology on Single-Layer Graphene on Ni(111) 25

3.3.3 Heat of Adsorption of Pd on Single-Layer Graphene on Ni(111) 31

3.3.4 Pd Chemical Potential Versus Particle Size and Adhesion Energy of Pd onto Graphene/Ni(111) 33

3.4 Discussion 36

3.4.1 Comparison of Heats of Adsorption and Adhesion Energy with DFT Results 36

3.4.2 Trend of Adhesion Energy of Metals on Single-Layer Graphene on Ni(111) 39

3.5 Conclusions 42

3.6 Figures 44

Chapter 4. Energetics of Cu Adsorption on and Adhesion to Rutile-TiO_2(100) Studied by Cu Vapor Adsorption Calorimetry 50

4.1 Introduction 51

4.2 Experimental Methods 53

4.3 Results 56

4.3.1. Cu Sticking Probability on Rutile-TiO_2(100) 56

4.3.2 Cu Growth Morphology on Rutile-TiO_2(100) 58

4.3.3 Heat of Adsorption of Cu on Rutile-TiO_2(100) 60

4.3.4 Chemical Potential and Adhesion Energy of Cu on Rutile-TiO_2(100) 63

4.4. Discussion 67

4.5 Conclusion 70

4.6 Figures 72
Chapter 5. Predicting adhesion energies of late transition metal nanoparticles to oxide support surfaces using oxide reducibility and metal oxophilicity: toward predicting catalyst performance 78
5.1 Introduction 80
5.2 Results and Discussion 83
5.3 Conclusion 91
5.5. Tables 98
Chapter 6. Continuing Small Molecule Adsorption Calorimetry: Understanding the Energetics of Solvents and Reaction Intermediates on Model Catalyst Surfaces for Applications in Catalyst Design 101
6.1 Introduction 102
6.2 Experimental Methods 103
6.3 Future Outlook 104
6.4 Figures 106
Chapter 7. Improving Our Understanding of Kinetics Using Degree of Rate Control Analyses: Relationship to Volcano Plots and Experimental Measurements 107
7.1 Degree of Rate Control Analysis of Volcano Plots for Improving Catalyst Design 108
7.1.1 Introduction 108
7.1.2 Methods 110
7.1.3 Results and Discussion 112
7.2 Studying Reaction Kinetics by Using Experimental Measurements to Determine Degrees of Rate Control 114
7.2.1 Introduction 114
7.2.2 Results and Discussion 116
7.3. Figures 120
7.4 Tables 124
Chapter 8. Conclusions and Future Outlook 127
Chapter 9. Bibliography 131

List of Figures

Figure 2.1. A photograph of the metal vapor adsorption calorimeter is shown. The main chamber is in the center box and includes calorimetry equipment as well as surface characterization and analysis instrumentation. The box on the right shows the location of the sample preparation chamber, and the sample manipulator is located to the right of that chamber (extends out-of-frame). The electron-beam chamber is labeled and indicated by the square box below the main chamber. To the left of the main chamber is the titanium sublimation pump and main chamber turbo pump. 18

Figure 3.1. (a) Integrated Pd LEIS signal (normalized to the saturated Pd signal for a thick, continuous Pd multilayer), or f, as a function of Pd coverage on graphene/Ni(111) at 100 K (blue points) and 300 K (red points). The blue solid line corresponds to the best fit of the low-coverage data at 100 K to a hemispherical cap model, whereby Pd particles grow as hemispherical caps with a constant number density, with best-fit value of 5.5×10^{16} particles/m^2. The red solid line corresponds to the best fit of the low-coverage data at 300 K to a model which assumes the particles are cylindrical disks with constant aspect ratio ($\alpha = 0.22$) and constant number density, with best-fit value of 8.5×10^{15} particles/m^2. The dotted lines are only polynomial fits as a guide to the eye. (b) Average Pd particle thickness vs Pd coverage at 100 K (blue points) and 300 K (red points) calculated from the Pd LEIS data points of panel (a). The blue and red curves correspond to the best-fit models from part (a)..... 44

Figure 3.2. Differential heat of adsorption of Pd atoms deposited on single-layer graphene on Ni(111) at 100 K (blue points) and 300 K (red points) as a function of (a) Pd coverage

and (b) the average Pd particle diameter from fit in Figure 1(c). The solid black line stands for the sublimation energy. Measurements in (a) taken till 5 ML whereas the heat of adsorption levels off before 4 ML. The inset shows the low-coverage regime (until 0.5 ML) on an expanded scale. 46

Figure 3.3. Chemical potential of Pd atoms on single-layer graphene on Ni(111) as a function of the average Pd particle diameter during deposition at 100 K (blue points) and 300 K (red points). The blue solid line shows the hemispherical cap approximation applied to the 100 K data with E_{adh} = 3.5 J/m^2. The red solid line shows the best fits of 300 K data to the constant aspect ratio model with also E_{adh} = 3.5 J/m^2..... 47

Figure 3.4. (a) Measured integral heats of adsorption of Pd on graphene/Ni(111) (red filled circles) and reported values for Ni on graphene/Ni(111) from ref.[36] as a function of deposited metal coverage. (b) The same heats plotted versus the average number of metal atoms per particle, with comparisons to the DFT calculated energies for metal clusters on free-standing graphene, from the literature: For Pd (in red), squares,[104] stars[106] and triangles;[101] for Ni (in black), squares,[108] stars[106] and triangles.[109]..... 48

Figure 3.5. Calorimetric E_{adh} values for Ni, Pd and Ag on single-layer graphene on Ni(111) versus carbophilicity per unit area for each metal (M), estimated from $\Delta U_{ad,\,C}$, the DFT-calculated energy for C(g) adsorption on the four-fold step-edge site of the M(211) surface. The best linear fit of the three points of Ni, Pd and Ag gives E_{adh} = 0.130 × carbophilicity/area + 0.69 J/m^2. The values of E_{adh} predicted for other metals from this linear relation are shown as red points..... 49

Figure 4.1. Sticking probability of Cu on rutile-TiO_2(100) at 300 K (red) and 100 K (blue). The data for each temperature includes multiple experimental runs. The lines are the best fits

for each temperature to the simple function $S = 1 - C\ exp\ (-X/X0)$, (300 K: C = 0.0042, X_0 = 4.8; 100 K: C = 0.019, X_0 = 1.6) 72

Figure 4.2. Integrated Cu LEIS signals as a function of Cu coverage at 300 K (red) and 100 K (blue). Signals are normalized to the integrated signal of a thick, continuous Cu multilayer. The lines show the best fit of the data to the HCM, with best-fit values of 1.5 × 10^{17} and 2.4 × 10^{17} particles/m^2 at 300 K and 100 K, respectively. The transitions to the dashed lines indicate the Cu coverages where the data were no longer used in calculating the best fits, due to possible overlapping-shadow effects. These fit lines are identical to the fit lines to a spherical cap model (SCM) described in the text with a contact angle of 67° and particle densities of 7.4 × 10^{16} and 1.2 × 10^{17} particles/m^2 at 300 K and 100 K, respectively. This SCM model is preferred because it fits better to the measured heat data (see below). 73

Figure 4.3. Differential heat of Cu adsorption on rutile-TiO_2(100) at 300 K for surfaces that are low in defect density (red) and high in defect density (black)..... 74

Figure 4.4. Differential heat of Cu adsorption on rutile-TiO_2(100) with low defect density at 300 K (red) and 100 K (blue) as a function of Cu coverage..... 75

Figure 4.5. Chemical potential of Cu atoms in Cu nanoparticles on rutile-TiO_2(100) (low defect density) at 300 K (red) and 100 K (blue) as a function of effective nanoparticle diameter, assuming the HCM. The black curve shows the best fit to the E_{adh} equation (E_{adh} = 3.57 J/m^2) with D_0 = 1.5 nm. 76

Figure 4.6. Chemical potential of Cu atoms in nanoparticles on rutile-TiO_2(100) (low defect density) at 300 K (red) and 100 K (blue) as a function of nanoparticle footprint diameter,

using the SCM. The black curve shows the SCM, Eq. 3, with $E_{adh,SCM}$ = 2.50 J/m^2, θc = 67°, and D_0 = 1.5 nm..... 77

Figure 5.1. The adhesion energy of metals on CeO_2(111), rutile-TiO_2(100), and MgO(100) as a function of metal oxophilicity per unit area (Oxo). Solid lines are the best linear fits passing through (0, 0) for each oxide. Slope values are 0.188 for CeO_2(111), 0.169 for TiO_2(100), and 0.102 for MgO(100). Circular points are SCAC measurements (using the SCM or flat-disk model), and square points are particle shape measurements. For additional details on the CeO_2(111) and MgO(100) data, see ref.[38] 93

Figure 5.2. The slope for correlating adhesion energy of metals on oxides with metal oxophilicity for each of the oxides is plotted as a function of (a) the negative standard enthalpy of reduction of each oxide to its next lower oxidation state plus ½ O_2(gas), $\Delta H_{red,ox}$, and (b) DFT-calculated negative oxygen vacancy formation energies for the oxide surfaces. The larger circles are the ΔE_{Ov} values reported for CeO_2(111),[164,165] rutile-TiO_2(100),[166] and MgO(100)[165,167] which are used to calculate the line of best fit. Some DFT values (smaller circles) were excluded in this fit because they were calculated using larger or unstated vacancy concentrations or a lower level of theory. For comparison, other reported DFT values are shown as smaller circles. The data in this plot and corresponding citations are listed in Table 5.1. 94

Figure 5.3. The oxygen vacancy formation energies, ΔE_{Ov}, for CeO_2, TiO_2, MgO, and Fe_2O_3 surfaces are shown as a function of the standard enthalpy of reduction of the bulk oxide to its next lower oxidation state plus ½ O_2 gas, $\Delta H_{red,ox}$. The line of best fit through the points is shown in black, with the equation of the line, showing that it is a near 1:1 proportionality. The data shown here are listed in Table 5.1..... 95

Figure 5.4. The measured adhesion energies of metals on CeO_2(111), rutile-TiO_2(100), MgO(100), rutile-TiO_2(110), Fe_3O_4(111), α-Al_2O_3(0001), and rutile-TiO_2(110) as a function of metal oxophilicity per unit area, scaled by f(oxide)/ f(MgO(100)), as in Equation 5.6. Each f(oxide) is calculated from the fit in Figure 5.2(b) (Equation 5.5), whereby f(MgO(100) = 0.106. The solid line here is the proportional line of best fit, with a slope of 0.097. The standard deviation of the measured E_{adh} values from this best fit line is 0.52 J/m^2, and its r2 score is 0.75. 96

Figure 5.5. The adhesion energies for late transition metals measured on clean, well-defined oxide surfaces, normalized by twice the surface energy of the metal, plotted as a function of the DFT-calculated single metal atom binding energy to the surface, normalized by the sublimation energy of the metal. The dashed parity line (where these values would equal each other) is the correlation suggested by Hu and Li in ref.[151]. The standard deviation from and r^2 value for the parity line are 2.2 J/m^2 and 0.090, respectively. The standard deviation from and r^2 value for the line of best fit to these data (not shown) are 0.47 and 1.9 J/m^2, respectively. For plot data, see Table 5.3. 97

Figure 6.1. A photograph of the small molecule single-crystal adsorption calorimeter is shown. There is a single main chamber, with the sample manipulator located on top. The molecular beam is located to the right of the chamber. Instrumentation for sample preparation and characterization is located around the top region of the chamber, and the calorimetry equipment is in the lower region of the chamber. The titanium sublimation pump can be seen below the main chamber at table level. The main turbo pump is located under the titanium sublimation pump, under the table (not visible). 106

Figure 7.1. (a) A 2-descriptor volcano plot of the methane steam reforming reaction rate per surface site (TOF in s^{-1}),[210] with the specific locations of transition metal catalysts within this "materials space" marked. The dotted line indicates the location of the plot shown in Figure 7.2. (b) DRC map for high-coverage intermediates in methane steam reforming,[210] plotted in the same descriptor space as the volcano plot in part (a). The color at each point is weighted by degrees of rate control for intermediates C^*, CO^*, and O*..... 120

Figure 7.2. A 2D representation of the volcano plot for E_{c*} = 3.5 eV. Points A and B are marked for demonstrative purposes that are described in the text. See Figure 7.1 to see the location of this line on the volcano plot..... 121

Figure 7.3. Coverage of intermediates versus one single descriptor. Plot (a) shows where E_{O*} = 2.0 eV in Figure 7.1b and plot (b) shows where E_{C*} = 1.0 eV in Figure 7.1b. Note that C* occupies different sites that CO* and O*, so that the sum of CO* and O* coverages may be as large as 1 no matter how high is the C* coverage. 122

Figure 7.4. (a) Arrhenius plot for CO_2 hydrogenation on Cu(211) at 30 bar from 400 to 700 K. The apparent activation energy at 450K is shown as well as the line of best fit that was used to solve for the slope and apparent activation energy. (b) Plot of the activation energy versus 1/T for the same temperature range as shown in (a)..... 123

List of Tables

Table 5.1. The best-fit proportional slopes of the adhesion energy of metals on oxides versus the metal oxophilicity (per area) for each of the oxide surfaces (from Figure 5.1), the standard enthalpies of reduction of the bulk oxides to their next lower oxidation state plus ½ O_2(gas) ($\Delta H_{red,ox}$), and DFT-calculated oxygen vacancy formation energies for these oxide surfaces (ΔE_{Ov}). The bold values are those used to calculate the line of best fit (f) shown in Figure 5.2b..... 98

Table 5.2. Adhesion energies for late transition metals on oxide surfaces, as well as the method by which they were obtained, and the scaled Oxo values via Equation 5.6, using the f($E_{Ov,ox}$) (=f(ox)) values from Equation 5.5, which gives f(MgO(100)) = 0.106. These two values are plotted against each other in Figure 5.4..... 99

Table 5.3. Values used to make Figure 5.5. For each metal / surface combination, the metal surface energy (from [38]), bulk metal sublimation energy (ΔH_{sub}, equal to its cohesive energy, E_c), and the single metal adatom binding energy on the surface (E_{bs}, from ref.[158]) is listed. The normalized binding energy, E_{bs}/E_c, and normalized adhesion energy, $E_{adh}/(2\gamma m)$, as plotted in Figure 5.5, are also listed, using E_{adh} values for clean oxide surfaces from Table 5.2..... 100

Table 7. 1. Case 1: One high-coverage intermediate and one transition state with high DRC.. 124

Table 7.2. Case 2: One high-coverage intermediate and two transition states with high DRC. 125

Table 7.3. Case 3: Two high coverage intermediates and two transition states with high DRC. 126

Acknowledgments

This work was funded by the Department of Energy, Office of Basic Energy Services, under Grant Number DEFG0296ER14630. This work was also supported by the B. Seymour Rabinovitch Chair Endowment.

First and foremost, I would like to express my deepest gratitude to my advisor Dr. Charlie Campbell for providing me with the opportunity to continue my academic career under his mentorship. His hard work, depth of knowledge, and scientific impact are a constant source of inspiration. I am honored to have had the opportunity to learn from him. His thoughtful advising provided me with the guidance necessary to move forward, while also challenging me to gain confidence as a scientist and take ownership of my work. Encountering and overcoming challenges is a large part of any graduate career, and Charlie's expert advice, patience, and encouragement taught me how to approach and overcome obstacles in a methodical and optimistic way, and even to embrace them for the valuable experience they provided me. I am so thankful for his expert advice and support, especially during the most difficult challenges; it made my experience as a graduate student truly enjoyable and allowed me to focus on learning to be a better scientist. His passion for good science is contagious and fueled my own excitement and enthusiasm for science and engineering. I could write pages thanking him for everything he has done for me and my education, but, due to a lack of space to do that here, I will just say that I feel incredibly lucky to have had Charlie as my advisor and I will always consider him a great friend and role model.

Next, I would like to extend a heartfelt thank you to the students who came before me in the Campbell Group for their hard work and dedication – they built the foundation on which the work presented here is built. I would especially like to thank the students who I had the

opportunity to work with and learn from, they were always so kind and knowledgeable and it was an absolute pleasure working with them. Thank you to Dr. Jack Rumptz and Dr. Kun Zhao for training me on the calorimeter and for their patience in doing so. They often prioritized my learning, even when it cost them time on ongoing experiments and projects. This generosity was deeply appreciated. I would also like to thank Dr. S. Elizabeth Harman and Dr. Griffin Ruehl for teaching me about their calorimeter and for always having excellent advice, or at least commiseration, when we ran into challenges on our instrument. It was always a fun experience working alongside them in lab and their willingness to teach me about their instrument gave me the opportunity to be a small part of continuing its good work at Pacific Northwest National Laboratory.

I must thank the members of the UW Chemistry department for all the work they did to support my projects and graduate career. They were also great friends to me and kept me from feeling isolated even as a solo lab member. In the machine shop, thank you to Kevin Soderlund and Brian Wadey for being there for helping me build and fix things, providing a helping hand, and giving me tools and materials I needed for my projects. In the electronics shop, thank you to Kit Sczudlo, Rachael Huffman, and Bill Beaty for their help, advice, and willingness to patiently teach me about electronics despite my lack of knowledge in that area when I first began. In the UW Chemical Shop, I want to give a heartfelt thank you to Loch Hickock for his help with anything and everything; no matter what challenges or doubts I encountered, he never failed to give great advice and help and to provide a friendly ear when I most needed it.

I would also like to thank the members of my committee for their time and support. The impression Dr. Daniel Schwartz left on my undergraduate research advisor at UGA was a big reason why I ended up at UW at all. It was an honor to interact with Dr. Oscar Vilches in group

meetings because of the great scientific impact he has had in his career, and I appreciated and learned a lot from his insights and perspectives. I also had the privilege of working closely with Dr. David Bergsman while serving as a teaching assistant for two of his courses, and it was an absolute pleasure working with and learning from him.

Finally, I would like to express my sincere gratitude to my family and friends—of course this work would not have been possible without their support and encouragement.

There are many individuals who have been important to my graduate experience, and I am deeply grateful to them all. While I may not have the space to thank everyone individually here, I want to extend my heartfelt appreciation to everyone who supported me in my effort to complete the work shown below.

Chapter 1. Introduction

Heterogeneous catalysts are a crucial component of our society, enabling the production of over 80% of chemical products worldwide. With a catalyst market size of nearly 34 billion USD in 2019, their economic impact is profound, and reflective of the critical role they play in facilitating essential reactions and reducing energy requirements for production processes.[1–5] Heterogeneous catalysts allow us to perform essential chemical reactions to synthesize materials essential for our food, energy, pharmaceutical, and other chemical production industries. Without catalysts, most industrial reactions that are widely used today would be too slow or energy-intensive to be feasible, especially in the amounts required today by the world's growing population.

As our population grows, the production of energy has become a critical issue for our society. Our reliance on fossil fuels is dangerous for our planet and for us, and developing clean energy alternatives, as well as lowering energy requirements for large-scale production processes and reducing environmentally dangerous waste, is vital for the future of our society. Catalysts play a significant role in mitigating the effects of climate change, for example by reducing air pollution due to exhaust from diesel engines.[6] Many green technologies such as clean fuel production, waste reduction and conversion, and greenhouse gas reduction depend on the advancement of innovative and efficient catalysts.[7–9] Heterogeneous catalysts also avoid many of the pitfalls of homogeneous catalysts, which are often hazardous to the environment,[10,11] or too costly to separate from products. Huge research efforts are dedicated to understanding, developing, and optimizing heterogeneous catalysts because of their power to enable clean technologies and mitigate and reduce the dangerous effects of unsustainable processes.

Synthesizing and testing different catalysts at reaction conditions is one way to search for good catalysts, but it is time-consuming and can lack important insight into how the catalysts work and how exactly the reaction occurs, information that is essential for optimizing catalysts and minimizing the number of experiments required to find the most efficient catalyst.[3] Theoretical methods, such as density functional theory (DFT) and molecular simulations, can be used to calculate atomic-level behavior of catalysts and the reactions that occur on them, but they still often lack accuracy, especially for heterogenous catalytic systems, which are exceptionally complicated to capture even with advanced theoretical models.[12] Computational research into catalysts is exciting because it promises much faster and more detailed insight, and recent advancements in computational power have enabled exciting advancements, but the development of these techniques depends on reliable experimental benchmarks. Without surface science experiments detailing fundamental energetics of catalysts, theoretical models could not be developed or relied upon to capture catalyst behavior because they would not have a reference to gauge the accuracy of these techniques in estimating essential energy values. Furthermore, understanding the fundamental energetics of catalysts is critical for understanding how catalyst structure affects catalyst properties and for informing catalyst research. The work presented here uses a surface science approach to catalyst research and seeks to understand fundamental energetics of catalysts to enable better and quicker catalyst design.

Most heterogeneous catalysts (except those based on zeolites) consist of metal nanoparticles, specifically late transition metals, on high surface area catalyst supports. Most catalyst supports are oxides or carbon-based materials, such as graphite or graphene. These types of systems are also important because they are used in a variety of industries, including semiconductors and sensors. Model catalysts involve well-ordered clean single-crystal surfaces

and are usually studied in UHV to reduce complexity and allow for analytic techniques that give atomic- and molecular-level understanding of the system, and are more easily modelled with computational catalysis methods like DFT. They can give fundamental insight into the energetics of heterogeneous catalysts and experimental information about systems that can then be used to benchmark theoretical techniques, which are mostly focused on capturing the energetics of clean and well-defined surfaces before introducing complexities associated with macroscopic catalytic structure and real reaction conditions.[13–15] Even for model catalysts, defects and impurities still exist and affect the system, but because the number of variables is reduced to a minimum, the energetics between the metal and the surface can still be measured and deconvoluted from other energetic influences. All the experiments in this work are performed on model catalyst surfaces so that fundamental energetics can be determined and more easily connected to details of the surface structure and composition.

One of the most important properties of metal / support catalysts is the bonding strength between the metal nanoparticles and the catalyst support surface because it directly mediates the properties and behavior of the nanoparticles. The adhesion energy between the metal and the surface is an important property because it directly gives the chemical potential of the metal atoms versus particle size for a given metal / support system,[16–18] as discussed in detail below. The chemical potential is a convenient and widely used descriptor for these systems because it includes the effect of the nanoparticle size as well as the binding energy to the support. Metal chemical potential is a particularly important thermodynamic property because it determines the reactivity of the nanoparticles and their sintering resistance. Sintering is the process by which smaller metal nanoparticles form larger clusters under reaction conditions. Sintering kinetic equations directly use the chemical potential when calculating the rate and activation energy for

the process.[17,19,20] Sintering is one of the most difficult challenges of industrial catalysts, because when catalysts sinter, catalysts are deactivated because both the surface area and the reactivity of the metal nanoparticles decreases.[21] Understanding and predicting the sintering resistance of metal nanoparticle / support systems is therefore critical for designing efficient and reliable catalysts.

Adhesion energy describes the interfacial energy between the bulk metal and bulk support surface, but on a nanoparticle level, the bonding energy between the metal nanoparticles and support are usually measured in the form of adsorption energies. Historically, temperature programmed desorption (TPD) measurements were used to measure adsorption energy,[22] but this technique mostly fails for late transition metal / support systems because as the temperature increases the metal atoms become more mobile and the nanoparticles restructure before desorbing, which is an irreversible process. David King's group addressed the challenge of directly measuring adsorption energies when they developed Single Crystal Adsorption Calorimetry (SCAC), a technique that directly enables precise measurement of adsorption energies.[23–26] Their technique used an infrared detector to directly measure heat changes on the surface of the sample upon small molecule adsorption. The Campbell group used some of the principles of King's technique to build a new calorimeter that is specifically capable of measuring metal adsorption and adhesion to surfaces.[27] The instrument uses a much more sensitive heat detector based upon a pyroelectric polyvinylidene fluoride (PVDF) ribbon that rests against the back of a thin sample to measure heat changes on the surface of the sample. An electron-beam evaporator is used to generate a flux of metal vapor, which is deposited on the sample in pulses during a calorimetry measurement. The sample is a well-defined single crystal surface, and the experiment is performed in ultrahigh vacuum (UHV) conditions to ensure a

clean surface. The sample is often a model oxide or carbon-based support material surface, such as $CeO_2(111)$[28] or graphene,[29] and are chosen based on whether they would be a good benchmark for theory and/or their relevance as real support materials in industrial catalysts. The SCAC apparatus developed by the Campbell group directly measures the adsorption and adhesion energies of metal nanoparticles on solid support surfaces, which is critical for gaining a fundamental understanding of metal / support systems and facilitate their design. The metal vapor adsorption calorimetry instrument is used for the experiments presented in this work. The details of the calorimeter design, as well as the processes by which data are obtained and analyzed, are given in Chapter 2.

The metal vapor adsorption calorimeter has been successfully used by the Campbell group to measure adsorption and adhesion energies for a variety of late transition metal / support combinations.[28–33] Most of the measurements have been performed on oxide surfaces,[28,31–35] because of the importance of oxides in industrial catalysis, but, more recently, measurements have been made for carbon-based surfaces in the form of graphene supported by Ni(111).[29,36] Measuring the adhesion energies of various metals on the same surface is essential, as it enables correlations between adhesion strengths and specific metal properties. Correlations developed in this way showed that the adhesion energy of metals to a given oxide surface correlates linearly with the oxophilicity per unit area of the metal.[18,37] The oxophilicity is a measure of how strongly the metal binds oxygen atoms, defined here as is the reaction enthalpy to go from a metal gas atoms plus O_2(gas) to the most stable oxide of that metal, is calculated by taking he difference between the metal's bulk heat of sublimation and the heat of formation of the most stable oxide of the metal (per mole metal). To get oxophilicity per unit area, the oxophilicity is normalized using an estimate of the surface area per metal atom, which is calculated by dividing

the molar volume of the bulk metal by Avogadro's number and taking the 2/3 power of that. The oxophilicity per unit area for most late transition metals have been reported;[38] therefore, if the linear relationship between adhesion energy and oxophilicity per unit area is determined for a given surface, it is easy to predict the adhesion energies of other metals on that surface.

Although correlations between adhesion energy and oxophilicity have been published for MgO(100) and CeO_2(111),[18,37] no such correlation has been developed for any carbon-based support surface. Carbon-based catalyst supports are popular because of their tunable structure, high surface area, low cost, and minimal environmental impact.[39–42] Carbon supports also have tunable electrochemical properties, which makes them particularly promising for electrocatalytic applications, such as those related to clean energy production.[43–47] Graphene, a 2-dimensional, atom-thick allotrope of carbon is an especially exciting catalytic, and electrocatalytic, material due to its high conductivity, high surface area, and compatibility with functional groups.[48–52] These unique properties make graphene an interesting substrate for investigating metal interaction and adhesion. The adhesion energies of Ni[36] and Ag[29] on graphene / Ni(111) have been previously measured using SCAC. In Chapter 3, the adhesion energy of Pd on graphene / Ni(111) is measured and reported. Because Pd is the third metal to be measured on the graphene / Ni(111) surface, a correlation is also developed for the adhesion energies on the graphene / Ni(111) surface. In the case of carbon supports, the oxophilicity can no longer be used as a descriptor for the metal when correlating its adhesion energy to the surface, because there is no oxygen on the surface to which metal atoms would bind. Instead, a new descriptor, carbophilicity, is developed and presented, assuming that the dominant bonding across the metal / graphene interface is due to metal – carbon bonds. The details of calculating the carbophilicity are described in Chapter 3, and the value is also normalized so that it is per unit area in the same

way that the oxophilicity was normalized per unit area, as described above. The trend presented in Chapter 3, showing a linear increase in adhesion energy with metal carbophilicity per area, is an exciting start to understanding and predicting the energetics of metal nanoparticles on carbon support materials.

Besides carbon supports, oxide supports are another major category of support, which are widely used in industry for their catalytic performance, durability, and long history of being reliable catalyst supports.[11,53] One widely used and studied oxide is TiO_2, which is used as a catalytic support for important processes such as the reverse water-gas shift reaction,[54] biomass upgrading,[55] and photocatalytic hydrogen production.[56] TiO_2 is a promising support for renewable energy applications,[57] and understanding the activity of different types of catalytic metal nanoparticles on this support would assist in designing optimal versions of TiO_2 catalysts. Cu supported on TiO_2 is an interesting photocatalyst,[58,59] and a Cu / TiO_2 system has not yet been studied via SCAC. The adhesion and adsorption energies of Ag / rutile-TiO_2(100) has been previously measured using SCAC.[35] In Chapter 4, the energetics of Cu / rutile-TiO_2(100) are reported, and the adhesion energy is determined using SCAC. This new measurement offers an important comparison for the previous measurement of Ag / rutile-TiO_2(100), as well as previous metal / oxide measurements. The growth morphology of Cu nanoparticles on the rutile-TiO_2(100) is also investigated (as described in Chapters 2 and 4) and a recently developed particle growth model, the spherical cap model (SCM),[60] is implemented. We first model the growth data using the hemispherical cap model (HCM),[61] which is a model that has historically been effective for modeling nanoparticle growth data for some systems, but it constrains the contact angle of nanoparticles to 90°, so adhesion energies are not always consistent with the Young-Dupre equation.[62] The new SCM can be used also to calculate the contact angle of the

particles so that it is consistent with the Young-Dupre equation. In Chapter 4, we use the equations developed by Zhao et al.[38,60,63] to convert the HCM results to SCM results and determine the contact angle of the Cu nanoparticles on rutile-TiO_2(100).

SCAC adhesion energy results that had previously been modeled using the HCM were remodeled using the new SCM by Zhao et al. and the trends for adhesion energy as a function of oxophilicity per unit area for MgO(100) and CeO_2(111) were updated based on the results.[38] Although the published proportionalities for adhesion energies on MgO(100) and CeO_2(111)[18,37,38] have made it simple to predict adhesion energies of other metals on these two surfaces, there is still a lack of understanding of how the oxide surface correlates with adhesion energy on other surfaces and what descriptors may be used to predict adhesion energies not just for a given oxide, but also across different oxide support surfaces. Performing SCAC experiments and determining adhesion energy experimentally is time-consuming and expensive, so being able to predict these values would be very valuable. In Chapter 5, a new proportionality is shown relating adhesion energy of metals on rutile-TiO_2(100) to the oxophilicity per unit area of metals. The proportionality predicts the adhesion energies of metals to this important surface, based only on the oxophilicity per unit area of the metals, which have been calculated and reported for many important late transition metals.[38] With the addition of this new proportionality, the adhesion energy trend is known for three surfaces, which means that we can begin to predict how properties of the oxide surface affect adhesion energies and what descriptors may be important for predicting them on other oxide surfaces. In Chapter 5, we show that the oxygen vacancy formation energy of the oxide is an important descriptor that can be used to predict the slope of the adhesion energy versus oxophilicity proportionality for oxides. This relation allows all measured adhesion energies of late transition metals on oxides to be

scaled to a single trendline, as shown in Chapter 5. This finally gives us the ability to predict adhesion energies for all oxide surfaces and any late transition metal without expending the many resources that are required to determine a proportionality for a given surface. This powerful and very general ability to predict adhesion energy, and therefore chemical potential versus particle size, for late transition metal / oxide systems is an exciting new contribution that will aid in catalyst research, screening and design.

With numerous combinations of metals and catalyst supports, isolating the most promising catalysts is crucial for advancing catalyst research to its full potential and addressing today's pressing challenges. The correlations and trends presented in Chapters 3 and 5 contribute to this goal by providing predictions about catalyst behavior based on the properties of their constituent materials, for both carbon and oxide support. Furthermore, the specific metal / support combinations examined in Chapters 3 and 4 serve as valuable DFT benchmarks, aiding theoretical methods in improving their accuracy for calculating energetics of complex heterogeneous catalysts. This improved reliability will help streamline catalyst research and design and enable the field to keep pace with today's growing and evolving challenges that demand catalytic solutions.

In Chapter 2, the experimental methods used in this work are described in detail, including a description of the calorimeter, how to perform metal vapor adsorption calorimetry, how the sample is prepared, and how to perform growth morphology experiments. Chapter 3 presents the results of the experiments described in Chapter 2 for the Pd / graphene / Ni(111) system and shows the linear relationship between the adhesion energy of metals on graphene / Ni(111) and the carbophilicity of the metals. Chapter 4 studies the adsorption and adhesion energetics of the Cu / rutile-TiO_2(100) system. Chapter 5 presents the adhesion energy

proportionality as a function of oxophilicity for the rutile-TiO_2(100) surface and combines it with previously published trends to give correlations that can be used to predict the adhesion energy of late transition metals across oxide surfaces based on metal oxophilicity and oxide reducibility. Chapter 6 discusses the work done to continue the operation and research of a unique small-molecule single-crystal adsorption calorimeter, which I helped move from Campbell's lab at the University of Washington to Dr. Zdenek Dohnalek's lab at Pacific Northwest National Labs in Richland, WA. Chapter 7 presents in-progress work regarding Degree of Rate Control (DRC) analyses and shows its connection to volcano plots and experimental measurements, so that DRC analysis can be employed to fuller extent as a powerful tool in catalysis research.

Several of these chapters have been published or submitted for publication in peer-reviewed journals, as summarized below.

Chapter	**Citation**
Chapter 3	K. Zhao, N. Janulaitis, J.R. Rumptz, & C.T. Campbell (2023). Size-Dependent Energy and Adhesion of Pd Nanoparticles on Graphene on Ni(111) by Pd Vapor Adsorption Calorimetry. *ACS Catalysis*, *13*(4), 2670–2680.
Chapter 4	N. Janulaitis, K. Zhao, C.T. & Campbell (2024). Energetics of Cu Adsorption on and Adhesion to Rutile-TiO2(100) Studied by Cu Vapor Adsorption Calorimetry. *The Journal of Physical Chemistry C*, *128*(39), 16481–16490.
Chapter 5	N. Janulaitis & C.T. Campbell (2024). Predicting adhesion energies of late transition metal nanoparticles to oxide support surfaces using oxide reducibility and metal oxophilicity: toward predicting catalyst performance. *ACS Catalysis*. Under Review.

Chapter 2. Experimental Methods

Single-crystal adsorption calorimetry (SCAC) experimental design principles and techniques have been extensively documented.[22,27,64] Experimental data in this work are obtained using a unique single crystal adsorption calorimeter, which has been previously described in detail.[27] In this chapter, the calorimeter design is described briefly (2.1) as well as the procedures required for preparing samples (2.2) for the systems examined in Chapters 3 and 4. The procedures for performing calorimetry experiments (2.3) and growth morphology experiments (2.4) using the apparatus are also described briefly.

2.1 Metal Vapor Adsorption Calorimeter

The instrument consists of three ultra-high vacuum (UHV) chambers: a preparation chamber, where the sample is prepared and cleaned, a main chamber, for calorimetry and growth mode experiments and sample characterization, and a beam chamber, where the deposition metal is evaporated and partially collimated into a beam, and where the off-axis beam flux is measured. For a fundamental understanding of model catalyst energetics, it is essential that the support surfaces to be studied are clean and structurally well-defined. Each chamber may be isolated from the others via gate valves. Experiments are run at base pressures $< 2 \times 10^{-10}$ torr in the main chamber, to minimize the impact of impurities on measurements and characterizations.

The preparation chamber contains a sample heater, pyrometer, metal doser, directed gas doser, and ion gun. A quadrupole mass spectrometer (QMS) allows for monitoring the composition of gases present in the preparation chamber. Leak valves on the preparation chamber are used to leak in gases to specific pressures for processes such as sputtering and chemical vapor deposition.

A manipulator is attached at the preparation chamber and can translate the sample horizontally into the main chamber.

The main chamber has a region for surface characterization, where low-energy electron diffraction (LEED), low-energy ion scattering (LEIS), Auger electron spectroscopy (AES), and x-ray photoelectron spectroscopy (XPS), and energy analyzer instrumentation is located. Calorimetry is performed in a separate region of the main chamber, neighboring the characterization region. Although most of the calorimetry setup is located within the chamber, there a few external components. These external components are the HeNe laser, which is shone in through a window, a power meter for measuring laser power, which is positioned outside a window. A series of mobile mirrors within the chamber exist to direct the laser toward the sample (along the same path as the atomic beam and collimated with the same beam-defining apertures to the same beam diameter), or the laser power meter with use of a mirror placed in the usual sample position. The remaining elements required for metal vapor adsorption calorimetry are located within the chamber, but many may be translated by external operators for performing experiments. One of the most important components of the calorimeter is the heat detection element, which consists of a pyroelectric β-polyvinylidene fluoride (PVDF) ribbon for direct measurement of heat changes on the sample. A stationary copper holder keeps the sample in place for deposition but leaves the bottom of the sample exposed so that deposition can occur. The holder keeps the sample located directly below the heat detection element on which the PVDF ribbon is mounted, so that the ribbon may be moved into contact with the back of the sample. A second QMS located near the sample is available to monitor the fraction of metal atoms that do not stick to the surface of the sample and the composition of gases in the main chamber. An on-axis quartz crystal microbalance (QCM) can be moved in in front of the sample to periodically monitor the metal flux near the

sample, but it must be moved out of line during deposition. To calibrate for thermal radiation from the metal pulses, a transparent barium fluoride (BaF_2) window can be translated in front of the sample, allowing radiation to pass through but not allowing metal atoms to reach the sample.

The beam chamber is located directly below the calorimetry components located in the main chamber. A series of apertures located between the beam chamber and the main chamber collimate the flux of metal atoms and set the final beam diameter to 4.26 mm. A chopper in the main chamber, between the beam chamber and the sample, allows the laser beam or beam of metal atoms to be split into pulses. Pulses for the experiments in this work are 100 ms with a period of 2 s. The beam chamber, which is connected only to the main chamber, contains an electron-beam (e-beam) evaporator, where the deposition metal is loaded into a crucible and heated via electrons emitted from a filament. Because the QCM in the main chamber cannot monitor flux while depositing on the sample, an off-axis QCM in the beam chamber continuously measures the flux near the e-beam evaporator.

2.2 Sample Preparation

The sample is a thin (1-2 μm) single crystal with a well-defined and known surface structure, e.g., Ni(111) or Mo(110), upon which films of graphene of a single-crystal oxide can be grown for adsorption calorimetry studies. The sample must be thin so that the heats of adsorption on the surface of the sample can be detected by the PVDF ribbon when it is rolled into contact on the opposite (back) side of the sample. The thin single crystal is spot welded between two thin, flat tantalum rings that keep the sample flat and stable. Once the sample is spot-welded between the rings, the piece is mounted on a copper platen that is held by the manipulator arm except during deposition for calorimetry measurements, when it is held by the Cu sample holder in the

calorimetry setup. The choice of sample depends upon the surface of interest. In most cases, the surface of interest must be grown on top of the original single crystal sample. All thin films grown on the sample are synthesized in the preparation chamber, which has the capabilities described above. Prior to growth, the sample is thoroughly cleaned using Ar^+ ion sputtering, with the duration adjusted based on the sample's condition and cleanliness.

A Ni(111) single crystal is used as the substrate for graphene growth because graphene and Ni(111) have an excellent lattice match.[65] The principles and methods of graphene growth on Ni(111) have been published in detail and the method used here was previously described in detail by Mao et al.[35] The clean sample is annealed using a heater in vacuum at ~600-650ºC for 5 min. The temperature of the sample is reported by an optical pyrometer aimed at the sample surface. While keeping the temperature constant at ~600-650ºC, the sample is exposed to 10^{-6} torr of ethylene for 30 min. The quality of the graphene is analyzed using He^+ LEIS by ensuring that no Ni is exposed on the surface.

For rutile-TiO_2(100) growth, a Mo(110) single crystal is used as a substrate. Growth of this oxide face on the Mo(110) substrate has been previously described in literature[66] and has also been previously successfully implemented by the Campbell group.[35] The clean Mo(110) surface is heated to ~350ºC and simultaneously exposed to 2×10^{-7} torr of O_2 and a flux of titanium atoms. The titanium vapor is generated via a titanium wire-wrapped filament that is resistively heated. The length of growth is adjusted depending on how much the filament has been used, because as the filament is used, it generates a lower flux of Ti, requiring longer growth times. The film is grown until the thickness of the TiO_2 is at least > 2 nm. After growth, the film is annealed by stopping the Ti flux and heating the sample to about 800 K for 10 minutes in the oxygen. The thickness of the film is estimated using the attenuation of the Mo $3d_{5/2}$ peak of the XPS spectrum,

compared to the peak on a clean Mo(110) surface. The surface structure of the film is verified using LEED. The shift and shape of the Ti $2p_{3/2}$ peak was also measured to confirm that the film was oxidized with minimal oxygen vacancies.

2.3 Calorimetry Measurement

The clean, prepared sample is held in place by a copper block, which also serves as a thermal reservoir. For 100 K experiments, the copper block and heat detection element with the PVDF ribbon (calhead) are cooled to 100 K by flowing nitrogen gas into piping near the area through coils placed in a dewar of liquid N_2. The previous cooling system used a funnel to flow liquid N_2 into the calhead / copper reservoir area, but the liquid N_2 caused a high level of noise and temperature increased by up to 20 K over the course of the heat measurement; therefore, a new system using cooled N_2 gas was built and used for the 100 K experiments reported here. The sample is also cooled separately before the experiment by flowing liquid nitrogen through tubing in the manipulator.

Before calorimetry can be performed, the sample is moved into the copper holder in the deposition area of the main chamber, and the heat detection element is translated so that the PVDF ribbon is in gentle contact with the back of the sample. The metal flux is prepared in the beam chamber by increasing current to the e-beam evaporator and monitoring the flux at the source (off-axis) QCM. Before and after the calorimetry measurement, heat response calibration is performed by measuring the power of the HeNe laser and the ribbon response to the laser pulsed onto the sample. The contact value (V/J) is calculated using the known laser power and corresponding ribbon response. The radiation is also measured before and after the calorimetric measurement to correct for its contribution to the heat signal. To measure radiation, the laser is pulsed onto the sample through the BaF_2 window, allowing the window's transmission to be calculated by

comparing the ribbon's voltage response when the laser strikes the sample directly versus when it passes through the window first. The metal is then deposited onto the window to determine the radiation emitted from generating the flux of gaseous metal atoms. The flux is measured at the sample QCM for two minutes before deposition. The off-axis QCM continuously measures and records the flux in the beam chamber. Calorimetry is performed by depositing the metal onto the sample in a series of pulses, while the heat response of the ribbon is recorded. The amount of metal deposited on the sample is measured in monolayers (ML), which are defined by the substrate surface density. For experiments on graphene, one ML is defined by the Ni(111) surface density ($1.87*10^{19}$ atoms/m^2), which is equal to ½ the surface carbon atom density of graphene. For experiments on rutile-TiO_2(100), one ML is defined as 7.36×10^{18} atoms/m^2, which is the surface density of coordinatively unsaturated O atoms on ideal bulk-terminated rutile-TiO_2(100). After calorimetry, the flux near the sample is recorded for an additional two minutes and the second round of heat and radiation calibration measurements is collected. The heat of adsorption can be extracted by subtracting the thermal radiation response from the total heat signal.

During deposition, the amount of metal atoms that do not stick to the surface are measured via QMS. A zero-sticking measurement is taken by directing the metal atom beam onto a hot tantalum flag, which is heated until the metal non-sticking QMS signal is maximized. By comparing the QMS signal from the deposition metal during calorimetry to the total signal obtained from directing the metal pulses at a hot tantalum flag, the number of metal atoms that stick to the sample and contribute to the heat signal can be extracted using a modified version of the King and Wells method.[27,67]

2.4 Growth Morphology Measurement with LEIS

For growth-mode experiments, metal is deposited on the sample in small amounts (typically <1 ML) and the sample is analyzed with He^+ LEIS after each deposition. The incident ion energy of the He^+ ions is 1keV and their scattering angle is 135º. Before and after each deposition of metal onto the sample surface, the flux is measured using the on-axis QCM in the main chamber. The off-axis QCM continuously monitors and records the flux in the beam chamber. The amount of metal deposited onto the sample is calculated by holding constant the ratio between the two fluxes. After each deposition, a He^+ LEIS spectra is recorded for both the substrate and the deposited metal. The signals are normalized by the signals from the clean substrate and from the substrate when it is covered in a multilayer of the deposited metal. Because He^+ LEIS is extremely surface sensitive, and only measures the topmost atomic layer of the sample, the normalized LEIS signals are the fraction of the substrate surface covered by the metal particles (after small corrections for beam-shadowing effects from the edges of the nanoparticles CITE). The fractional coverage data is fit with a growth model to determine particle density and size.

2.5 Figures

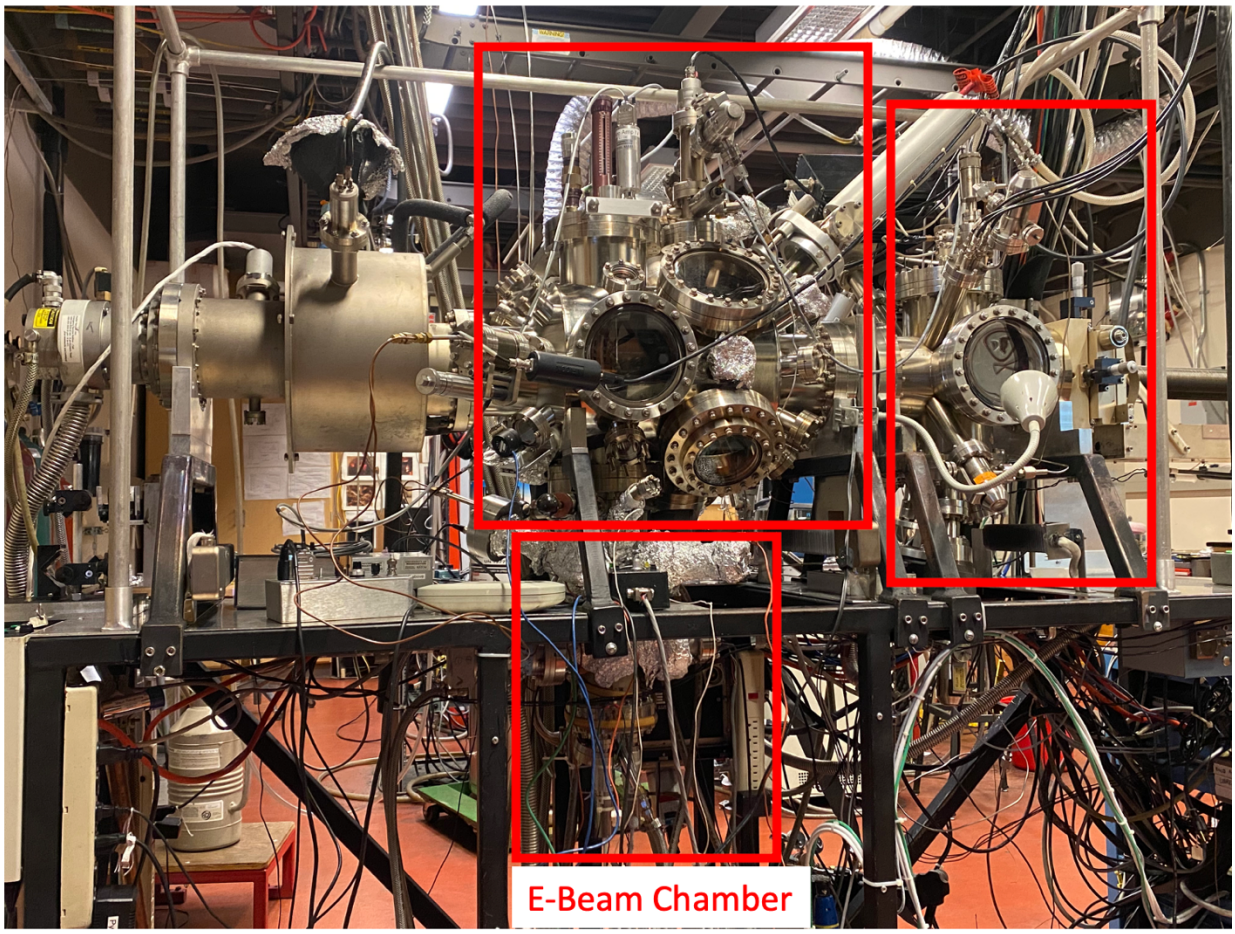

Figure 2.1. A photograph of the metal vapor adsorption calorimeter is shown. The main chamber is in the center box and includes calorimetry equipment as well as surface characterization and analysis instrumentation. The box on the right shows the location of the sample preparation chamber, and the sample manipulator is located to the right of that chamber (extends out-of-frame). The electron-beam chamber is labeled and indicated by the square box below the main chamber. To the left of the main chamber is the titanium sublimation pump and main chamber turbo pump.

Chapter 3. Size-Dependent Energy and Adhesion of Pd Nanoparticles on Graphene on Ni(111) by Pd Vapor Adsorption Calorimetry

This chapter has been published as:

K. Zhao, N. Janulaitis, J. Rumptz, & C.T. Campbell (2023). *ACS Catalysis*, 13(4), 2670-2680.

Chapter Abstract

Carbon-supported late transition metal nanoparticles are promising catalysts and electrocatalysts for wide ranging applications. However, experimental investigations of the bonding energetics of metal nanoparticles on carbon supports are very limited. Here we report heats of adsorption of Pd vapor deposited onto single-layer graphene(0001) supported on Ni(111) at 100 K and 300 K as the Pd grows particles of well-defined size in the range from 3 atom clusters to 6 nm diameter. Sizes were determined from He^+ low-energy ion scattering (LEIS). In this size range, the differential heat of Pd adsorption increases from 228 kJ/mol to within 10 kJ/mol of the heat of sublimation of bulk Pd (377 kJ/mol). The chemical potential of metal atoms in these nanoparticles as a function of average particle size was determined from these results. The adhesion energy at the Pd / graphene(0001)/Ni(111) interface was extracted from these data and found to be 3.5 J/m^2 for the largest Pd particles. For the three metal elements that have now been studied (Pd, Ni and Ag), we found an increase in metal / graphene(0001) / Ni(111) adhesion energy with metal carbophilicity, which we defined here as the heat of C atom adsorption on that metal's (111) surface estimated from published density functional theory calculations.

3.1 Introduction

Late transition metal nanoparticles are widely applied in heterogeneous catalysis in both gas/solid and liquid/solid interfacial reactions, including electrocatalysis, for energy conversion and storage.[68] The metal nanoparticles are hosted normally by oxide or carbon supports. The strength of bonding interactions between the metal nanoparticles and the support materials influence the morphology and energetics of the metal nanoparticles,[17,69,70] which then affect the binding energies of small adsorbates during the catalytical reactions.[71–73] Carbon is a commonly-used support material for late transition metal catalysts and electrocatalysts, which often has superior performance over oxides.[74–78] Recently, carbon has become much more important as a support due to its widespread use in electrocatalysts, fuel cell and battery electrodes, where interest has grown dramatically due to energy storage needs for solar and wind energy technologies. Whether it is in the form of activated carbon, carbon black, modified graphite, carbon nanofibers or carbon nanotubes, the dominant building block in a carbon support's structure is the graphite unit cell.[74]

There have been many investigations of the energetics of the metal atoms and clusters on support materials by Density Functional Theory (DFT), but experimental measurements of the energies of the metal atoms and nanoparticles on support surfaces are far fewer in number. While we have studied the energetics of late transition metal nanoparticles on oxide supports using Single Crystal Adsorption Calorimetry (SCAC) for decades,[19] there have only been two previous experimental measurements of the energetics of metal nanoparticles on any carbon-based supports: our previous reports of the size-dependent energetics and adhesion energies of Ag and Ni nanoparticles on single-layer graphene(0001) supported on Ni(111).[29,36] Here we report a similar study of Pd nanoparticles on that same graphene/Ni(111) surface, and discover a

correlation between the adhesion energy at the metal nanoparticle / support interface (E_{adh}) for these three metals and the metal element's carbophilicity. Carbon-supported Pd nanoparticles are widely used in both basic and applied catalysis and electrocatalysis research.[77–80]

In studies of the energetics of late transition metals on oxide supports, the chemical potential of the metal atoms in the supported metal nanoparticles was found to be a key descriptor of catalyst performance factors, such as sintering rates, adsorbate binding energies and overall catalytic conversion rates.[16,17,19,81] Small sized (<6nm) nanoparticles showed very strong dependence of the metal chemical potential on nanoparticle size. Significantly, the adhesion energy (E_{adh}) can be used to predict the metal chemical potential vs size, and vice versa.[17] E_{adh} of different metals on the same oxide support were found to increase linearly with the oxophilicity of the metal.[20,37] This E_{adh} vs oxophilicity relation allows one to predict the adhesion energy of other metals on that oxide surface, and then determine the chemical potential of the other metals, and thereby to estimate their sintering properties and surface reactivity in catalysis. Here we reveal a similar E_{adh} vs carbophilicity relation for carbon-based supports.

The structure and properties of Pd nanoparticles on carbon support materials (e.g., carbon nanotubes, highly oriented pyrolytic graphite (HOPG) and graphene oxide) have been investigated experimentally under high temperature or catalytic reaction conditions.[80,82–85] Fundamental research studies of Pd nanoparticle growth on pure carbon supports (i.e. graphene, carbon nanotubes, and HOPG) at room temperature have reported the particle shape and size at different Pd deposition amounts.[69,86–90] To our knowledge, there have been no previous measurements of the interaction energies between the Pd nanoparticles and any carbon-based support surface.

Previously, we have investigated the adsorption energies of Ag and Ni during nanoparticle growth on graphene(0001)/Ni(111) using single crystal adsorption calorimetry (SCAC) and low-energy He^+ ion scattering spectroscopy (LEIS).[29,36] In this work, we apply the same methodologies as used there to investigate the size-dependent nanoparticle energetics and growth of Pd on graphene(0001)/Ni(111). We study the growth modes of Pd on graphene(0001)/Ni(111) at 100 and 300 K with LEIS, fitting the measured LEIS signals versus coverage with models that allow us to estimate the average Pd particle size versus coverage. The heat of adsorption of Pd vapor is measured versus coverage during nanoparticle growth on graphene(0001)/Ni(111), and we use that to determine the size-dependent chemical potential of Pd atoms in Pd nanoparticles on graphene(0001)/Ni(111) at 100 and 300 K. Finally, we extract the adhesion energy of Pd / graphene(0001)/Ni(111) and compared it with Ag and Ni, obtaining a strong relation between adhesion energy to this carbon surface and metal carbophilicity.

3.2 Experimental Methods

The experiments were conducted in an ultrahigh vacuum (UHV) chamber with a base pressure < 2×10^{-10} Torr. The chamber is equipped with (1) sample surface preparation needed heaters and ion guns; (2) e-beam evaporator; (3) sample characterization apparatus, including X-ray photoelectron spectroscopy (XPS), Auger electron spectroscopy (AES), He^+ low-energy ion scattering spectroscopy (LEIS), low-energy electron diffraction (LEED), quadrupole mass spectrometry (QMS), and two quartz crystal microbalances (QCMs). The surface spectroscopy measurements were obtained with a PHI 10−360 precision energy analyzer with a PHI 72−250 position sensitive detector; and (4) the calorimeter with a pyroelectric polyvinylidene fluoride (PVDF) ribbon as the sensor.

The single-layer graphene was grown on a clean 1 μm thick Ni(111) single-crystal sample (Aarhus University, Denmark) using a recipe described in previous work,[29] and a complete coverage of graphene on the Ni(111) was confirmed using LEIS each time right after graphene growth.

The Pd metal atom beam was generated by evaporating Pd pellets (99.95%, Kurt J. Lesker) in the e-beam evaporator at a very high temperature (est. 2000 K). The Pd beam was chopped into pulses with a duration of 0.1 s and an interval of 2 s. The Pd flux was monitored with two QCMs in a method described previously to provide the flux at all times at the sample position.[64]

The sticking probability of each pulse was measured simultaneously with the heats of adsorption using the QMS which records the desorbed Pd atoms from the graphene/Ni(111) support.[64] The number of Pd atoms that stick to the sample surface in each pulse is then equal to the flux times the pulse duration and the sticking probability. The Pd coverage is the accumulated amount of adsorbed Pd atoms. The coverage are given here in units of monolayers (ML), with 1 ML defined as 1.87×10^{19} atoms/m^2, which is the areal density of Ni atoms on the underlying Ni(111) surface as well as exactly ½ the areal density of C atoms on the graphene(0001) surface, as there are two C atoms of graphene for every surface Ni atom on Ni(111) for this system.

The growth modes of the Pd nanoparticles were determined using He^+ LEIS, as the normalized LEIS signal is proportional to the surface area of the particles.

The methods for metal vapor adsorption calorimetry are the same as reported previously with this apparatus.[64] The heat change during the Pd vapor deposition onto graphene/Ni(111) is measured using a pyroelectric polyvinylidene fluoride (PVDF) ribbon which contacted the back

of the thin Ni(111) single-crystal sample. The PVDF ribbon is calibrated for each experiment using a HeNe laser pulses with known power. To eliminate the heat contribution from the thermal radiation from the hot metal source, the heat from the radiation is measured when a barium fluoride (BaF_2) window is placed in front of the sample to block Pd vapor from reaching the sample but allowing > 87% thermal radiation to transmit through the window. The heat signal from this transmitted fraction is measured and then subtracted from the total heat signal measured for each Pd pulse that adsorbs on the graphene/Ni(111).

3.3 Results

3.3.1 Pd Sticking Probability on Graphene/Ni(111)

The sticking probability of Pd gas atoms to graphene/Ni(111) during the Pd particle growth was measured as the fraction of Pd atoms that strike the surface and stick using the QMS and the modified King and Wells method (see above). The QMS data is recorded as the time-integrated signal for the Pd isotope with the strongest QMS signal) for each Pd vapor pulse during the calorimetric measurements. This QMS signal was normalized by the zero-sticking signal for Pd atoms, which was measured by pulsing the Pd vapor beam onto a hot flat tungsten foil, where no permanent sticking occurs and the Pd QMS signal reaches the maximum, as described previously by our group.[27,64] The sticking probabilities (equal to 1 minus this ratio) were found to be > 0.997 at all Pd coverages at both 100 K and 300 K (not shown). Therefore we used unity as the sticking probability to calculate the accumulated Pd coverage for all calorimetry and growth mode experiments described below.

The Pd coverages reported here are given in units of ML, with 1 ML defined as 1.87×10^{19} atoms/m^2, which is the areal density of Ni atoms on the underlying Ni(111) surface as well

as exactly 1/2 the areal density of C atoms on the graphene(0001) surface, which grows in registry with the Ni(111) substrate.[65,91]

3.3.2 Pd Growth Morphology on Single-Layer Graphene on Ni(111)

The growth morphology of Pd on graphene/Ni(111) at 100 and 300 K was determined using He^+ LEIS measurements, as this LEIS signal is sensitive only to the topmost surface atomic layer. The Pd signal thus rather directly reflects the fraction of the surface covered by Pd nanoparticles (after correction for shadowing effects[61]). Here, we deposited Pd in discrete amounts and measured the Pd LEIS signal after each dosage. A thick Pd layer (>10 nm) was deposited at the end of each experiment for collection of the saturated LEIS signal associated with a Pd film that completely covers the graphene. Each LEIS spectrum was integrated in the range of the Pd peak (850 – 950 eV), and then normalized to the integrated saturation signal of this thick Pd layer. This normalized Pd LEIS signal equals the fraction (f) of the surface covered or shadowed by Pd particles. These normalized Pd LEIS signals are plotted versus Pd coverage in Figure 3.1a for growth at both 100 and 300 K.

Studies by scanning tunneling microscopy (STM) of Pd deposition on single-layer graphene on other closest-packed later transition metal surfaces (Cu(111)[86] and Ru(0001)[87]) show that when deposited at room temperature, the Pd forms 3D islands with rather flat tops and small aspect ratios (α = average thickness / diameter = ~0.22). We will therefore analyze the LEIS data at 300 K in Figure 3.1 assuming that the Pd grows as particles with the approximate shape of a flat cylinder, with an (approximately) constant aspect ratio of 0.22 and a fixed number per unit area. Detailed analysis (see below) shows that the aspect ratio actually decreases slowly with particle size (or the average particle thickness stays more constant with coverage) than in

the ideal case where the aspect ratio is truly constant. The flat-topped shape of Pd particles was also seen in STM on highly oriented pyrolytic graphite (HOPG) surface[88] at room temperature, and also at higher temperatures (400 K on graphene[82] and 700 K on HOPG[84]). When Ni is deposited on this same graphene(0001)/Ni(111) surface at room temperature, it also grows rather flat-topped islands with small aspect ratios and fixed number per unit area.[92,93] The kinetic reasons for such a growth mode have been explained.[36,94,95]

At 100 K, the number of Pd particles per unit area is 6.5-fold larger than at 300 K (see below), so that they are 6.5-fold smaller than at 300 K for the same coverage, and they do not have the possibility to grow so large (remaining thinner than 0.8 nm) in the low coverage range where the LEIS data can be quantitatively analyzed (i.e., when the covered/shadowed fraction f is < 0.35, see below). We are therefore able to analyze the LEIS data at 100 K in Figure 3.1 assuming the more commonly used hemispherical cap model, whereby the metal nanoparticles are assumed to have the approximate shape of hemispherical caps. Note that the average thickness to diameter ratio for hemispherical caps is 1/3. This larger aspect ratio for these much smaller particles than the value of ~0.22 seen for the larger particles at 300 K is consistent with the decrease in aspect ratio with size mentioned above.

Both of these models assume a constant number of particles per unit area independent of metal coverage in the coverage range modelled).[61] This is the so-called "saturation number density" which is often reached at very low coverage (a few percent of a monolayer),[61] as explained by the kinetic models for nucleation and growth during metal vapor deposition developed by Venables.[96] At high coverage, the growing particles get so large that they start to overlap and eventually merge into a continuous film. We avoid this regime (where the number density of particles decreases) when modelling the LEIS data of Figure 3.1 quantitatively by only

fitting data below the coverage where the metal particles cover 35% of the surface (i.e., when f < 0.35).

As derived previously for the hemispherical cap model,[61] the relationship between this covered/shadowed fraction (f), the particle size and total metal coverage is given by:

$$f_{hemisphere} = 1.207\,\pi\,{r_{hemisphere}}^2 = 1.207\,\pi^{1/3}\left(\frac{3V_m}{2N_A}\right)^{2/3}\,{n_{np}}^{1/3}\,{n_m}^{2/3}, \text{ with} \quad (1)$$

$$r_{hemisphere} = \left(\frac{3V_m\,n_m}{2\pi\,N_A\,n_{np}}\right)^{1/3},$$

where 1.207 is the LEIS shadowing factor for a hemispherical cap on the substrate when the ion beam is normal to the surface and the detector is at 45° from the normal to the surface (the geometry used here), $r_{hemisphere}$ is the footprint radius of the particle's contact interface with the support (the same as its radius of curvature for hemispherical shape), V_m is the molar volume of bulk solid metal ($8.84 \times 10^{-6}\ m^3/mol$ for Pd), N_A is Avogadro's number, n_{np} is the number of particles per unit area, and n_m is the total number of the metal atoms per unit area that were deposited onto the substrate at that coverage being analyzed by LEIS.

As shown, the Pd LEIS signal versus Pd coverage at 100 K in Figure 3.1a is well fitted to this hemispherical cap model, with the number of particles per unit area (n_{np}) as the only fitting parameter. [61,96,97] The best fit, shown by the solid line, gives a particle density 5.5 × 10^{16} particles/m^2. The dotted line starting from the end of this fitted line is to guide the eye.

The Pd average thickness for the hemispherical shapes is calculated from the normalized LEIS signal and the corresponding coverage in Figure 3.1a. In detail, the coverage (in ML, 1 ML = 1.87 × 10^{19} atoms/m^2) is converted back to the number of deposited Pd atoms per unit area. Multiplying this number by atomic volume gives the total volume of the deposited Pd per unit

area at that coverage. Dividing this by the fraction of the surface that is covered by Pd particles (i.e., the normalized LEIS signal on the y axis of Figure 3.1a divided by the shadowing factor[61] of 1.207) gives the average Pd particle thickness. This is plotted as a function of Pd coverage in Figure 3.1b. The average diameter of hemispherical particles is three times the average thickness (calculated from the volume of a hemisphere divided by its footprint area). The resulting average diameter at 100 K vs Pd coverage is plotted Figure 3.1c. These average thickness and diameter estimate at 100 K agree well with the predictions shown for the best-fit hemispherical cap model from Figure 3.1a at 100 K.

For the particles grown at 300 K, the data are fitted to a constant aspect ratio model, which assumes the particles have the approximate shape of cylindrical disks with a constant aspect ratio (α = average thickness / diameter = 0.22) and a constant number density of particles. This constant aspect ratio model has been successfully applied to analyze similar He^+ LEIS data in previous studies of Au/MgO(100) and Ni/CeO_{2-x}(111).[42,43]

The expression for the covered/shadowed factor (f) for the constant aspect ratio model is slightly different from the hemispherical cap model, due to a change in the shadowing factor for the normalized LEIS signal from the particles. The shadowing factor is $1 + 4\alpha/\pi$ for the cylindrical disk,[98] whereas it was 1.207 for the hemispherical cap (see above). Although not explicitly stated in the paper where this shadowing factor was first presented,[98] the approximate cylindrical disk shape assumed in that derivation was not exactly cylindrical. The edges around the perimeter of the disk were not assumed to be perpendicular to the support surface, but at some small angle from normal, such that the flat top of the particle is slightly smaller than its flat bottom, as a truncated cone. Thus, the ion beam, which is incident perpendicular on the support surface, strikes the edges of the disk (and not only its top surface, which would be the case if the

disk's edges were normal to the support surface). As the normalized LEIS signal from the particle and from the support sum to one,[61,99] the normalized LEIS for the particle element is equivalent to the fraction of support surface that is covered and shadowed by the particles. The fraction of the support surface that is covered and shadowed by the cylindrical objects is approximately the same as that by the truncated cone objects. Therefore, the shadowing factor calculation can be simplified by using the cylindrical geometry.

The relationship between this covered/shadowed fraction (f), the particle size and total metal coverage is given for this disk model by:

$$f_{disk} = \left(1 + \frac{4\alpha}{\pi}\right)\pi\, {r_{disk}}^2 = \left(1 + \frac{4\alpha}{\pi}\right)\pi^{1/3}\left(\frac{V_m}{2N_A\,\alpha}\right)^{2/3}\ {n_{np}}^{1/3}\,{n_m}^{2/3},$$
$$r_{disk} = \left(\frac{V_m\, n_m}{2\pi\, N_A\, \alpha\, n_{np}}\right)^{1/3}. \quad (2)$$

Thus, the normalized LEIS signal increases as the 2/3 power of the metal coverage (n_m) within this constant aspect ratio model, just as in the hemispherical cap model (Eq. 1). The 300 K data in Fig. 3.1(a) is fitted with Eq. 2 up to $f_{disk} = 35\%$ (1.5 ML). The dashed line starting from the end of the fitting line is to guide the eye. The best fit to this constant aspect ratio model for the 300 K LEIS data gives a particle density 8.5×10^{15} particles/m^2. The average Pd particle thickness for the cylindrical shape is calculated from the normalized LEIS signal and the corresponding coverage in Figure 3.1a, just as explained in the hemispherical cap model above. The Pd diameter is calculated as the aspect ratio (0.22) times this average thickness. The resulting average Pd particle thickness and diameter as a function of Pd coverage are shown in Figure 3.1b and 3.1c. These average thicknesses and diameters at 300 K agree reasonably well with the constant aspect ratio model, also shown, although it is clear that the measured particle

thickness is more constant with coverage, and larger at low coverage, than predicted by the best constant-aspect-ratio fit.

The particle sizes shown in Figure 3.1b and 3.1c at 300 K are supported by STM observations on the growth morphology of Pd on graphene from the literature.[86,87] Pd was grown from vapor deposition at room temperature and formed flat-topped particles in both these two STM works. Gotterbarm, *et al*.[87] showed Pd vapor deposited on graphene/Rh(111) at room temperature has particle diameters of 3.0±0.3 nm and heights of 0.66±0.1 nm at 0.3 ML, which gives an aspect ratio of 0.22. Similarly, Soy, *et al*.[86] showed Pd particles has diameter of ~3.6 nm at 0.29 ML on graphene/Cu(111). Unfortunately the height was not presented there. Instead, the diameter and height at 0.9 ML were shown in a distinctly continuous deposition experiment, where the Pd grown as much flatter islands, with the average height of ~1.3 nm (four to five atomic layers) and diameter of 7.8 nm. The height of Pd particles on graphene after annealing to 400 K was measured as 0.8 – 2 nm at 1 ML.[82] Our Pd particles deposited at 300 K showed an average height of 1.2 nm at around 1 ML (Figure 3.1b), consistent with those STM observations. The flat-topped shape can be attributed to the (111) facet of the face-centered cubic (FCC) Pd formed at the particle bottom where contacts with the graphene(0001) surface and the adatoms on the top follow the closest packed structures of metal (111) at the thermal equilibrium.

A flatter cylindrical shape was also tested in our analysis for the 300 K LEIS data by assuming the aspect ratio equals to 0.2 (not shown). This smaller aspect ratio results in a smaller particle density (7.4×10^{15} particles/m^2) in the best fit. The standard deviation of the fittings for the normalized LEIS signal vs coverage and height vs. coverage were the same as those in the fittings with $\alpha = 0.22$. Nevertheless, the standard deviation of the fitting for diameter vs coverage was ~10% larger when compared with the fitting with $\alpha = 0.22$. Additionally, noting that the Pd

average thickness at 300 K below 0.7 ML (Figure 3.1b) was approximately constant, with average value of 1.0 nm. We applied a constant height model to the LEIS data at 300 K for the coverage < 0.7 ML. The fitting is a straight line for the normalized LEIS signal vs coverage, with slightly smaller standard deviation than that in the constant aspect ratio model (0.0145 vs 0.0270). However, the LEIS signal in the constant height model is not related in any way to the particle diameter nor density. By combining the aspect ratio reported from STM studies with the LEIS results in the constant aspect ratio model, we are able to extract diameter and density, so we prefer that model, while recognizing that it is approximate.

3.3.3 Heat of Adsorption of Pd on Single-Layer Graphene on Ni(111)

The heat of adsorption at any temperature T is defined here as the negative of the standard enthalpy change from an initial state consisting of a collection of gaseous metal atoms and a support surface, both at T, and a final state where the metal atoms are confined to the support at T. The heats of adsorption are obtained by the measurement of calibrated calorimeter's signal (internal energy change) which is then converted to the enthalpy change.[32] The Pd heats of adsorption were measured upon Pd gas atoms deposition onto graphene/Ni(111) as a function of Pd coverage at 100 and 300 K. The curves shown for 300 and 100 K are averaged from several individual calorimetry runs to ensure replicability and to reduce the standard deviation in the measurement. The shown heats of adsorption are corrected from the small difference in internal energy between a *flux* of gaseous Pd atoms initiating from a high-temperature electron beam evaporator and a collection of the same gas atoms in an equilibrated *volume* at the support surface temperature (300 or 100 K).[27,100] Due to errors (~3.5%) in calibrating the calorimeter's absolute heat signal with laser pulses, we adjusted this calibration

factor slightly to ensure that the heat of adsorption and corresponding Pd chemical potential to agree with the theoretical model described below for chemical potential versus particle size at the largest particle sizes analyzed (~6 nm). At this large size, the theoretical value is nearly independent of the fitting parameter in the model, so we realized that this is the most accurate way to calibrate heat sensitivity in our calorimeter.[17] Previously, we had calibrated by setting the highest-coverage (thickest multilayer) heat of adsorption equal to the bulk heat of sublimation. However, due to small changes after long times (20 – 30 minutes) in the atomic beam flux and the accuracy of its off-axis measurement, we realized it is more accurate to use this lower-coverage, shorter-time measurement for calibration, before these flux problems get more significant. This resulted in heats of adsorption at 300 K and 2 ML, where the heats approached a constant level, agreeing within 3 kJ/mol of the known heat of sublimation of bulk Pd (ΔH_{sub} = 377 kJ/mol[46–48]). The same occurs at 100 K at 3 ML, with this higher coverage required due to the much smaller particle sizes than at 300 K. At 300 K, this calibration method gave heats that were 3.5 % higher than the old method, and at 100 K the difference was negligible.

As shown in Figure 3.2a, at 100 K, the initial differential heat of adsorption is 228 kJ/mol, then gradually increases with coverage to the heat of sublimation of bulk Pd (ΔH_{sub} = 377 kJ/mol) by 3 ML. At 300 K, the data develops very similar to the 100 K data, except that the heat of adsorption starts higher (273 kJ/mol) and reaches Pd heat of sublimation already by 2 ML.

The increasing heat of adsorption with coverage is due to the fact that more Pd-Pd metal bonds form when new Pd adatoms arrive at larger Pd particles on the substrate. This increasing binding energy with increasing particle size is commonly found in DFT calculations as well, wherein, for example, the binding energy (per Pd atom) of Pd to unsupported Pd clusters and Pd

clusters on a carbon support nearly doubles from Pd_3 to Pd_{13}.[49] When the Pd particles grow large enough, the heat of adsorption approaches the heat of sublimation (ΔH_{sub}) of 377 kJ/mol, which corresponds to making 6 Pd-Pd bonds in a simple pairwise bond-additivity model.

At any given coverage below 1 ML, the Pd heats of adsorption at 100 K are lower than the those at 300 K. This is attributed primarily to Pd particle size differences between these two temperatures. As shown in Figure 3.1b and c, Pd particles at 100 K have 6.5-fold larger number density, and therefore 6.5-fold fewer Pd atoms, than at 300 K for any given coverage. For example, at 0.5 ML, the Pd particle diameter at 100 K is ~2 nm while it is ~5 nm at 300 K. When a new adatom arrives, fewer Pd-Pd bonds form on the smaller particle surface as smaller particles have a much larger fraction of undercoordinated atoms, therein less nearest neighboring atoms to form Pd-Pd bonds. In comparison, the larger, flat-topped (herein, faceted) particles formed at 300 K have more nearest neighboring atoms to form more Pd-Pd bonds when a new adatom reaches the particle surface.[36] This continues until the hemispherical caps at 100 K grow sufficiently large that they are dominated by sites where new Ni atoms can make as many Ni-Ni bonds upon adsorption as at 300 K (~3 ML of Pd coverage).

Figure 3.2(b) shows the differential heat of adsorption plotted versus average particle size. As seen, the heats for a given particle size at 300 K are closer to those at 100 K, but differences are still present due to the difference in particle shape.

3.3.4 Pd Chemical Potential Versus Particle Size and Adhesion Energy of Pd onto Graphene/Ni(111)

Chemical potential of the metal atoms (μ) is the most accurate way to express the thermodynamic stability of the metal atoms supported particles. Since the entropy change with

particle size is very small compared to the large enthalpic changes seen in Figure 3.2b, the chemical potential is calculated here considering only these enthalpy changes. [37] The chemical potential of Pd in its particles on graphene/Ni(111) here will be referenced to the bulk Pd(solid) large-size limit. So it was calculated by simply subtracting the measured differential heat of adsorption at each data point from the bulk heat of sublimation.[18] The resulting Pd chemical potential is plotted as a function of the average diameter of the Pd particles in Figure 3.3. As seen, the Pd chemical potential at 100 K begins at ~150 kJ/mol then rapidly decreases with the particle diameter. The analysis for 100 K data ends at 2.7 nm (1 ML) which is the large-coverage limit analyzed in the LEIS growth model for 100 K. At 300 K, the Pd chemical potential is higher than at 100 K at the same particle size, and decreases more slowly with size than at 100 K. This is due to the difference in particle shape (see below). The analysis for 300 K data ends at 6 nm (1.2 ML), which is also the high-coverage limit of the LEIS growth model analysis for 300 K.

The adhesion energy (E_{adh}) of the metal/support (the Pd/graphene here) interface can be determined with these experimental values of chemical potential versus size. The theoretical relationships between chemical potential, particle size, and the adhesion energy at the metal particle / support interface were firstly derived in the previous publications,[18,37] and are shown in Eq. (3) here for the hemispherical assumption for the 100 K data and Eq. (4) for the cylindrical assumption for the 300 K data. The difference between Eq. (3) and (4) are originated from the mathematical expressions in the total surface area and volume of the particles in the hemispherical cap versus cylindrical disk geometries.

$$\mu_{hemisphere}(D) = (3\gamma_m - E_{adh})\left(1 + \frac{D_0}{D}\right)\left(\frac{2V_m}{D}\right), \quad (3)$$

$$\mu_{disc}(D) = [2(2\alpha + 1)\gamma_m - E_{adh}]\left(1 + \frac{D_0}{D}\right)\left(\frac{2V_m}{3\alpha D}\right), \quad (4)$$

where γ_m is the surface free energy of the bulk metal (1.98 J/m^2 for Pd[37]), and $(1 + D_0/D)$ with $D_0 = 1.5\ nm$ is an empirical factor that was found to account for the increase in γ_m and E_{adh} (relative to their bulk values) when the particle size decreases.[17] Note that E_{adh} in both equations corresponds to the limit of large particle size.

E_{adh} is the only unknown variable in this equation and can be determined by the best fit of the measured Pd chemical potential as a function of the Pd diameter. The fittings for 100 K and 300 K data are shown as solid lines in Figure 3.3. They show good agreement with the data points versus particle size. The fits and measurements meet at large particle size, as the chemical potential approaches to the bulk Pd energy in the large size limit. The best fits to the hemispherical and cylindrical assumptions give E_{adh} = 3.54 and 3.44 J/m^2, respectively. These are so close that we show here the fitting of both temperature to a single value of E_{adh} equal to 3.5 J/m^2. Omitting the very first (lowest coverage) data point (since it may be dominated by defect sites), the standard deviations of the data points from the models are 3.070 and 5.580 kJ/mol at 100 K and 300 K, respectively.

The adhesion energy can also be calculated from a three-step thermodynamic cycle for the largest particle analyzed, as shown previously:[18,29]

$$\sum_n \Delta H_{ads} = -n\Delta H_{sub} + A[(1 + f)\gamma_m - E_{adh}]\left(1 + \frac{D_0}{D}\right), \quad (5)$$

where $\sum_n \Delta H_{ads}$ is the integrated enthalpy of metal adsorption (negative heat of adsorption) for n moles of metal, A is the interfacial area between the metal nanoparticle and the support surface, and f is the surface roughness factor of the nanoparticle (exposed surface area/A). For

hemispheres, f = 2. This method is applied to the hemispherical caps at 100 K and extracted the E_{adh} = 3.37 J/m^2.

This is very close to the average of the Pd adhesion energy acquired above of 3.5 J/m^2. This value is very close to Ni adhesion energy (3.6 J/m^2) on graphene/Ni(111) in our previous study.[36] As discussed further below, DFT calculations have shown that the adsorption energies of Pd atoms and clusters on graphene are similar to those of Ni atoms and clusters on graphene,[101–104] consistent with our results.

3.4 Discussion

3.4.1 Comparison of Heats of Adsorption and Adhesion Energy with DFT Results

Our measured adhesion energy of Pd to graphene/Ni(111) of 3.5 J/m^2 can be compared to the adhesion energy of Pd(111) to a free standing graphene sheet calculated by DFT to be 0.50 – 0.53 J/m^2 (0.084 – 0.089 eV/C atom, with 3.74 x10^{19} C atoms/m^2).[103,105] A similar large difference was also seen when comparing the adhesion energy of Ni to graphene/Ni(111) we measured[36] of 3.6 J/m^2 and that calculated by DFT[92] of 3.47 J/m^2 to the adhesion energy of Ni(111) to a free-standing graphene sheet calculated by DFT to be 0.81 J/m^2. This huge difference indicates that there are strong Ni-Ni attractions between the Ni(solid) on both sides of the graphene, i.e., long-range attractions across the intervening graphene, not existing for Ni on free-standing graphene. The similar effect we see here for Pd indicates that there are similarly strong Pd(solid)-Ni(111) attractions also across the intervening graphene, not existing for Pd on free-standing graphene.

The binding and adsorption energies of small Pd clusters on free-standing graphene have been calculated with DFT.[101,104,106,107] To compare the energies of similar-size Pd clusters in our

experiment with the DFT results, we calculated the average number of Pd atoms per particle in our 100 K experiment by dividing the Pd coverage (numbers of deposited atoms per unit area) by the number density of the particles. For example, the first three data points in Figure 3.2 at 100 K give ~4, 11 and 18 atoms per particle, respectively. Since those DFT results are presented as the energy difference between gas phase Pd atoms and the cluster bound to graphene at 0 K, this corresponds closely to the integral heat of adsorption at 100 K (minus RT, which is only 0.8 kJ/mol at 100 K so neglected here). In Figure 3.4a, we replot the differential heats versus coverage at 100 K from Figure 3.2a as integral heats versus coverage. Figure 3.4b presents those same integral heats now versus the average Pd particle size (in numbers of Pd atoms). The DFT energies are systematically lower than the integral heats for Pd by 20 to 50 kJ/mol for the same cluster size in the range from 4 to 13 atoms, with the difference decreasing with size. This comparison is made using only heats measured at 100 K simply because the 300 K data do not extend to such small sizes. The smallest size measured at 300 K corresponds to 15 atoms, and the integral heat here was 273 kJ/mol. This 300 K point is nearly midway between the second and third points measured at 100 K in Fig. 3.4(b), and again ~20 kJ/mol higher than the trend in DFT values.

Since the energy per atom in larger clusters is dominated by Pd-Pd bonds, this decrease in the difference between our heats and these DFT estimates with increase in cluster size suggests that DFT is getting the Pd-Pd bonding more accurately, but underestimating the strength of binding between Pd and the support (graphene/Ni(111) in our experiments, but only free-standing graphene in the DFT studies). Our larger heats of adsorption versus DFT could originate from the interaction between Pd and the underlying Ni(111) surface below the graphene (not present in these DFT calculations), just as noted above to explain the higher metal

adhesion energies to graphene/Ni(111) compared to free-standing graphene. However, these tiny clusters have quite different electronic properties than the large metal particles used for these adhesion energy comparisons, so the through-graphene metal-metal attractions could be very different. DFT calculations of Pd clusters on graphene supported on Ni(111) would be helpful to perhaps clarify this.

In Figure 3.4, we also present our previously reported integral heats of adsorption for Ni on graphene/Ni(111) at 100 K[36] versus coverage (a) and average cluster size (b), for comparison to Pd. We also show there the reported DFT results for Ni clusters on free-standing graphene.[106,108,109] As seen, the Ni heats are always slightly higher than those for Pd at the same coverage, but they are slightly lower than those for Pd when compared at the same cluster size. This is because the clusters for Ni are larger than for Pd at the same coverage (due to the smaller number density of clusters for Ni at 100 K[36]), yet atoms in small Pd clusters bind slightly more strongly when compared to Ni at the same cluster size. Since Pd has a 13% lower heat of sublimation than Ni, Pd-Pd bonds are expected to be ~13% weaker than Ni-Ni bonds, so this small difference for small clusters is dominated by the stronger bonding of the metal clusters to the graphene/Ni(111) surface for Pd compared to Ni, at the same tiny cluster size.

Opposite to the case for Pd, the DFT energies for Ni on free-standing graphene are 20–50 kJ/mol higher than the experimental integral heats of adsorption at the same cluster size (around 6 to 10 atoms). We note that in our previous publication about Ni on graphene/Ni(111),[36] we made an error in calculating the smallest Ni cluster size measured in the first gas pulse, and stated it incorrectly there as being ~13 Ni atoms. As seen in Figure 3.4b, it is actually only ~6 Ni atoms, but this does not change this qualitative difference compared to DFT. We have no explanation for this surprising difference compared to DFT for small Ni versus Pd clusters.

Most surprising perhaps is the fact that the DFT energies for both Pd and Ni clusters on free-standing graphene are not a lot smaller than the experimental energies on graphene/Ni(111). The huge long-range attractive bonding to the underlying Ni(111) noted above in the comparison of adhesion energies (in the large-particle-size limit) seems to play a much smaller role for cluster sizes in this size range below 10 atoms for both Ni and Pd. This may be compensated on free-standing graphene by the fact that its carbon atoms are not locked in place by strong interactions with underlying Ni(111), and thus they can move their positions more freely to optimize bonding to these small metal clusters. Similarly, their strong bonding to the underlying Ni(111) for the graphene/Ni(111) case causes the C atoms to be lower in energy by ~58 kJ/mol compared with free-standing graphene.[36] This lowering of the C atom energy (chemical potential) is expected to weaken the local bonding of these C atoms to the metal atoms in such adsorbed clusters.

We note that these published DFT results summarized in Figure 3.4 were not all calculated with a similar level of description and accuracy. Specifically, the methods used for Pd clusters were: PW91 (refs.[101,104]) and PBE (ref.[106]), none with any vdW corrections. Those for Ni clusters were: PBE (refs.[106,108]) and PBE with vdW corrections (ref.[109]). Independent of these differences between DFT methods, the DFT adsorption energies for making clusters of Pd are consistently 25-50 kJ/mol lower than measured by calorimetry, and the DFT adsorption energies for making clusters of Ni are consistently 15-40 kJ/mol higher than measured by calorimetry.

3.4.2 Trend of Adhesion Energy of Metals on Single-Layer Graphene on Ni(111)

In previous work, the adhesion energies of large nanoparticles of different metal elements to metal oxide supports (MgO(100) and CeO_{2-x}(111)) have been found to increase linearly with

the metal oxophilicity. Campbell and Sellers defined the metal element's oxophilicity as the heat to convert one gaseous metal plus O2 to the most stable oxide of that metal (per mole of metal).[20,37] This is estimated from tabulated experimental heats as: ($\Delta H_{sub,M} - \Delta H_{f,MOx}$), where $\Delta H_{sub,M}$ is the metal's bulk sublimation enthalpy (per mole of metal) and $\Delta H_{f,MOx}$ is the standard heat of formation of the most stable oxide of the metal (per mole of metal)) per unit area.[17,18] We expect a similar trend of increasing adhesion energy of the transition metals on graphene/Ni(111) support versus metal carbophilicity. Since heats of formation of bulk carbides are known for very few elements, we define the carbophilicity of metal elements here as the negative binding energy of a C atom on the metal surface, through the chemical reaction C(g) + M(s) → C*-M(s), meaning negative of the ΔU for adsorbing a gaseous C atom per unit area. Since experimental values are not available, we estimate this ΔU, which we will call $\Delta U_{ad,C}$, using DFT calculated results at zero Kelvin, as described below.

To calculate this energy, we separate this chemical reaction into two reaction steps:

(1) $CO(g) + M(s) + H_2(g) \rightarrow C^*\text{-}M + H_2O(g)$, and

(2) $C(g) + H_2O(g) \rightarrow CO(g) + H_2(g)$, which sum to give:

NET: $C(g) + M(s) \rightarrow C^*\text{-}M(s)$.

DFT calculations of the energies for the formation of C* at four-fold step sites on the M(211) surface, via the first chemical reaction above, have been reported for M = Ag, Cu, Pd, Pt, Rh, Au, Ni, Ir, Ru at zero Kelvin, all done with the same RPBE functional and DFT methods.[110] The reaction enthalpy of the second reaction above was calculated using the standard enthalpies of formation of each gas molecule at 298 K from NIST web chemical book[111] (-241.83, 716.68, -110.53 and 0 kJ/mol for $H_2O(g)$, C(g), CO(g) and $H_2(g)$, respectively). From these, the

experimental enthalpy change for this second reaction is -585.38 kJ/mol at 298 K. We use this as an estimate of the internal energy change for this second reaction at 0 K. Summing these two energies from these two reactions gives ΔU for the net reaction to make a C adatom form a C gas atom at 0 K, which we define here as that metal's carbophilicity. This carbophilicity in kJ/mol is then divided by Avogadro's constant (N_A) and the area per surface metal atom (estimated as $\Omega_M^{2/3}$, where Ω_M = volume per atom in bulk metal) to convert to J/m^2, for correlating with E_{adh}, which is also in J/m^2.

Figure 3.5 shows the adhesion energy of Pd on graphene/Ni(111) from this work and those for Ni and Ag from our previous studies (3.6 and 1.8 J/m^2, respectively)[29,36] plotted versus this carbophilicity per unit area. As shown, the best linear fit of these adhesion energies to carbophilicity per unit area gives: E_{adh} = 0.130 × carbophilicity/area + 0.69 J/m^2. This fitting line allows us to estimate the adhesion energies of other metals that lack measurements. As shown by the red data points in Figure 3.5, the estimated E_{adh} for Au, Cu, Pt, Ir, Rh and Ru are 1.97, 2.82, 2.99, 3.28, 3.39, 3.68 J/m^2, respectively. The reliability of this type of estimation method was proven in our reported E_{adh} versus oxophicility relation[17,18,37,112,113] by accurately predicting the values for Ni before they had been measured.[18]

It is interesting that the slope of this line (0.13) is very similar to the slopes of adhesion energy versus oxophilicity per unit area of 0.18 and 0.14 for these metals on MgO(100) and CeO_2(111), respectively.[18] It is clear from these slopes that only a small fraction (10-20%) of these intrinsic C-M or O-M bond energies can be used in making the adhesive bond energy at these solid metal / support interfaces. This is due to all the other bonds that the surface atoms simultaneously make to other atoms in their solid, and lattice mismatch at the interface, both of which limit their ability to optimize metal bonding to carbon atoms across the interface.

Just as the adhesion energy of Ag to graphene/Ni(111) here is much weaker than that of Pd and Ni, so too is its monomer adsorption energy on this surface. This is evidenced through the initial sticking probabilities at 300 K, which is only 75% for Ag,[29] but nearly unity for Ni[36] and Pd. The relationship between metal vapor sticking probability and heat of metal monomer adsorption has been discussed.[29]

3.5 Conclusions

Growth morphology and calorimetric adsorption energies of Pd vapor deposited onto graphene/Ni(111) were measured using the He^+ LEIS and SCAC. The chemical potential of Pd nanoparticles as a function of Pd nanoparticle size were derived from the differential heats of adsorption and growth mode measurements. The adhesion energy of Pd nanoparticles to graphene/Ni(111) were extracted from the chemical potential vs diameter relation.

Pd vapor deposition on graphene/Ni(111) at 100 K and 300 K have nearly unit (>0.997) sticking probabilities. At 100 K, Pd grows as hemispherical caps on graphene/Ni(111) with a particle density of 5.5×10^{16} particles/m^2, and at 300 K as flat-topped islands with a constant aspect ratio of 0.22 and a particle density of 8.5×10^{15} particles/m^2. The heat of adsorption of Pd nanoparticles at 100 K initiated at 228 kJ/mol, then increased as the particles grow upon continuous deposition until it saturates near the sublimation energy of bulk Pd metal above ~2.5 ML. The heat of adsorption of Pd nanoparticles at 300 K started from 273 kJ/mol, then increased to near the sublimation energy of bulk Pd metal by ~2.0 ML.

The Pd chemical potential as a function of average Pd particle diameter (from 0.6 to 2.7 nm at 100 K and 1.0 to 6.2 nm at 300 K) was determined from the heats of adsorption. By fitting the measured chemical potential as a function of diameter using the hemispherical cap model for 100 K growth and the cylindrical disk model for 300 K, we determined an adhesion energy of

3.5 J/m^2 for Pd nanoparticles (in the large-size limit) on graphene/Ni(111). This adhesion energy is higher than that the Ag (1.8 J/m^2) nanoparticles and slightly lower than the Ni (3.6 J/m^2) nanoparticles on the same support from previous work.

This result for Pd, in conjunction with the reported adhesion energies for Ag and Ni nanoparticles on graphene/Ni(111), show that these adhesion energies increase with metal carbophilicity. The adhesion energy of other metals on graphene(0001)/Ni(111) are estimated here assuming that this increase is linear. These measured energies provide benchmarks for developing more accurate computational tools and to clarify structure−function relationships of these nanomaterials in heterogeneous catalysis.

3.6 Figures

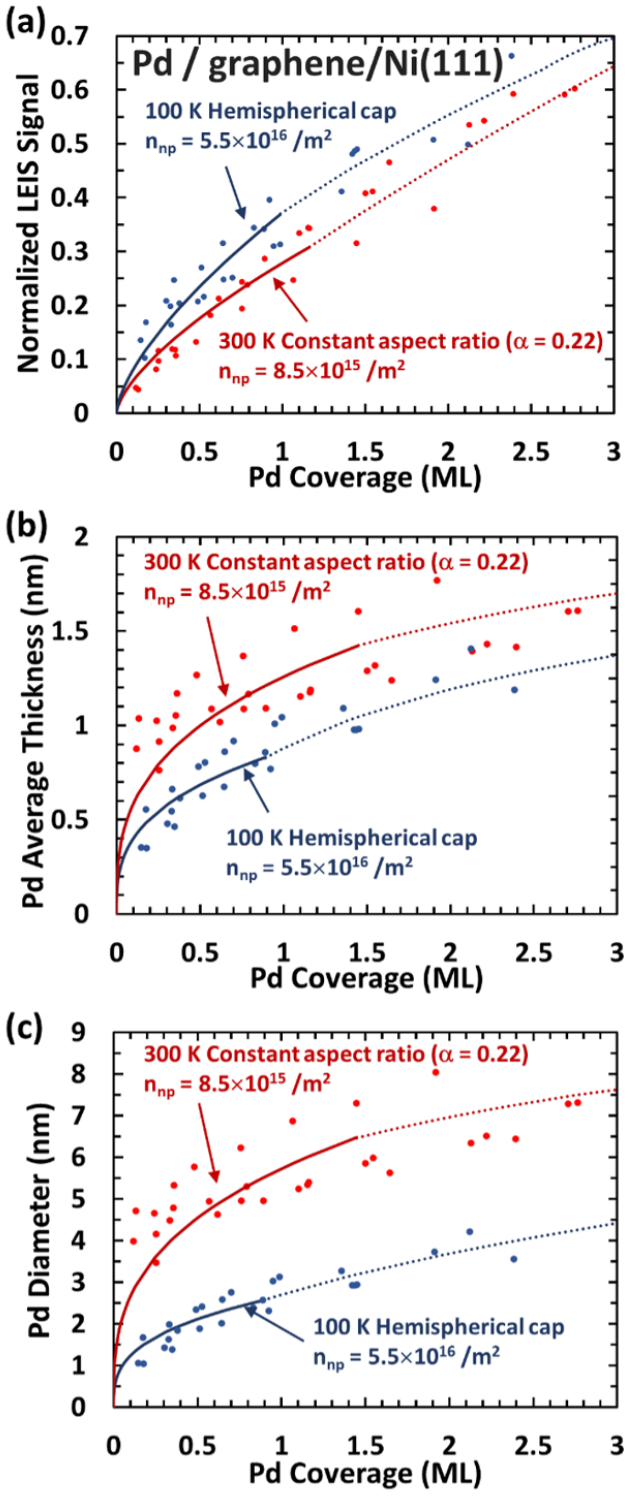

Figure 3.1. (a) Integrated Pd LEIS signal (normalized to the saturated Pd signal for a thick, continuous Pd multilayer), or f, as a function of Pd coverage on graphene/Ni(111) at 100 K (blue

points) and 300 K (red points). The blue solid line corresponds to the best fit of the low-coverage data at 100 K to a hemispherical cap model, whereby Pd particles grow as hemispherical caps with a constant number density, with best-fit value of 5.5×10^{16} particles/m^2. The red solid line corresponds to the best fit of the low-coverage data at 300 K to a model which assumes the particles are cylindrical disks with constant aspect ratio ($\alpha = 0.22$) and constant number density, with best-fit value of 8.5×10^{15} particles/m^2. The dotted lines are only polynomial fits as a guide to the eye. (b) Average Pd particle thickness vs Pd coverage at 100 K (blue points) and 300 K (red points) calculated from the Pd LEIS data points of panel (a). The blue and red curves correspond to the best-fit models from part (a).

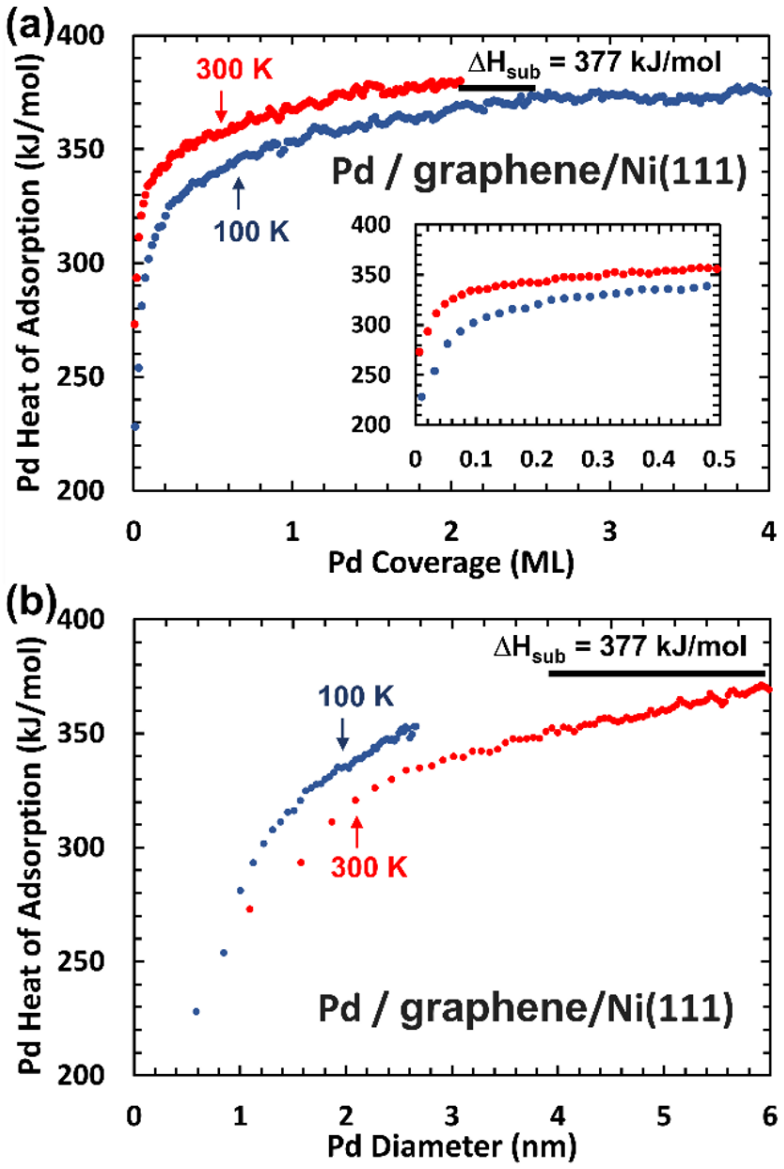

Figure 3.2. Differential heat of adsorption of Pd atoms deposited on single-layer graphene on Ni(111) at 100 K (blue points) and 300 K (red points) as a function of (a) Pd coverage and (b) the average Pd particle diameter from fit in Figure 1(c). The solid black line stands for the sublimation energy. Measurements in (a) taken till 5 ML whereas the heat of adsorption levels off before 4 ML. The inset shows the low-coverage regime (until 0.5 ML) on an expanded scale.

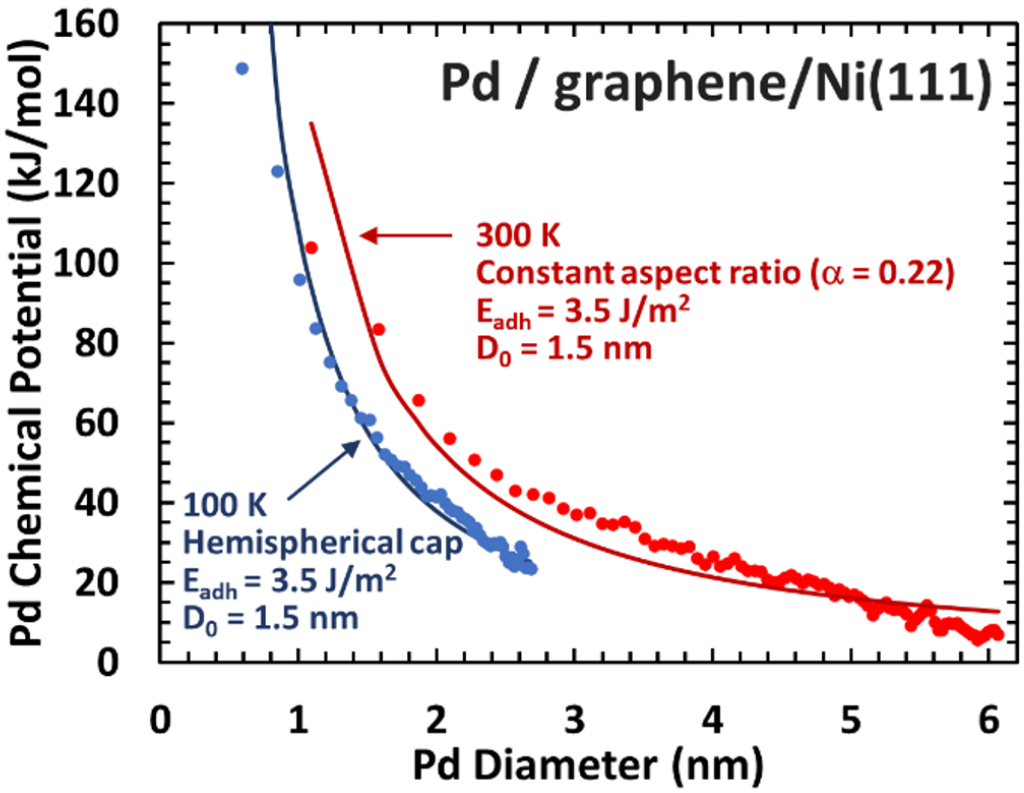

Figure 3.3. Chemical potential of Pd atoms on single-layer graphene on Ni(111) as a function of the average Pd particle diameter during deposition at 100 K (blue points) and 300 K (red points). The blue solid line shows the hemispherical cap approximation applied to the 100 K data with E_{adh} = 3.5 J/m^2. The red solid line shows the best fits of 300 K data to the constant aspect ratio model with also E_{adh} = 3.5 J/m^2.

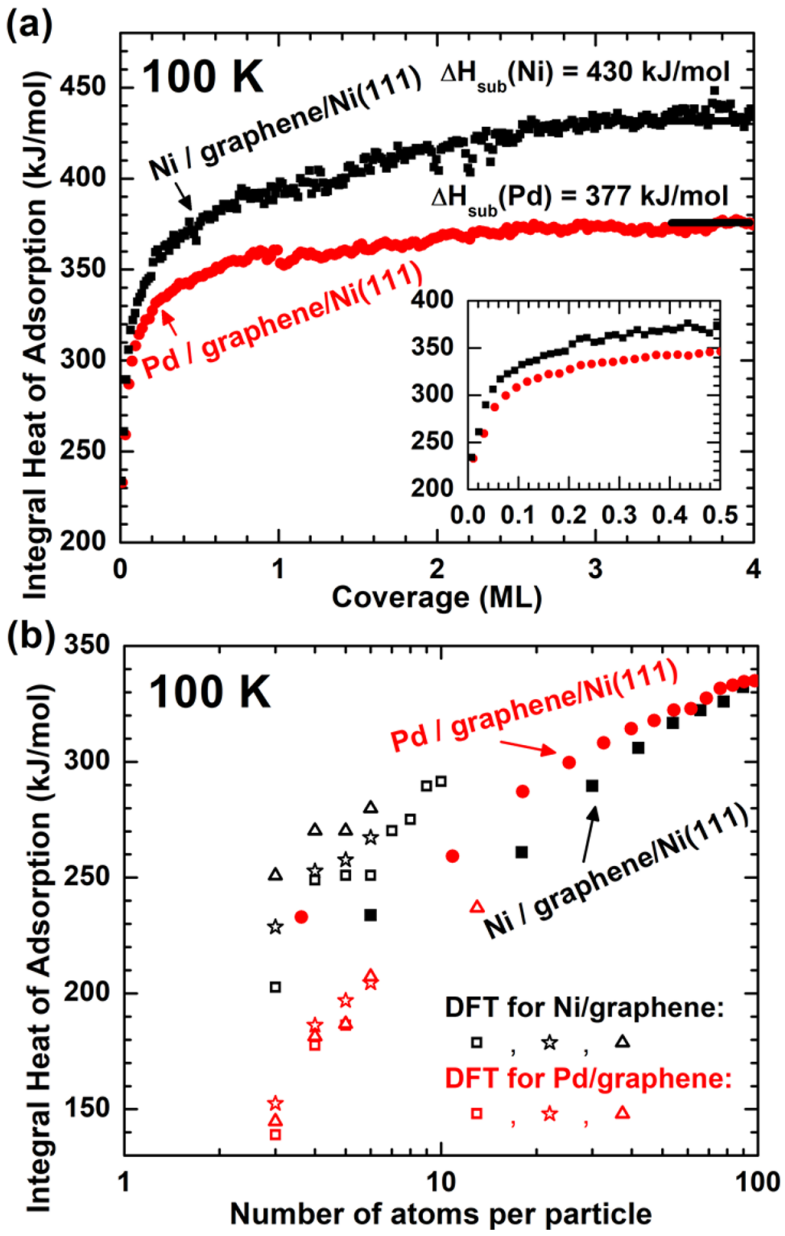

Figure 3.4. (a) Measured integral heats of adsorption of Pd on graphene/Ni(111) (red filled circles) and reported values for Ni on graphene/Ni(111) from ref.[36] as a function of deposited metal coverage. (b) The same heats plotted versus the average number of metal atoms per particle, with comparisons to the DFT calculated energies for metal clusters on free-standing graphene, from the literature: For Pd (in red), squares,[104] stars[106] and triangles;[101] for Ni (in black), squares,[108] stars[106] and triangles.[109]

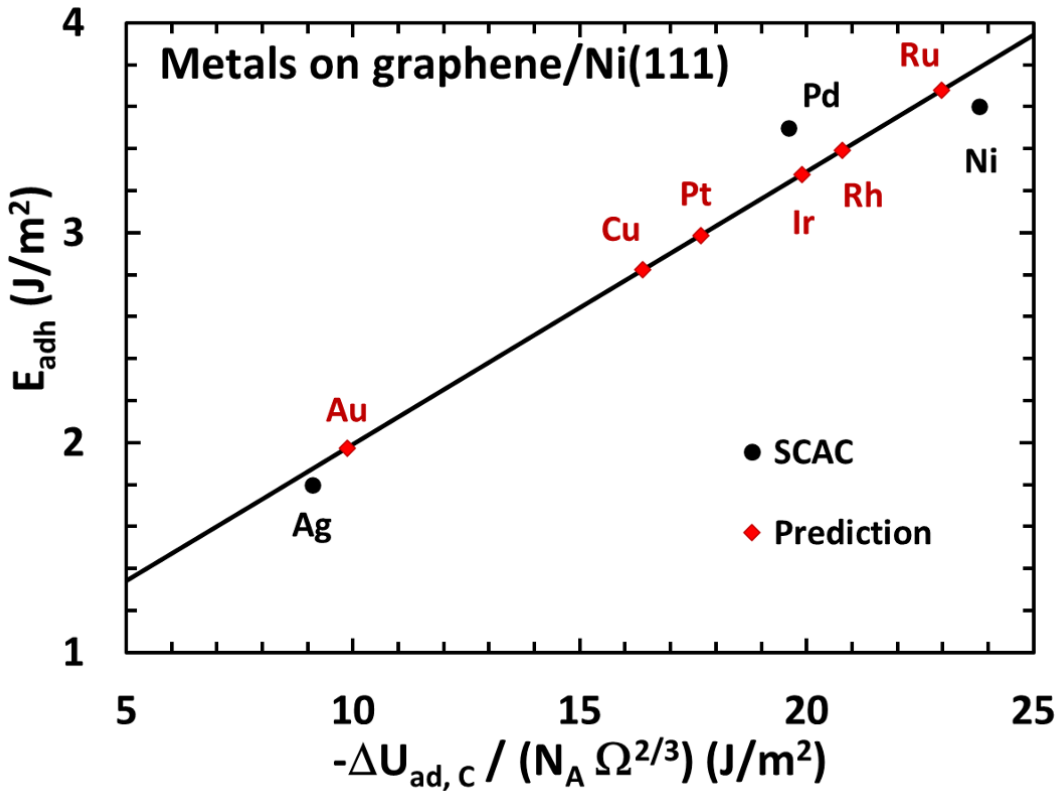

Figure 3.5. Calorimetric E_{adh} values for Ni, Pd and Ag on single-layer graphene on Ni(111) versus carbophilicity per unit area for each metal (M), estimated from $\Delta U_{ad,\,C}$, the DFT-calculated energy for C(g) adsorption on the four-fold step-edge site of the M(211) surface. The best linear fit of the three points of Ni, Pd and Ag gives E_{adh} = 0.130 × carbophilicity/area + 0.69 J/m^2. The values of E_{adh} predicted for other metals from this linear relation are shown as red points.

Chapter 4. Energetics of Cu Adsorption on and Adhesion to Rutile-TiO_2(100) Studied by Cu Vapor Adsorption Calorimetry

This chapter has been published as:

N. Janulaitis, K. Zhao, & C.T. Campbell (2024). *The Journal of Physical Chemistry C*, 128(39), 16481-16490.

Chapter Abstract

The heat of adsorption of Cu vapor versus coverage was measured on rutile-TiO_2(100) at 300 K and 100 K using single-crystal adsorption calorimetry. At these conditions, Cu nanoparticles nucleate and then grow larger. The average Cu particle size versus Cu coverage was measured using He^+ low-energy ion scattering spectroscopy. These data were analyzed with the recently-introduced spherical cap model (SCM) to provide the heat of Cu adsorption and Cu chemical potential versus Cu particle size, as well as the contact angle (67°) and adhesion energy (2.50 J/m^2) at the Cu particle / rutile-TiO_2(100) interface. The hemispherical cap model (HCM) was used to model the data first, and then those HCM results were converted to the more accurate SCM results using a recently-published mathematical approximation whose high accuracy was validated here. The adhesion energy of Cu on rutile-TiO_2(100) measured here is compared to prior values for Ag and Au on rutile-TiO_2(100), showing a nearly proportional increase in adhesion energy with metal oxophilicity (per unit area).

4.1 Introduction

Current environmental, chemical, and energy production technologies often depend on catalysts or electrocatalysts composed of late transition metal nanoparticles distributed on high surface area supports. New catalysts and electrocatalysts of this type are needed for our clean-energy and sustainable-chemistry future. Most such catalyst supports, to which the metal nanoparticles are anchored, are either oxide or carbon-based materials. Thus, there is a huge motivation to correlate and predict the catalytic performance of such metal nanoparticle catalysts based on the details of their structure such as particle size and shape and the nature of the support material's surface, and understanding these relationships has been the subject of intensive research.[114–118]

The chemical potential (energetic instability) of the metal atoms in nanoparticles on a given support correlates with their catalytic performance and sintering resistance.[17–20,37] Metal atoms in larger particles have lower chemical potential (are more stable) because their metal atoms are stabilized by more metal-metal bonds, while those in smaller particles are less stable (higher in chemical potential), and thus generally more chemically reactive.[17–20,37] The metal chemical potential also decreases with the strength of attraction between the metal nanoparticles and the support (or the adhesion energy at that interface), so the adhesion energy controls much of the behavior of the catalytic nanoparticles, including their shape and reactivity.[17–20,37] Sintering, whereby metal nanoparticles grow in size while decreasing in number to lower the system's free energy (by decreasing metal chemical potential) is a common form of catalyst deactivation, and its rate correlates strongly with metal chemical potential. Specifically, activation energy for sintering decreases with increasing metal chemical potential (decreasing particle size) for a given metal/support system.[17–21,37,119]

Copper nanoparticles on TiO_2 supports are promising as catalysts, electrocatalysts, and photocatalysts for a range of reactions.[58,120–125] Copper nanoparticle on other supports are also important in many other reactions.[117,126–133] Because of the ease with which they can be imaged using scanning tunneling microscopy, rutile TiO_2 surfaces are perhaps the most widely studied of all oxide catalyst support materials in terms of atomic-scale surface structure and the connections of that structural detail with surface chemical reactions and their mechanisms. This paper reports measurements of the chemical potential of copper atoms in copper nanoparticles supported on clean rutile-TiO_2(100) surfaces versus Cu particle size. Single crystal adsorption calorimetry (SCAC) is used to measure the adsorption energy of Cu vapor versus Cu coverage, and He^+ low energy ion scattering (LEIS) measurements are used to determine the average Cu particle size versus coverage. The chemical potential of Cu in the nanoparticles is determined from the Cu adsorption energy data. The adhesion energy per unit area at the Cu / rutile-TiO_2(100) interface is determined by fitting the Cu chemical potential versus particle size to a theoretical model.[18,63]

A stronger attraction between the support and a nanoparticle, i.e. a higher metal/support adhesion energy per area, means that nanoparticles of a given size are stabilized to a higher degree by their interaction with the surface, so that their metal atoms have lower chemical potential. The adhesion energy directly relates to the chemical potential of the metal atoms in supported nanoparticles of a given size;[17–19,37,63] therefore, it affects not only the stability and sintering resistance of the nanoparticles but also their shape and reactivity. Tuning the adhesion energy of metal nanoparticles and their supports, by, for example, changing the support material, changes the chemical potential of metal atoms in the nanoparticles, and aids in designing catalysts with optimal activity and stability.[18,134]

Previous work on the interactions between metal nanoparticles and oxide and carbon supports demonstrated linear correlations between the adhesion energy of the metal on a given support and the oxophilicity [18,20,37] (in the case of oxide supports) or carbophilicity [135] (in the case of graphene) of the metal elements. Oxophilicity and carbophilicity indicate how strongly a metal atom binds to oxygen or carbon atoms, respectively. These known proportional relationships for some supports allow prediction of adhesion energies, and thus the metal chemical potential versus particle size, of metals that have not been measured on those supports. Such proportionalities have been measured for CeO_2(111),[18,37,38] MgO(100), [18,37,38] and graphene/Ni(111).[38,135] Titania is used in this study because it is an important catalyst support,[136] for which such an adhesion energy trend would be important. The adhesion energy for Ag on the rutile-TiO_2(100) surface already has been reported.[35] The adhesion energy of Au on the rutile-TiO_2(110) surface has been studied using particle shape measurements.[137,138] The adhesion energy of Cu on rutile-TiO_2(100) is interesting because Cu is much higher in oxophilicity than these previously-studied metals, lying approximately in the center of the oxophilicity range of late transition metals. Thus, it is closer to most other catalytic metals, providing more accuracy when extrapolating any adhesion energy trend that might be discovered.

4.2 Experimental Methods

The rutile-TiO_2(100) surface studied here was grown on a clean Mo(110) single crystal surface in an ultra-high vacuum (UHV) chamber with a background pressure of 1×10^{-10} torr. Growth of this oxide face on the Mo(110) substrate has been previously described in literature and has also been previously implemented by the Campbell group.[35] The clean Mo(110) surface was heated to ~350ºC and simultaneously exposed to 2×10^{-7} torr of O_2 and a flux of titanium

vapor. The Ti was evaporated from a titanium-wire-wrapped W filament that was resistively heated. The time of growth was adjusted so that the thickness of the resulting TiO_2 film was 2 to 4 nm. According to our prior studies of metal adsorption energetics on oxides,[28] oxide films that are only 1 nm thick showed higher heats of metal adsorption than films that were 2, 3 and 4 nm thick, which all had the same heats and therefore are assumed to be bulk-like is material character. The thickness of the TiO_2 film was estimated using the attenuation of the Mo $3d_{5/2}$ peak in x-ray photoelectron spectroscopy (XPS), compared to the peak on a clean Mo(110) surface. The shift and lineshape of the Ti $2p_{3/2}$ XPS peak were also measured to confirm that the Ti film was fully oxidized and had minimal oxygen vacancies. XPS was also used routinely to verify surface cleanliness. The (100) structure of the TiO_2 film was verified by low energy electron diffraction (LEED) as described in ref.[35]

The heat of Cu adsorption was measured by single crystal adsorption calorimetry (SCAC), which has been previously described in detail.[64] Briefly, a polyvinylidene difluoride (PVDF) ribbon, which is pyroelectric, is pressed against the back of the Mo single-crystal sample to detect heat changes on the sample surface. A flux of metal atoms is generated using an electron beam evaporator. An off-axis quartz crystal microbalance (QCM) continuously monitors Cu flux near the evaporator during calorimetry measurements. An on-axis QCM is translated just in front of the single crystal sample before and after metal deposition (e.g., for Cu adsorption calorimetry or LEIS studies) to monitor the flux of Cu at the sample. The ratio of metal fluxes measured at the sample and near the evaporator (off-axis) are used to scale the off-axis QCM reading to determine the Cu flux on the sample during Cu deposition. The flux of Cu atoms is cut into pulses using a rotating chopper, and, as these pulses of metal atoms are deposited on the surface, the PVDF ribbon gives an electric response to the heat changes on the sample. The

electric response of the ribbon to heat changes is calibrated for every experiment by measuring the ribbon response when a HeNe laser of known power is pulsed onto the sample. The hot metal source generates optical radiation that also heats the sample slightly. This contribution to the heat at the sample is measured separately by positioning a translucent BaF_2 window in front of the sample surface. After correcting for the small fraction of light that is absorbed by this window, this optical heat is subtracted from the total heat. A quadrupole mass spectrometer (QMS) measures the fraction of metal atoms that do not stick to the surface, and a sticking probability is calculated from this measurement, as referenced to a zero-sticking probability measurement taken by pulsing metal onto a hot tantalum flag. If the sticking probability is not unity, the modified King and Well's method[67] is used to correct for non-sticking metal atoms. The heats are also corrected for the small difference in internal energy (which is all translational energy here) between a flux of gaseous Cu atoms initiating from a high-temperature electron beam evaporator and a collection of the same gas atoms in an equilibrated volume at the support surface temperature.[27,100] Due to errors (up to ~3.5%) in calibrating the calorimeter's absolute heat signal with laser pulses, this calibration factor is slightly adjusted to ensure that the heat of adsorption and corresponding Cu chemical potential agree with the theoretical model for chemical potential versus particle size at the largest particle sizes analyzed (see below).[60] The final "heat of Cu adsorption" values reported here, including the above corrections, are the negative of the standard enthalpies of Cu adsorption at the surface temperature.

For growth morphology measurements, metal is deposited on the sample in small amounts (typically <1 ML) and the sample is analyzed with He^+ LEIS after each deposition. The incident energy of the He^+ ions is 1 keV and their scattering angle is 135º. Before and after each deposition of metal onto the sample surface, the Cu flux at the sample is measured using the on-

axis QCM in the main chamber. The off-axis QCM continuously monitors and records the flux near the evaporator. After each deposition, a He^+ LEIS spectrum is recorded for both the substrate and the deposited metal. The signals are normalized using the signals from the clean substrate and the substrate when it is covered in a multilayer (~40 ML) of the deposited metal. After small corrections for shadowing effects,[60] the Cu LEIS signal at any coverage, normalized to that for a continuous Cu multilayer film, provides a measure of the fraction of the TiO_2 surface covered by Cu nanoparticles. Dividing the area-averaged Cu thickness (which is one way to express the total Cu coverage) by this area fraction gives the average thickness of the Cu particles. Within the spherical cap model (SCM) for particle shape,[60] for any given contact angle at the particle/support interface, this average particle thickness also corresponds to a specific particle size (footprint diameter).

4.3 Results

4.3.1. Cu Sticking Probability on Rutile-TiO_2(100)

The sticking probability of Cu vapor onto rutile-TiO_2(100) was measured with the QMS signal and normalized to the zero-sticking QMS signal from a hot tantalum flag (see Experimental). The sticking probabilities of Cu on rutile-TiO_2(100) at 300 K and 100 K are shown in Figure 4.1 as a function of Cu coverage.

Reported Cu coverages are given here in monolayers (ML), where one ML is 7.36×10^{18} atoms/m^2, the areal number density of coordinatively-unsaturated O atoms on an ideal bulk-terminated rutile-TiO_2(100) surface (i.e., O2C atoms). Points from multiple experimental runs are included for each temperature. Because the sticking probabilities are used to determine

coverages and convert heat measurements to "per mole adsorbed" units, each set of data is fitted to a simple function to remove noise,

$$S = 1 - C \exp(-X/X_0), \quad (4.1)$$

where S is the sticking probability, X is the coverage, and C and X_0 are fitting parameters. These sticking probability functions are multiplied by the measured Cu flux to obtain the increase in Cu coverage with each gas pulse, and applied to the measured heats of adsorption at 300 K and 100 K to convert them to a heat per mole of adsorbed Cu. The sticking probability at both temperatures is very close to unity. At 300 K, the sticking probability is nearly constant within the measured coverage range, with an average sticking probability of 99.8%. At 100 K, the initial sticking probability is approximately 98%, and increases to 99.8% by 4 ML. For later transition metals on oxides, the initial sticking probability has rarely, if ever, been reported to be lower at 100 K than 300 K.[139–141] The coverage of some weakly-adsorbed background-gas contaminants, such as CO or H_2O, on the rutile-TiO_2(100) surface is likely higher at the lower temperature. These contaminants, if at low level such as 2% of a ML at 100 K, could prevent about 2% of the incoming Cu atoms from sticking to the surface as observed, due to simple site blocking. At 300 K, when these contaminants are expected to have a much lower coverage than at 100 K, far fewer sites are blocked, so Cu atoms have higher sticking probability, much closer to unity. This suggests that the sticking probability of Cu on a truly *clean* TiO_2(100) surface is approximately unity at both temperatures. The observed increase in S toward unity with increasing Cu coverage is expected, since S is known to be unity for Cu on multilayer Cu surfaces at 100 to 300 K.[142,143]

4.3.2 Cu Growth Morphology on Rutile-TiO_2(100)

He^+ LEIS measurements were used to determine the growth morphology of Cu nanoparticles on rutile-TiO_2(100), using methods that have been previously described in detail.[60,61] Cu is deposited incrementally onto the sample surface, and, after each increment, the Cu LEIS signal is measured. The amount of Cu deposited in every increment is calculated from the sticking probabilities in Figure 4.1 times the Cu flux and dose time. The Cu LEIS signal is integrated and normalized to the integrated Cu signal of a thick Cu multilayer. The resulting value gives the fraction of the oxide surface covered and shadowed by Cu. Shadowing effects in LEIS are accounted for using a growth model that assumes particle shape (hemispherical cap or spherical cap).[60,61]

The normalized Cu He^+ LEIS signal intensities as a function of Cu coverage at 300 K and 100 K are shown in Figure 4.2. Datasets at each temperature are a compilation of measurements from multiple experimental runs. The best fits of the data to the hemispherical cap model (HCM), which assumes the Cu nanoparticles grow as hemispherical caps of the same size at any given coverage and with a constant number density independent of coverage,[61] are also shown. The data points at Cu coverages where > 30% of the surface is covered (normalized Cu signal intensity > 0.30) are excluded from each of the fits because the nanoparticles (or their shadows) may begin to overlap, which is not accounted for in mathematical growth mode models used here.[60,61]

The number density of particles is determined from the best fit of the data to the model. The HCM fits both the 300 K and 100 K data well and gives a number density of 1.5×10^{17} particles/m^2 at 300 K and 2.4×10^{17} particles/m^2 at 100 K. The HCM gives a good first estimate

of the growth morphology of the Cu nanoparticles, but a more descriptive model with fewer assumptions, called the spherical cap model (SCM),[60] has recently been developed. The SCM assumes that the particles grow as spherical caps (of the same size at any given coverage and with a fixed number density and contact angle, independent of coverage). The contact angle between the nanoparticles and the substrate is initially assumed to be 90°. The SCM with this assumed contact angle of 90° is equivalent to the HCM. Details of fitting such LEIS data to the SCM were presented by Zhao et al.[60] The best fit of the SCM for any assumed contact angle gives exactly the same line as the HCM best-fit line shown in Figure 2, but requires a different number density of particles to get the best fit. The best fit of the SCM with an assumed contact angle of 67° to the LEIS data is exactly the same line as the HCM best-fit line shown in Figure 4.2 for either temperature, except with nanoparticle number densities of 7.4×10^{16} particles/m^2 at 300 K and 1.2×10^{17} particles/m^2 at 100 K. (These were calculated from the HCM values using Equation 4.7 below.) As described below, this contact angle of 67° is preferred over the HCM because it gives an adhesion energy from the fit to calorimetric metal chemical potential versus size that agrees with the Young-Dupré equation, following a procedure described previously.[63]

The number density is higher at 100 K because the Cu adatoms have a smaller diffusion constant on rutile-TiO_2(100) at 100 K than at 300 K, due to the activation energy for diffusion. The lower diffusion constant, means that, at the same coverage, the Cu atoms form more and smaller islands at 100 K than at 300 K.[96] The best-fit number density at 100 K is ~1.6-fold higher than at 300 K. Using Venables homogeneous nucleation model[96] relating the particle number density to the metal monomer diffusion constant (to the -1/3 power), these number densities indicate that the diffusion constant for Cu adatoms across the surface is ~4 times larger at 300 K

than at 100 K (k_{diff}(300 K) / k_{diff}(100 K) = 1.6[3]). From this ratio, the activation energy for Cu adatom diffusion across rutile-TiO_2(100) can then be estimated to be ~1.8 kJ/mol. ($E_{diff} = R \times \ln(4)/[(1/100\ K) - (1/300\ K)] = 1.8$ kJ/ mol.)

4.3.3 Heat of Adsorption of Cu on Rutile-TiO_2(100)

The differential heats of Cu vapor adsorption on rutile-TiO_2(100) were measured with SCAC, as shown in Figures 4.3 and 4.4. These have been corrected for optical radiation, temperature, and translational energy effects, as described in the Experimental section, so that these reported heat values equal the negative standard enthalpies of adsorption of Cu gas atoms on the rutile-TiO_2 surface at the sample temperature. We found that the heat of Cu adsorption versus Cu coverage was always very high in the first 2% of a ML, quickly decreased to a minimum at 10-15% of a ML, and then rose with coverage, eventually approaching an asymptotic value near the bulk heat of Cu sublimation ($\Delta H_{sub,\ Cu}$ = 337 kJ/mol).[144] This behavior is often reported for late transition metal adsorption on single-crystal oxide surfaces, and has been interpreted to indicate that the surface has a few percent of stronger-binding defects (probably mainly step edges), which get saturated after a few % of a ML, and thereafter the heats are dominated by metal binding to metal particles, whose growing interface with the oxide is mainly at normal terrace sites.[35,98,112] This high initial heat varies by up to 60 kJ/mol from run to run, which we attribute to run-to-run variations in the areal density of defects. Figure 4.3 shows the heat of adsorption at 300 K as a function of Cu coverage, averaged over several runs when the rutile-TiO_2(100) surface appeared to have many defects (based on their higher initial heats) and averaged over runs when the number of surface defects appeared to be far fewer (lower initial heats).

The average initial heat of Cu adsorption is about 40 kJ/mol higher for the rutile-TiO_2(100) surfaces with many defects than for the surfaces with minimal defects at the same temperature. Once the defects have been saturated, the adsorption energies for both surfaces nearly equal each other (above about 0.5 ML). The initial higher heat due to defects is seen even for the surfaces with minimal defects, so they are not defect-free. If the surface were ideal, the initial heat of adsorption would be expected to be the lowest, and progressively increase with coverage due to increasing particle size (see below). When there are fewer defects, the heats are initially lower, and the minimum heat is located at a lower coverage, so the heat of adsorption curve is more indicative of that on an ideal rutile-TiO_2(100) surface. For the remainder of this work, we only present and analyze data from experiments on rutile-TiO_2(100) surfaces of the type shown here with "low defect density".

The subsequent increase in Cu heat with coverage in Figure 4.3 is always seen for late transition metal adsorption on single-crystal oxide surfaces (of the oxide types used for catalyst particle support materials), even when such defect sites are not evident. This increase is well known to be associated with the fact that the metal nanoparticle size increases with coverage, so that the average number of metal-metal bonds formed when one new metal atom adsorbs increases with particle size.[19,145]

The differential heats of Cu adsorption at 300 K and 100 K as a function of Cu coverage, averaged over several runs, are shown in Figure 4.4. The heats are scaled (relative to absolute heat calibration) so that the multilayer heat of adsorption approaches the heat of sublimation of Cu.

The initial heat of adsorption of Cu at 100 K is larger than at 300 K. As described above, defects on the surface can cause the initial heats to be larger than would be observed on an ideal

surface, but, because the surfaces used for the 100 K experiments were prepared in the same way as at 300 K, we do not expect them to have a significant difference in defect density. Furthermore, at 100 K, the Cu atoms are less likely to reach defect sites because they are less mobile, as described above, so, although defects may play a role, the initial heats are likely higher at 100 K for a different reason. At 100 K, the surface is likely to have more adsorbed impurities from background gases in the UHV chamber. The observed sticking probability data (above) indeed suggests that adsorbed impurities are present on the oxide surface at 100 K at the ~2% of a ML level, but are not significant at 300 K. These impurities (such as CO and H_2O) probably adsorb more strongly to the Cu adatoms and clusters, so they likely move to the Cu sites upon Cu adsorption, which would release the additional heat seen in the 100 K data versus 300 K. At 100 K, this impurity effect is possibly the most significant contributor to the initially elevated heats of adsorption; whereas, at 300 K, surface defect sites are the main effect (since neither CO nor H_2O should have significant coverages on TiO_2 surfaces at 300 K.)

The defect sites and/or impurities have been saturated with Cu for both temperatures by ~0.4 ML, at which point the heats of adsorption at 100 K are lower than at 300 K, and this holds true until about 2 ML is reached. Recalling that the number density of Cu nanoparticles at 100 K is about 1.6 times larger than at 300 K (see above), the particles at any given Cu coverage are about 1.6 times smaller in volume at 100 K, so the Cu atoms have, on average, a lower coordination number, resulting in a lower heat of adsorption. As more Cu atoms are deposited, the average coordination number of the Cu atoms increases, because the incoming Cu atoms form more metal-metal bonds. As Cu coverage increases, the number of new Cu-Cu bonds formed upon Cu adsorption approaches six (1/2 the bulk coordination number of 12), and the heat of adsorption approaches $\Delta H_{sub,\,Cu}$. This is why the heats of adsorption increase as a function

of Cu coverage (once defects and impurities are no longer a contributing factor) at both 300 K and 100 K, but do so more slowly at 100 K. In the range of 0.5 to 1 ML, the same heat is obtained at 100 K as at 300 K only when the Cu coverage is about 60% higher at 100 K. Since the number density of particles is about 60% higher at 100 K than 300 K (see above), this means that the heats at 100 K and 300 K are nearly the same at the same particle volume in this coverage range.

Based on a thermodynamic analysis that reproduces well the trends for metal adsorption on oxide surfaces,[95] the adsorption of Cu is not likely to be accompanied by any significant extent of reduction of the TiO_2 to make any Cu oxide: The heat of formation of bulk Cu oxide is much smaller that the heat of reduction of 2 TiO_2 to Ti_2O_3 (368 kJ/mol O).[95]

4.3.4 Chemical Potential and Adhesion Energy of Cu on Rutile-TiO_2(100)

The chemical potential of Cu on rutile-TiO_2(100) at any Cu coverage (particle size) relative to the zero reference for chemical potential (bulk solid Cu of infinite size) is estimated to equal the difference between the heat of Cu adsorption and $\Delta H_{sub,\,Cu}$, as we have done previously.[17,20,37] This neglects molar entropy changes with Cu coverage (particle size), which are assumed to be negligible relative to the large enthalpic changes versus coverage (size) reported here. The average size of the Cu nanoparticles at any Cu coverage is calculated from the coverage (Cu atoms per unit area) divided by the number density of Cu particles (particles per unit area). To convert the number of Cu atoms per particle to volume per particle, we assume the particles have the same mass density as bulk Cu(solid). The number density of Cu particles is determined from the best fit of the LEIS data to the SCM (Figure 4.2). Initially, we will assume the HCM for this fitting, but modify it later to give the best fit to the SCM model. (As described

previously,[63] this is the simplest way to solve the mathematics of the SCM fitting.) These models' assumptions only hold below a coverage where nanoparticles (or their LEIS "shadows") start to overlap, as described above. The resulting chemical potential of Cu plotted as a function of Cu particle effective diameter (D, for the HCM), within this coverage range, is shown in Figure 4.5 for both 100 K and 300 K, as obtained from the data in Figures 4.3 and 4.4.

The chemical potential of the metal atoms, μ_{HCM}, in hemispherical cap nanoparticles attached to a flat surface has been shown to be well-modeled as a function of particle diameter, D, by:[17,18]

$$\mu_{HCM}(D) = (3\gamma_M - E_{adh})\left(1 + \frac{D_0}{D}\right)\left(\frac{2V_M}{D}\right), \quad (4.2)$$

where γ_M is the surface energy of the bulk metal (1.8 J/m^2 for Cu),[20,146] V_M is the molar volume of the bulk metal (7.12 cm^3/mol for Cu), E_{adh} is the adhesion energy per unit area between the metal particle and the surface (in the large-size limit), and $(1 + D_0/D)$ with $D_0 = 1.5$ nm is an empirical factor that accounts for the fact that γ_m and E_{adh} of metal particles both increase with decreasing D below 10 nm, but are treated in this equation as constant values (at their large-size limits).[17]

The best fit of the data to Equation 4.2 is shown as the solid line in Figure 4.5. The data points for particles with D < ~0.9 nm are neglected from the best fit due to the effects of defects and/or impurities, so that the resulting E_{adh} value should reflect the value for clean rutile-TiO_2(100) terraces. The 100 K data are also excluded from the fitting because the particle size range is narrow, but Figure 4.5 shows that the 100 K data agrees excellently with the model for the chemical potential that is fit based on the 300 K data alone.

The values reported above are based upon the HCM, but these values may be corrected to the more accurate SCM by using the results of the HCM, as described elsewhere.[60,63] This purely

mathematical shortcut alleviates the need for some complex data analyses that involve:[60] first finding the best fit to the LEIS data assuming a wide range of contact angles at every 1°, and then fitting the calorimetric heats to the SCM chemical potential model for each assumed contact angle, to finally finding the one assumed contact angle that gives an adhesion energy consistent with the Young-Dupré equation below (Eq. 4.5).

Within the SCM, the chemical potential, μ_{SCM}, as a function of the spherical cap footprint radius, r, is given by:[63]

$$\mu_{SCM}(r) = \left\{[2\alpha(\theta_c) + 1]\,\gamma_M - E_{adh,SCM}\right\}\frac{2}{\alpha(\theta_c)\,\beta(\theta_c)}\left(1 + \frac{D_0 \sin(\theta_c)}{2r}\right)\left(\frac{V_M}{r}\right), \quad (4.3)$$

where $\alpha(\theta_c)$ and $\beta(\theta_c)$ are simply-defined functions of the contact angle, θ_c, at the nanoparticle / support interface: $\alpha(\theta_c) = 1/[1 + \cos(\theta_c)]$ and $\beta(\theta_c) = [(2 + \cos(\theta_c)(1 - \cos(\theta_c)]/[\sin(\theta_c)]$.[60] The adhesion energy when particles are modeled as spherical caps, $E_{adh,SCM}$, can be estimated from the HCM model's best-fit adhesion energy, $E_{adh,HCM}$ (in this case, 3.57 J/m^2 for Cu / rutile-TiO_2(100) from Figure 4.5) as:[38]

$$E_{adh,SCM} = E_{adh,HCM}\left[1 - 0.300\left(E_{adh,HCM}/\gamma_M - 1\right)^{0.543}\right]. \quad (4.4)$$

The resulting adhesion energy of Cu / rutile-TiO_2(100) using the SCM is 2.50 J/m^2. This $E_{adh,SCM}$ can then be used to calculate the contact angle of the nanoparticles with the Young-Dupré equation:[62]

$$E_{adh,SCM} = \gamma_M(1 + \cos(\theta_c)). \quad (4.5)$$

The resulting contact angle of spherical Cu caps on rutile-TiO_2(100) is 67°. $E_{adh,SCM}$ and θ_c may then be used in Equation 3 to model the chemical potential in the context of the spherical cap model. This best fit of the SCM to the Cu chemical potential as a function of spherical-cap footprint diameter is shown as the solid curve in Figure 4.6. (The scaling factor applied to the

calorimetric heat calibration in Figure 4.6 is 1% larger than the factor used to scale the heat data for the HCM fit in Figure 4.5, as required to provide the best agreement in the large-size limit to each model's predictions of chemical potentials, since these have slightly different large-size functional forms.) The particle size on the x-axis of Figure 4.6 is the footprint diameter of the spherical cap nanoparticle at the support interface (2r), not the diameter of the sphere upon which its radius of curvature is defined (2R).

The particle size at any given coverage in the SCM differs from that of the HCM. The difference in particle size also changes the (constant) particle density. The relationships between HCM particle size and SCM particle size, and HCM particle density and SCM particle density, were derived previously, and are given by:[60,63]

$$\frac{r(\theta_c)}{r(90°)} = \frac{X_M^{\cap}(\theta_c, \theta_d)}{X_M^{\cap}(90°, \theta_d)} \frac{\alpha(90°)\beta(90°)}{\alpha(\theta_c)\beta(\theta_c)} \tag{4.6}$$

$$\frac{n_{np}(\theta_c)}{n_{np}(90°)} = \left[\frac{X_M^{\cap}(90°, \theta_d)}{X_M^{\cap}(\theta_c, \theta_d)}\right]^3 \left[\frac{\alpha(\theta_c)\beta(\theta_c)}{\alpha(90°)\beta(90°)}\right]^2. \tag{4.7}$$

Here, $X_M^{\cap}$ is a well-defined function of θ_c and θ_d, given in ref. [60], where θ_d is the angle from support surface's normal to the ion detector. The SCM fit determined using the method above provides an excellent fit to the calorimetric chemical potential data. This confirms that the best fit to the HCM, which has been fit to only one parameter (adhesion energy), can be used to calculate the two best-fit SCM parameters (adhesion energy and contact angle), without the need to do the mathematically-complex full fit to the SCM. This was claimed previously,[38] and this result confirms the validity of that claim.

4.4. Discussion

A previous MEIS study[147] of Cu on rutile-TiO_2(110) found that, below coverages of about 0.5 ML, Cu islands grow as hemispherical caps, and then proceed to grow as spherical caps. If the (100) surface behaves similarly to the (110) surface, then these results are generally consistent with the observations reported here. STM studies of Cu on rutile-TiO_2(110) report that metal atoms favor step edges,[148,149] and this is likely also true for the (100) face. At 300 K, Cu adatoms diffuse faster and can reach the preferred step-edge sites. At 100 K, Cu nanoparticles are more likely to form on terrace sites, as well as step-edge sites, because the metal atoms have less mobility to reach step-edge sites. The larger number density of the Cu nanoparticles is consistent with more nanoparticles forming on terrace sites at 100 K, because incident Cu atoms are more likely to nucleate new particles before reaching an existing cluster or a step edge.

The growth morphology of vapor-deposited Ag on the rutile-TiO_2(100) surface has been previously studied.[35] Using the HCM, the study found that the Ag nanoparticle number density on rutile-TiO_2(100) is 8.0×10^{16} particles/m^2 at 300 K and 2.5×10^{17} particles/m^2 at 100 K.[35] The Ag nanoparticle densities found by the HCM approximation but later corrected by the SCM, using Equation 4.7 above, are 4.3×10^{16} particles/m^2 at 300 K and 1.4×10^{17} particles/m^2 at 100 K.[63] Using the method noted above, this allows us to estimate the diffusion activation energy for Ag adatoms on rutile-TiO_2(100) to be 4.4 kJ/mol. This is larger than the 1.8 kJ/mol value estimated above for Cu on this same surface. Because the heats of adsorption for Cu are larger than for Ag, the expected trend is that the diffusion barrier will be higher for Cu than Ag adatoms.[96,150,151] On the other hand, the density of Cu nanoparticles is about 2 times larger than that of Ag nanoparticles on rutile-TiO_2(100) at 300 K, consistent with the higher heats of adsorption for Cu than Ag and the corresponding expectation that the diffusion barrier will be

higher for Cu than Ag adatoms. The diffusion barrier estimated from nanoparticle densities for Cu here may be biased by the obvious involvement of defects and impurities in the heats at 100 K in the low-coverage range of Figure 4.4, when nucleation is occurring.

This higher nanoparticle density for Cu than Ag on rutile-TiO_2(100) is also consistent with the nanoparticle densities reported for Cu / CeO_2(111) [34] and Ag / CeO_2(111),[28] where the Cu particle density is also about 2 times higher than that of Ag at 300 K (7.8×10^{16} particles/m^2 for Cu / CeO_2(111); 4×10^{16} particles/m^2 for Ag on CeO_2(111)), and where the heats of adsorption for Cu are also higher than for Ag. These nanoparticle densities for Cu and Ag on CeO_2(111) are even similar in magnitude to the corresponding values on rutile-TiO_2(100), which suggests that the two oxide surfaces have similar interaction strengths with Cu and Ag. To our knowledge, nanoparticle densities for Cu an Ag on CeO_2(111) at 100 K have not yet been reported, so we cannot make the same comparison at a low temperature.

The adhesion energy of the nanoparticles on the flat support surface is determined from the He^+ LEIS growth morphology results (Figure 4.2) and the chemical potential of the nanoparticles versus size (Figures 4.5 and 4.6), which is obtained from the heats of adsorption (Figure 4.4). The chemical potential versus size (below the large-particle size limit where overlapping LEIS shadows do not occur) is used to determine the adhesion energy. The adhesion energy of Cu to rutile-TiO_2(100), extracted from the best fit of the HCM model (Equation 4.2) to the chemical potential, is 3.57 J/m^2. Applying the more accurate SCM to this Cu / rutile-TiO_2(100) result lowers the adhesion energy to 2.50 J/m^2, which is our best estimate of the true value. Note that in this SCM model, this adhesion energy corresponds, by definition, to the large Cu particle size limit for the Cu / rutile-TiO_2(100) interface. (The empirical correction factors involving D_0 in Equations (2) and (3) accounts for the increase in both adhesion energy and

metal surface energy with decreasing particle size.) This is a relatively large adhesion energy, reflecting that Cu nanoparticles on this support are relatively stable (low chemical potential for a given size). This also means that they should also be relatively resistant to sintering.[19,119]

The adhesion energy of Ag to the rutile-TiO_2(100) surface, measured with the same methods used here and fitted using the HCM, was reported to be 2.44 J/m^2.[35] This HCM adhesion energy for Ag / rutile-TiO_2(100) was later corrected using the more accurate SCM model following the above procedure to give 1.64 J/m^2.[63]

Adhesion energy trends on other oxide surfaces have shown that the adhesion energy for metals on a given oxide surface are nearly proportional to the oxophilicity per unit area of the metal.[18,37,38] Oxophilicity, a measure of how strongly one metal atom binds O atoms, is defined as the difference between the sublimation enthalpy of the metal and the formation enthalpy of the most stable metal oxide of the metal per mole of metal atoms. Oxophilicity per unit area (or "Oxo" for short) refers to this oxophilicity (in kJ/mol) divided by the area per mole of metal atoms (estimated as the atomic volume in the bulk metal to the 2/3 power times Avogadro's number). This area per mole varies little from one late transition metal element to another, so that Oxo variations are dominated by oxophilicity differences. The proportionality of E_{adh} with Oxo (~oxophilicity) indicates that the adhesion interaction between a metal particle and an oxide is mainly governed by bonds between the metal atoms and the surface oxygen atoms.

The oxophilicities per unit area of Cu and Ag are 15.9 J/m^2 and 7.5 J/m^2, respectively.[18,38] Both the oxophilicity and adhesion energy of Cu are larger than those of Ag, which agrees with the general trend of metals with larger oxophilicities also having larger adhesion energies to the same oxide surface. The growth morphology results above suggest that rutile-TiO_2(100) and CeO_2(111) have similar interaction strengths, and the adhesion energy of Cu to CeO_2(111) is

2.60 J/m^2 (from the SCM),[63] which is very similar to the value of 2.50 J/m^2 reported here for Cu / rutile-TiO_2(100), supports this observation. This result is also consistent with what is expected from the growth morphology results, which are similar for Cu / CeO_2(111) and Cu / rutile-TiO_2(100). This similarity also agrees well with the observation that the adhesion energy of Ag / CeO_2(111) is 1.70 J/m^2,[63] which nearly matches the adhesion of Ag to rutile-TiO_2(100).

DFT studies[152,153] have found that both Cu and Ag tend to have strong interactions with the rutile-TiO_2(110) surface, with Cu being the stronger of the two. Based on the results reported here, the (100) surface also has strong interactions with Cu, much stronger than the interactions between Ag and this surface. These same theoretical studies, as well as experimental studies,[137,138] found that the interaction strength between Au and rutile-TiO_2(110) is much weaker than for Ag or Cu. Because Au has a slightly higher oxophilicity than Ag, and because the adhesion energy of Au to CeO_2(111) is also slightly higher than Ag to CeO_2(111), we would expect the adhesion energy of Au / rutile-TiO_2(100) to be similar in magnitude to that of Ag / rutile-TiO_2(100). Further studies are needed to clarify whether differences between the (100) and (110) faces might cause this deviation from demonstrated trends. In general, the results reported here suggest that adhesion energies to rutile-TiO_2(100) generally follow the trend reported for metals on CeO_2(111).[38]

4.5 Conclusion

The adsorption of Cu vapor on rutile-TiO2(100) was found to nucleate and grow 3D Cu nanoparticle with saturation densities of 7.4×10^{16} and 1.2×10^{17} particles/m^2 at 300 K and 100 K, respectively. The heats of adsorption of Cu vapor on rutile-TiO_2(100) were measured using SCAC. Defects and potential contaminants (at 100 K) on the grown rutile-TiO_2(100) surface

cause the initial heats of adsorption to be elevated compared to the values on a clean, ideal rutile-TiO_2(100) surface. Once defect and contaminant effects no longer dominate, the heats of adsorption at the same coverage were higher at 300 K than at 100 K, because at 300 K the metal grows fewer but larger nanoparticles. This is attributed to the monomers' higher diffusion constant than at 100 K. The differential heats of Cu adsorption were used to determine the Cu atom chemical potential versus coverage. After the initial effects of defects and contaminants at very low Cu coverage, the chemical potential was the same for Cu particles of the same size at 100 K and 300 K. These Cu nanoparticle densities and sizes versus coverage, and the adhesion energy at the Cu / TiO_2(100) interface, were determined by simultaneously modeling the Cu He^+ LEIS signal and chemical potential versus coverage using the recently-developed spherical cap model (SCM, which has the same assumptions as the often-used hemispherical cap model (HCM) except allowing other contact angles besides 90°), and assuming that the particles have their equilibrium contact angle (so that the Young-Dupré equation relates contact angle to adhesion energy). The adhesion energy at the Cu / rutile-TiO_2(100) interface was found to be 2.50 J/m^2, with a contact angle of 67°. A previously-proposed mathematical shortcut was used to do this simultaneous fitting, whereby the data are first analyzed within the HCM approximation to determine the adhesion energy within the HCM, and this is corrected to the more accurate SCM value using Equation (4).[38] This avoids the more complex and time-intensive mathematical analyses otherwise required to model the data using the SCM. The presented results confirm the accuracy of the approximation inherent to Equation (4). The adhesion energy of Cu / rutile-TiO_2(100) is larger than reported for Ag / rutile-TiO_2(100) (1.70 J/m^2), showing that the adhesion energy increases nearly proportional to the metal's oxophilicity per unit area, consistent with the trends observed for CeO_2(111) and MgO(100).

4.6 Figures

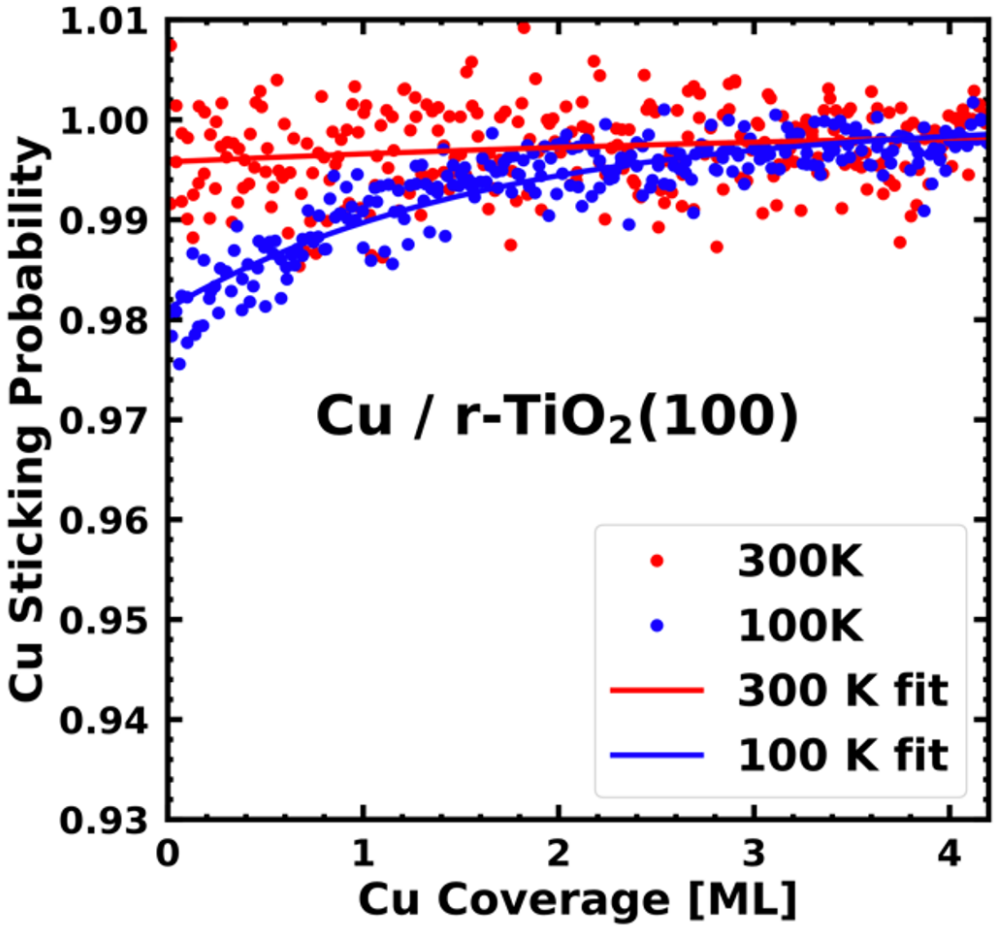

Figure 4.1. Sticking probability of Cu on rutile-TiO_2(100) at 300 K (red) and 100 K (blue). The data for each temperature includes multiple experimental runs. The lines are the best fits for each temperature to the simple function $S = 1 - C\ exp\ (-X/X_0)$, (300 K: C = 0.0042, X_0 = 4.8; 100 K: C = 0.019, X_0 = 1.6)

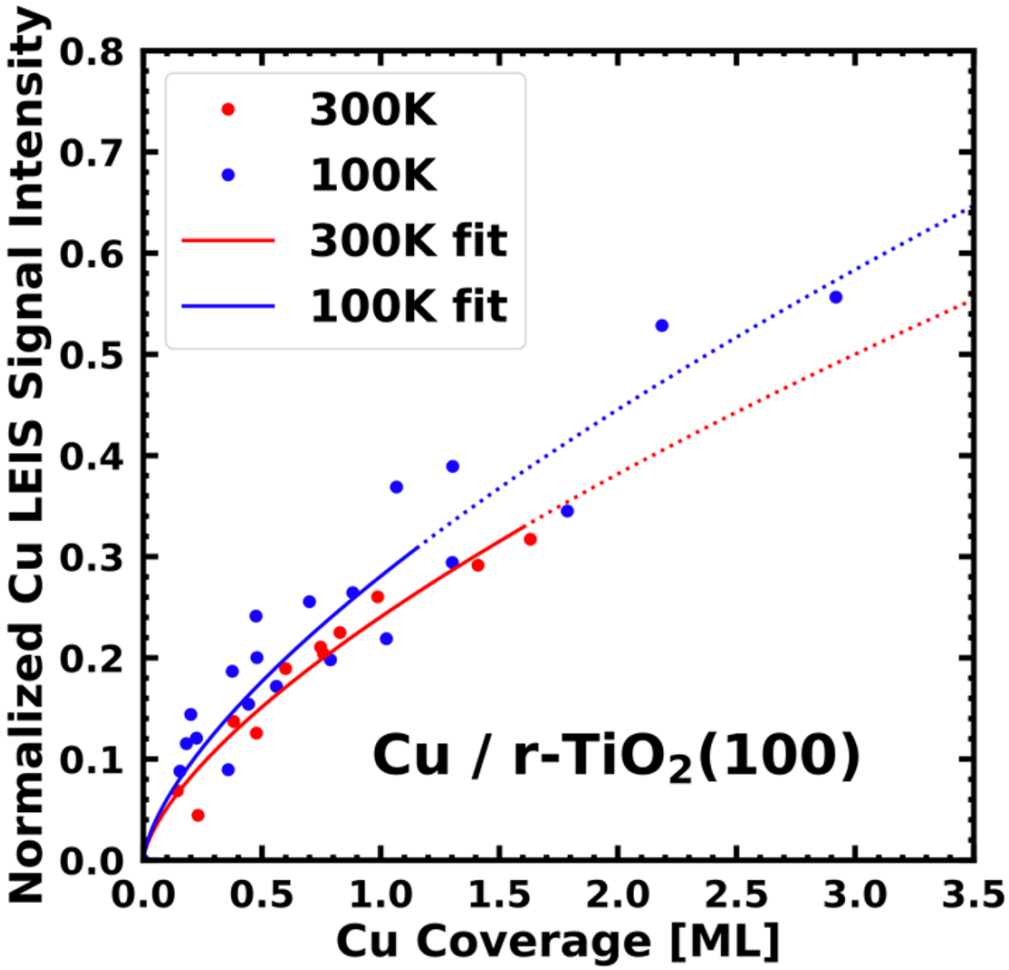

Figure 4.2. Integrated Cu LEIS signals as a function of Cu coverage at 300 K (red) and 100 K (blue). Signals are normalized to the integrated signal of a thick, continuous Cu multilayer. The lines show the best fit of the data to the HCM, with best-fit values of 1.5×10^{17} and 2.4×10^{17} particles/m^2 at 300 K and 100 K, respectively. The transitions to the dashed lines indicate the Cu coverages where the data were no longer used in calculating the best fits, due to possible overlapping-shadow effects. These fit lines are identical to the fit lines to a spherical cap model (SCM) described in the text with a contact angle of 67° and particle densities of 7.4×10^{16} and 1.2×10^{17} particles/m^2 at 300 K and 100 K, respectively. This SCM model is preferred because it fits better to the measured heat data (see below).

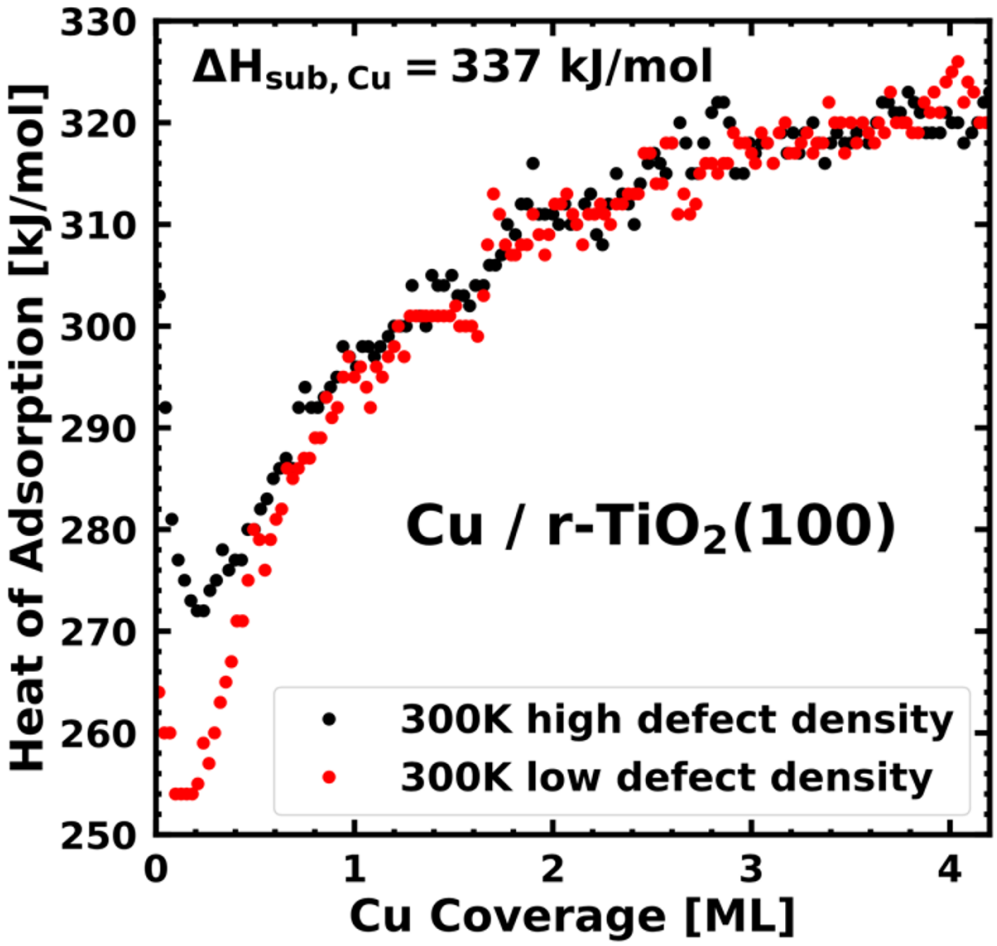

Figure 4.3. Differential heat of Cu adsorption on rutile-TiO_2(100) at 300 K for surfaces that are low in defect density (red) and high in defect density (black).

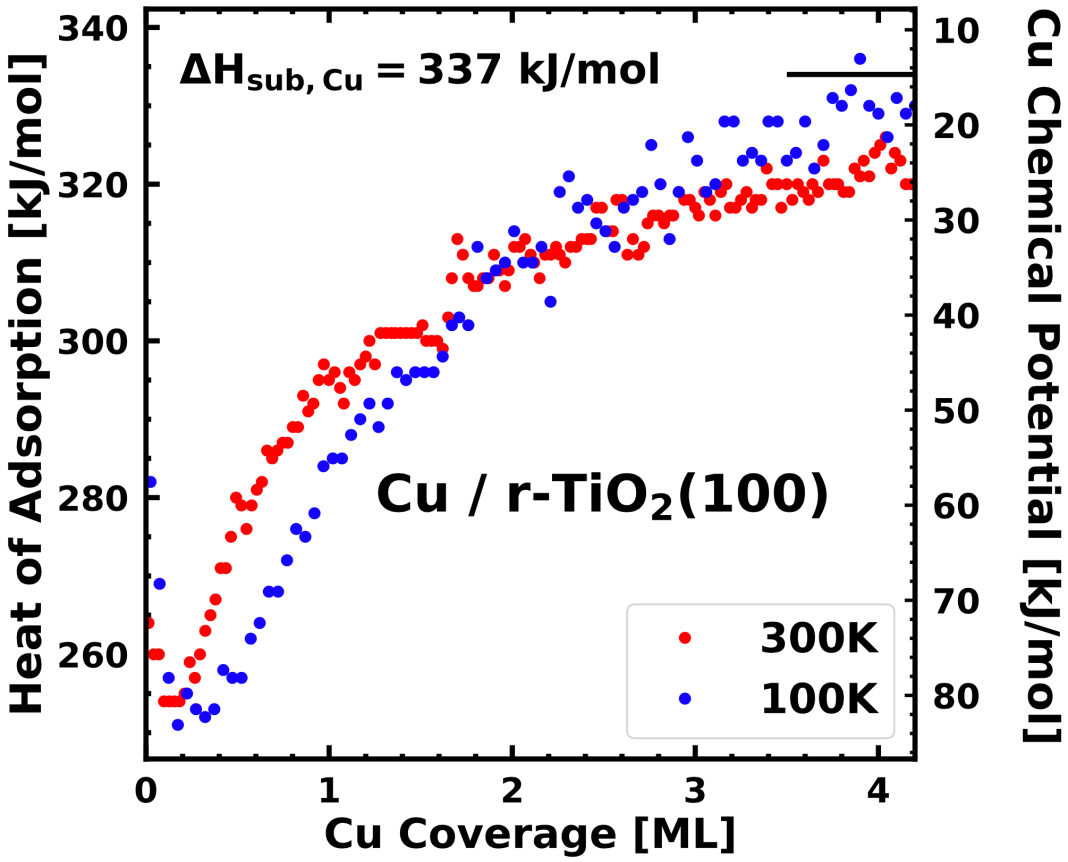

Figure 4.4. Differential heat of Cu adsorption on rutile-TiO_2(100) with low defect density at 300 K (red) and 100 K (blue) as a function of Cu coverage.

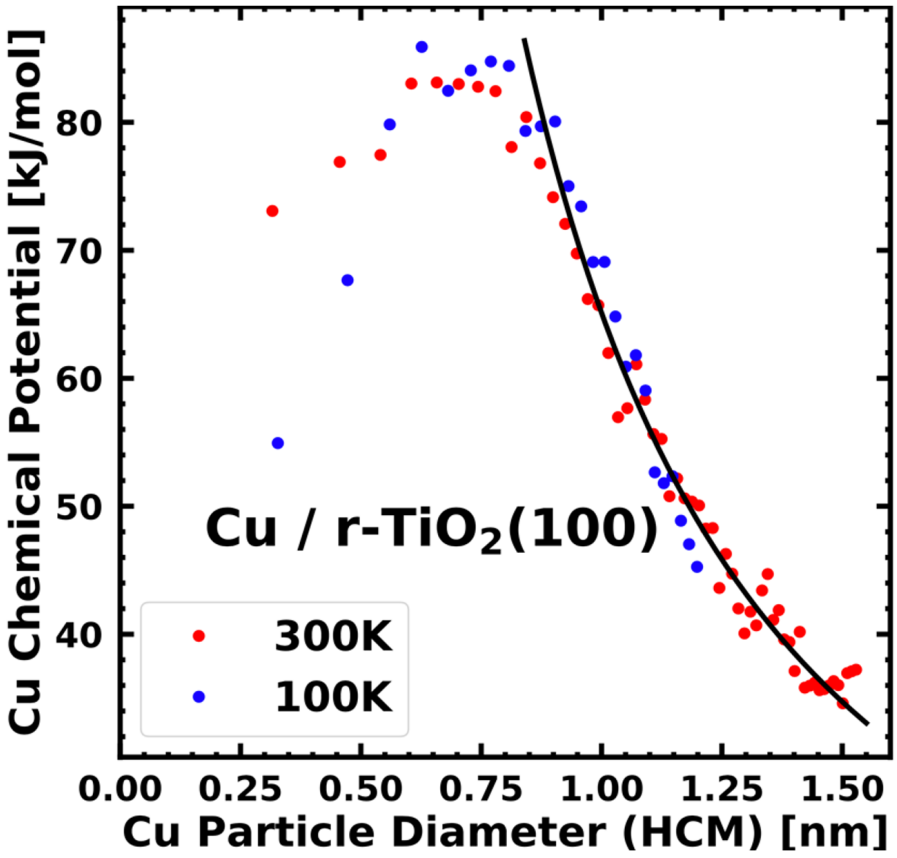

Figure 4.5. Chemical potential of Cu atoms in Cu nanoparticles on rutile-TiO_2(100) (low defect density) at 300 K (red) and 100 K (blue) as a function of effective nanoparticle diameter, assuming the HCM. The black curve shows the best fit to the E_{adh} equation (E_{adh} = 3.57 J/m^2) with D_0 = 1.5 nm.

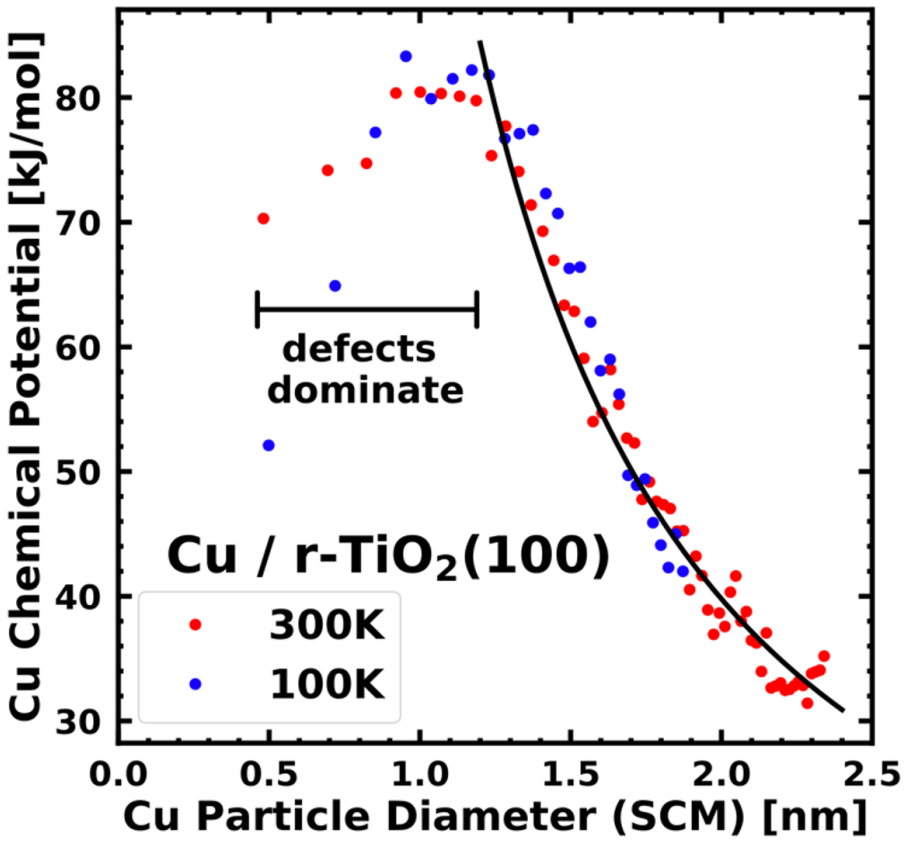

Figure 4.6. Chemical potential of Cu atoms in nanoparticles on rutile-TiO_2(100) (low defect density) at 300 K (red) and 100 K (blue) as a function of nanoparticle footprint diameter, using the SCM. The black curve shows the SCM, Eq. 3, with $E_{adh,SCM}$ = 2.50 J/m^2, θ_c = 67°, and D_0 = 1.5 nm.

Chapter 5. Predicting adhesion energies of late transition metal nanoparticles to oxide support surfaces using oxide reducibility and metal oxophilicity: toward predicting catalyst performance

This chapter has been submitted as:

N. Janulaitis, & C.T. Campbell (2024). *ACS Catalysis*. Under Review.

Chapter Abstract

Adhesion energies between metal nanoparticles and catalyst supports are important for understanding the reactivity and stability of supported nanoparticle catalysts, since they determine the metal chemical potential versus particle size, and this chemical potential dictates both surface reactivity and the rate of deactivation by sintering. A general correlation is presented here for predicting adhesion energies of late transition metals to clean oxide surfaces based on the metal atom's oxophilicity and size and the oxide surface's reducibility (as estimated by its oxygen vacancy formation energy). Previous work had shown that the adhesion energies of metals to MgO(100) and to CeO_2(111) correlate proportionally with the oxophilicity per unit area of the metal, and we show here that this also holds for rutile-TiO_2(100). A linear relationship is then discovered between the proportionality constants measured for these three oxide surfaces and their surface oxygen vacancy formation energies. Adhesion energies of metals to these and several other oxide surfaces are scaled using this correlation between the proportionality constant and the oxygen vacancy formation energy of the oxide, giving a single

trend line for the predicting adhesion energies of many late transition metals to many oxide surfaces with a standard deviation of 0.52 J/m^2 over their 4 J/m^2 range. We also show that the surface oxygen vacancy formation energy can be estimated based on the heat of reduction of the bulk oxide to its next lower oxidation state, at least for the very stable oxide facets studied here.

5.1 Introduction

Efficient catalyst development relies upon a fundamental understanding of how the behavior of catalytic materials (activity, selectivity and long-term stability) depends upon their structural details at the nanometer and atomic scale. Because the stability and chemical reactivity of the active sites are expected to correlate with their energetics, it is important to know how energetics depend upon structural details of the material. Heterogeneous catalysts composed of metal nanoparticles supported on high-surface-area materials such as oxides or graphite are widely used and studied for applications in chemical production, environmental technology, and energy, including clean energy, systems. These types of catalysts and electrocatalysts are complex in structure and function, and predicting their behavior is challenging. The complexity of supported metal nanoparticle catalysts limits computational understanding and prediction because electronic structure theory calculations are often either too limited in accuracy or too expensive. Understanding the energetics of these types of catalysts is critical for understanding and predicting their behavior, as well as providing benchmarks for electronic structure theory, so that faster and more accurate ways of screening catalyst materials may be developed. Discovering the relationships and trends between catalysts' structure and behavior is required to improve the efficiency of developing these catalysts as well as improve the efficiency of the catalysts themselves. *Herein, we report an important step toward predictive design of supported metal nanoparticle catalysts and electrocatalysts, allowing the metal chemical potential to be predicted as a function of particle size for a wide variety of oxide support materials.*

One of the most useful descriptors of nanoparticle catalyst activity is the chemical potential of the metal atoms in the catalyst material, which is a measure of the metal nanoparticle's thermodynamic reactivity, which in turn directly relates to the surface reactivity,

stability and sintering resistance of the nanoparticles.[19] Nanoparticles with lower chemical potential are less reactive and more stable, and, therefore, less prone to deactivation via sintering. Sintering, whereby nanoparticles grow in size and shrink in number, is a major problem for many industrial catalytic processes[9,21] because, when catalysts sinter, both the metal surface area decreases and the chemical potential of the nanoparticles is reduced, so they become less reactive per unit area.[17] Effective catalysts should have a metal chemical potential that is high enough so that they exhibit a high activity for the reaction of interest, but not so high that the catalyst quickly deactivates due to sintering.

The chemical potential of metal atoms in nanoparticles on catalyst supports is a function of particle size (diameter, D), molar volume (V_m) and surface energy (γ_m) of the metal, and adhesion energy per unit area between the metal and support (E_{adh}). Assuming the particles have the shape of hemispherical caps of equal sizes, the chemical potential has been previously derived as:[61]

$$\mu_{HCM}(D) = (3\gamma_m - E_{adh})\left(1 + \frac{D_0}{D}\right)\left(\frac{2V_m}{D}\right), \quad (5.1)$$

where $(1 + D_0/D)$ with $D_0 = 1.5$ nm is an empirical factor that accounts for increases in surface energy and adhesion energy with decreasing D, with γ_m and E_{adh} defined here as their values in the large-particle size limit. The chemical potential using the hemispherical cap model (HCM) is shown in Eq. 1 for simplicity; however, it is generally much more accurate to consider the particles as having the shape of spherical caps with some contact angle, θ_c, at the metal / support interface that is not limited to 90°.[60] A spherical cap is the equilibrium shape that would be assumed by particles if the surface energy of the metal were independent of facet. (Facet dependence can be considered in defining facetted particle shape via the Wulff-Winterbottom

construction,[154] but the metal chemical potential has not been modelled within that theory yet.) At equilibrium, θ_c and E_{adh} are related by the Young-Dupré equation:[62]

$$E_{adh} = \gamma_M(1 + \cos(\theta_c)). \quad (5.2)$$

Within this spherical cap model (SCM), the chemical potential, μ_{SCM}, as a function of the spherical cap footprint radius, r, is given by:[60]

$$\mu_{SCM}(r) = \{[2\alpha(\theta_c) + 1]\,\gamma_M - E_{adh}\}\frac{2}{\alpha(\theta_c)\,\beta(\theta_c)}\left(1 + \frac{D_0\sin(\theta_c)}{2r}\right)\left(\frac{V_m}{r}\right), \quad (5.3)$$

where $\alpha(\theta_c)$ and $\beta(\theta_c)$ are simply-defined functions of the contact angle, θ_c, at the nanoparticle / support interface: $\alpha(\theta_c) = 1/[1 + \cos(\theta_c)]$ and $\beta(\theta_c) = [(2 + \cos(\theta_c)(1 - \cos(\theta_c)]/[\sin(\theta_c)]$.[60]

Because γ_m and V_m are constant for any given metal element, the adhesion energy is the only way that the chemical potential of that metal may be tuned when it is in the form of nanoparticles of a given size, within this model. Equation 3, when combined with Equation 2, shows that adhesion energy and chemical potential are directly related to one another, meaning that adhesion energy is an excellent descriptor and predictor of metal chemical potential versus particle size. Predicting adhesion energies between metals and surfaces therefore directly corresponds to predicting chemical potentials of nanoparticle/support catalysts as a function of particle size.

On given oxide, or carbon-based, surfaces, proportionality relationships between adhesion energies and metal oxophilicity,[18,37,38] or carbophilicity in the case of carbon-based surfaces,[38,135] have been published for CeO_2(111), MgO(100), and graphene/Ni(111). These correlations are powerful tools for predicting adhesion energies of unstudied metal/support combinations, but they are limited to the surfaces that have published correlations, because the trends of adhesion energies across different surfaces is still poorly understood. In this paper, we

present a third oxide correlation based on measurements of the adhesion energies of metals on rutile-TiO_2(100). We compare this oxide trend to those that have been published for CeO_2(111) and MgO(100) to discover a new correlation that allows predicting adhesion energies for metals across the range of oxide supports. We test this prediction with measurements of individual metal's adhesion energies on other oxide surfaces (Fe_3O_4(111), α-Al_2O_3(0001), and rutile-TiO_2(110)), and find good agreement.

These results provide a new way for estimating adhesion energies for late transition metals on oxide surfaces. This in turn allows prediction of the equilibrium contact angle and metal chemical potential versus particle size for that metal / oxide system (see above). This is an important step forward for predictive design of improved catalyst and electrocatalyst materials.

5.2 Results and Discussion

Adhesion energies of metals on two oxide surfaces, CeO_2(111) and MgO(100), have been found to be proportional to the oxophilicity of the metal,[38] as shown in Figure 5.1. Oxophilicity, a measure of how strongly one metal atom binds O atoms, is defined here as the difference between the sublimation enthalpy of the metal, $\Delta H_{sub,M}$, and the formation enthalpy of the most stable metal oxide of the metal per mole of metal atoms, $\Delta H_{f,MOx}$.[155] In this paper, as in ref.[156], we use oxophilicity per unit area (or "Oxo" for short), so this difference in molar enthalpies (in kJ/mol) is divided by the area per mole of metal atoms (estimated as the atomic volume in the bulk metal ($\Omega_M = V_m/N_A$) to the 2/3 power times Avogadro's number, N_A), so Oxo equals $(\Delta H_{sub,M} - \Delta H_{f,MOx})/(\Omega_M^{2/3} N_A)$. The area per mole of metal atoms varies little from one late transition metal element to another, so variations in Oxo are dominated by oxophilicity differences.

For CeO_2(111), the proportionality constant, or the slope of the trendline correlating adhesion energies on this surface and Oxo of the metal has been previously determined to equal 0.188,[38] as reproduced in Figure 5.1. (This reference also provides all the individual E_{adh} and Oxo values for these metals.) For MgO(100), the slope was found to equal 0.102,[38] as reproduced in Figure 5.1. (This reference also provides all the individual E_{adh} and Oxo values for these metals.) The E_{adh} values used in determining these slopes are mainly from single crystal adsorption calorimetry (SCAC) measurements of heats of adsorption of metal vapor versus coverage.[27] These values are based upon fits of the SCAC heats and He^+ low-energy ion scattering spectroscopy (LEIS) intensities versus coverage to the recently-developed SCM.[60] Older linear (but non-proportional) correlations of E_{adh} with Oxo have been published,[18,37] but these were based on E_{adh} values estimated instead with the less-accurate HCM. Values of E_{adh} based on particle shape measurements are also included in Figure 5.1. For full details on how all these adhesion energies were obtained, see ref.[38,157]

The adhesion energy of Ag / rutile-TiO_2(100) has been previously measured using SCAC and found to be 1.64 J/m^2,[35,38] and, more recently, E_{adh} for Cu has been measured by SCAC for this same surface and found to be 2.5 J/m^2.[157] These data have been added to Figure 5.1, and are also well fitted by the best-fit proportional line shown. The slope of this adhesion energy versus Oxo proportional line for this surface is equal to 0.169.

The proportionalities of E_{adh} with Oxo in Figure 5.1 indicate that these metal nanoparticles' attraction to oxide surface is dominated by the bond strength between metal atoms in the nanoparticle and the oxygen atoms in the oxide surface, which should increase in strength with metal oxophilicity.

The proportionality constants in Figure 5.1 for $CeO_2(111)$ and rutile-$TiO_2(100)$ are similar, with adhesion energy values (measured using SCAC) for both Ag and Cu consistently about 4% lower on rutile-$TiO_2(100)$ than $CeO_2(111)$. Adhesion energies on MgO(100) are nearly 50% smaller than on $CeO_2(111)$, but still proportional to metal oxophilicity (or Oxo). Based on the trendlines, the adhesion energies of other metal/support combinations that have not yet been studied can be predicted. The predicted values can be used to screen for catalyst materials that are most likely to behave in a desirable way and inform further research. These predictions for $CeO_2(111)$ and MgO(100), based on the lines shown here, have been published.[156]

Although the trends in Figure 5.1 are valuable, obtaining such trends for a new oxide surface would be costly and slow, because rigorous experimentation would be needed to obtain a few accurate adhesion energy values required to determine the slope of the trendline for each new surface. A more general correlation that could predict adhesion energies across multiple oxide surfaces, e.g. predict the E_{adh} vs Oxo proportionality constant for other oxides, would be extremely valuable. The discovery of the rutile-$TiO_2(100)$ surface trend in Figure 5.1 provides a third slope value, which is essential for correlating this slope to some property of the oxide or its surface. Because metal nanoparticles' interaction with the surface is dominated by their bonding to the oxygen atoms in oxide surfaces, the E_{adh} / Oxo slope values likely correlate best with some measure of the chemical potential of the oxygen atoms on each oxide surface, with stronger adhesion to metals expected for oxide surfaces with higher oxygen atom chemical potential. Two relatively easy-to-access measures of this O chemical potential (or the instability of O atoms in the oxide surface) are the negative of the standard enthalpy of reduction of each bulk oxide to its next lower oxidation state, $-\Delta H_{red,ox}$, and the negative of the oxygen vacancy formation energy of the oxide surface, $-\Delta E_{Ov}$. This $-\Delta H_{Ov}$ value is conceptually preferred since it depends upon

the crystal face of the oxide being considered (while $-\Delta H_{red,ox}$ relates only to the bulk), but no ΔE_{Ov} have been measured, so they can only be approximated by DFT calculations (which have errors), whereas $\Delta H_{red,ox}$ values are known experimentally. O'Connor et al.[158] showed that the DFT-calculated binding energies of Ag, Pd and Ir atoms to several oxide surfaces increase nearly linearly with the negative DFT-calculated ΔE_{Ov}, supporting the expected trend mentioned above.

We show the slope values for each oxide surface from Figure 5.1 above plotted as a function of $-\Delta H_{red,ox}$, in Figure 5.2a, and as a function of $-\Delta E_{Ov}$, in Figure 5.2b. The data values for the X axes in these plots are listed in Table 5.1, along with citations for their sources and these values for the other three oxide surfaces (Fe_3O_4(111), α-Al_2O_3(0001), and rutile-TiO_2(110)) to be discussed below.

In Figure 5.2a, $\Delta H_{red,ox}$ are bulk values calculated from formation enthalpies of oxides.[144] In Figure 5.2b, the ΔE_{Ov} values are from DFT calculations of CeO_2(111),[158,159] MgO(100),[158,160] and rutile-TiO_2(100).[161] For each of these two descriptors, the best-fit straight line is shown. For these surfaces, multiple DFT calculations of ΔE_{Ov} have been reported. The larger circles in Figure 5.2b are points used to find the line of best fit. These are the most rigorously calculated DFT values (i.e. using the highest level of theory and largest supercell size, because ΔE_{Ov} values are known to converge as cell size increases)[162]. The smaller points in Figure 5.2b are shown to demonstrate existing variations in DFT results. The quality of the linear fit is good, and similar for both descriptors (with standard deviations of 4.7×10^{-5} and 4.5×10^{-5} for Figures 5.2a and 5.2b, respectively). The correlation in Figure 5.2b has the disadvantage of not being surface-specific, but it is valuable for estimating E_{adh} / Oxo for some surfaces, such as Fe_3O_4(111), for which ΔE_{Ov} has not been reported. It is surprising that $\Delta H_{red,ox}$ is so similar to ΔE_{Ov} for these

three oxide surfaces, in spite of its lack of surface facet specificity. Figure 5.3 shows ΔE_{Ov} plotted versus $\Delta H_{red,ox}$ for different oxide surfaces.

The ΔE_{Ov} values for oxides versus their bulk $\Delta H_{red,ox}$ values, shown in Figure 5.3, are best fitted by the line:

$$\Delta E_{Ov} = 0.956\,\Delta H_{red,ox} + 20.7 \text{ kJ/mol O.} \quad (5.4)$$

Figure 5.3 shows that the variations in ΔE_{Ov} across different facets of the same oxide are much smaller than the variations in $\Delta H_{red,ox}$ across different oxides. Because of this difference in variation magnitude, Equation 5.4 may reasonably be used to estimate the ΔE_{Ov} of an oxide based on the $\Delta H_{red,ox}$ of that oxide. Although the resulting ΔH_{Ov} value is not surface-specific, Figure 5.3 shows that the different surfaces of the oxide are likely to have relatively similar ΔE_{Ov}'s, so this estimate only introduces a small error. This error may be less than the error introduced by uncertainties in DFT values themselves, which can vary based on the exact computational method used. Thus, on oxide surfaces for which the ΔE_{Ov} has not yet been calculated, Equation 5.4 may be used to get an approximate ΔE_{Ov} value, from which E_{adh} / Oxo may then be calculated using the line in Figure 5.2b. Wexler et al.[163] showed a linear correlation similar to the one in Figure 5.3, but for forming bulk oxygen vacancies rather than surface O vacancies, and for more complex oxides, with a correction for band-gap differences.

Based on the good linear correlations in Figure 2, we postulate that the E_{adh} vs. Oxo proportionality constant (f = E_{adh} / Oxo) can be estimated for any oxide surface using the best-fit lines in Figure 5.2. For example, as shown in Figure 5.2b, the E_{adh} vs. Oxo proportionality constant is given by:

$$f = Eadh / Oxo = (2.11 \times 10^{-4})(\Delta E_{Ov} / (kJ/mol)] + 0.234. \quad (5)$$

Equation 5.5 can be used to calculate E_{adh} / Oxo for any oxide surface for which ΔE_{Ov} is known from reliable DFT; and, since Oxo is known for all the late transition metals, one can also estimate E_{adh} for any late transition metal on that specific oxide surface. If a ΔE_{Ov} has not yet been reported for a given oxide surface, Equation 5.4 may be used to estimate the ΔE_{Ov} value needed for Equation 5.5. Alternatively, the Equation in Figure 5.2a may be used to estimate E_{adh} / Oxo, but, because the fit in Figure 5.2b to Equation 5.4 is based on more oxide data, it is slightly preferred over the fit in Figure 5.2a.

If our postulate for predicting E_{adh} / Oxo is true, Equation 5.5 should be useful for scaling the adhesion energies on all oxide surfaces to a single trendline. Figure 5.4 shows the result, using all the reliable measured E_{adh} values we know for late transition metals on clean, well-defined oxide surfaces. All values are plotted here with respect to the E_{adh} vs. Oxo proportionality constant for MgO(100), because it is based on a fit to more measured adhesion energies than the CeO_2(111) or rutile-TiO_2(100) fits. Also, the DFT values of ΔE_{Ov} show the least deviation for MgO(100). Oxo values are scaled using the ΔE_{Ov}-based correlation in Figure 5.2b (Equation 5.5), unless ΔE_{Ov} for the surface has not yet been reported. The measured adhesion energies and Oxo values for metals on all three surfaces in Figure 5.1, as well as for metals on three additional oxide surfaces (Fe_3O_4(111), α-Al_2O_3(0001), and rutile-TiO_2(110)) are scaled in this way and plotted in Figure 5.4. We note that the ΔE_{Ov} value for Fe_3O_4(111) has not yet been reliably estimated computationally, due to the complicated electronic structure of this surface. For this surface, ΔE_{Ov} was estimated based on the reported $\Delta H_{red,ox}$ of Fe_3O_4[144] using Equation 5.4 above. The data shown in Figure 5.4 are also presented in Table 5.2.

As seen, the adhesion energies for these many metal / oxide combinations in Figure 5.4 are very well fit by the best proportional fit to these data, given by:

$$E_{adh} = 0.097[\text{f(that oxide)}/\ \text{f(MgO(100))}][(\Delta H_{sub,M} - \Delta H_{f,MOx})/(\Omega_M^{\frac{2}{3}} N_A)] \quad (6)$$

$$= 0.097[\text{f(that oxide)}/\ 0.106)][(\Delta H_{sub,M} - \Delta H_{f,MOx})/(\Omega_M^{\frac{2}{3}} N_A)]$$

$$= 0.097[9.40\ \text{f(that oxide)}[(\Delta H_{sub,M} - \Delta H_{f,MOx})/(\Omega_M^{\frac{2}{3}} N_A)].$$

The function f in Equation 5.6 is obtained from Equation 5.5, based on the fit in Figure 5.2b. Scaling Oxo as shown in Equation 5.6 clearly reduces the multiple trendlines in Figure 5.1 to a single trendline that predicts E_{adh} for multiple oxide surfaces with reasonable accuracy. Because the data is scaled with respect to MgO(100), the ideal slope of this trendline would be 0.102 if our postulate were completely accurate. The actual best-fit slope of the line for all the data shown in Figure 5.4 is 0.097, which is nearly equal to this ideal slope, reflecting the accuracy of this postulate. The fit of the data to this proportionality is very good, with a standard deviation of 0.52 J/m^2 and a r2 score of 0.75.

Large errors relative to this best fit in Figure 5.4 is seen in some of the measured adhesion energy values for Ag and Au, which fall significantly below the fit line. However, the deviations amongst the measured values for these metals are larger than for other metals. The adhesion energy for Cu / α-Al_2O_3(0001) is also well above the trend line. This stronger binding could be due to interactions between the adhering metal and the metal in the oxide surface.

The correlation in Figure 5.4 (Equation 5.6) finally allows adhesion energies to be estimated across many oxide surfaces. To estimate the adhesion energy of some metal on some oxide surface, the only information needed is the Oxo of the metal (see ref[38] for Oxo values for most late transition metals) and the ΔH_{Ov} (or $\Delta H_{red,ox}$) of the oxide surface. The ΔE_{Ov} (or $\Delta H_{red,ox}$) is plugged into the appropriate correlation in Figure 5.2 to estimate the E_{adh} / Oxo proportionality slope of that oxide, and the adhesion energy for any metal on that oxide is simply

equal to this slope multiplied by that metal's Oxo value. This prediction process simply involves combining Equation 5.5 with Equation 5.6, and, when necessary, using Equation 5.4.

Hu and Li[151] presented a large amount of data where the measured adhesion energies of metals on oxides and other supports, divided by $2\gamma_m$, was shown to be closely approximated as being equal to the single metal atom binding energy to the surface (E_{bs}, calculated by DFT) divided by the bulk metal cohesive energy (E_c): $E_{adh} / (2\gamma_m) = E_{bs} / E_c$. However, most of their adhesion energy values for oxide surfaces were measured on surfaces that were not verified to be clean, and such values are known to generally be far below the values measured on clean oxide surfaces.[17,37,155] In an attempt to validate their trend, Figure 5.5 shows adhesion energies plotted in this format, now using only values measured for oxide surfaces that were verified to be clean in UHV, and using only the same E_{bs} values as cited by Hu and Li in that paper,[151] taken from ref. [158]. Figure 5.5 includes adhesion energy values measured on clean MgO(100), CeO_2(111), and α-Al_2O_3(0001). Table 5.3 is a table of these data.

As shown in Figure 5.5, these clean-surface data do not fit well to the trend predicted by Hu and Li[151] (the dashed parity line), having a standard deviation of 2.2 J/m^2, more than 4 times that for the predictions of Equation 5.6 in Figure 5.4. The results in Figure 5.4 do not support the trend proposed by Hu and Li, and show that $E_{adh} / (2\gamma_m)$ is not closely approximated by E_{bs} / E_c. This reinforces the importance of the trends shown in Figures 5.2, 5.3 and 5.4 for predicting adhesion energies of metals on oxide surfaces. Note that these clean-surface adhesion energy measurements in Figure 5 are generally considerably higher in value than the prediction line of Hu and Li, which was based on data from surfaces that had not been verified to be clean. This further confirms our previous findings that such values are known to generally be far below the values measured on clean oxide surfaces. [17,20,37]

The adhesion energy of a metal nanoparticle to a surface dictates the metal chemical potential of the metal nanoparticles on that surface and its particle-size dependence. The metal chemical potential correlates with the surface reactivity, stability, and sintering-resistance of the metal nanoparticles on a surface. Therefore, the ability to predict the adhesion energy at any given late transition metal / oxide interface based on the correlation in Figure 5.4 is an important step toward predicting the fundamental properties and behavior of catalytic metal nanoparticles on a wide variety of oxide surfaces. These predictions for transition metal nanoparticles supported on oxide surfaces will aid in designing efficient catalysts and identifying catalysts of interest for further study.

5.3 Conclusion

Correlations for predicting adhesion energies of late transition metals on differing oxide surfaces are presented. Using the relationships reported here, the first step to estimating the adhesion energy for a new metal / oxide combination is determining the surface oxygen vacancy formation energy of the oxide from DFT calculations. If this oxygen vacancy formation energy is not available, it may be estimated using Equation 5.4 from Figure 5.3, which shows that the oxygen vacancy formation energy is closely related to the heat of reduction of the bulk oxide to its next lower oxidation state. Once this oxygen vacancy formation energy has been determined or estimated, the E_{adh} / Oxo value, which is the proportionality constant between the oxophilicity per unit area of the metal and the adhesion energy of the metal on a given oxide, is determined from Equation 5.5 from Figure 5.2b. Once this E_{adh} / Oxo ratio is determined, the adhesion energy of any late transition metal to that oxide can be estimated from the oxophilicity per unit area of that metal. The oxophilicities per unit area of many late transition metals may be found in ref.[38] Figure 5.5 shows that previous relationships for predicting adhesion energies based on

single atom binding energy[151] do not always hold, which stresses the importance of the relationships presented above, which are based on high-quality experimental adhesion energies of metals on clean surfaces.

5.4 Figures

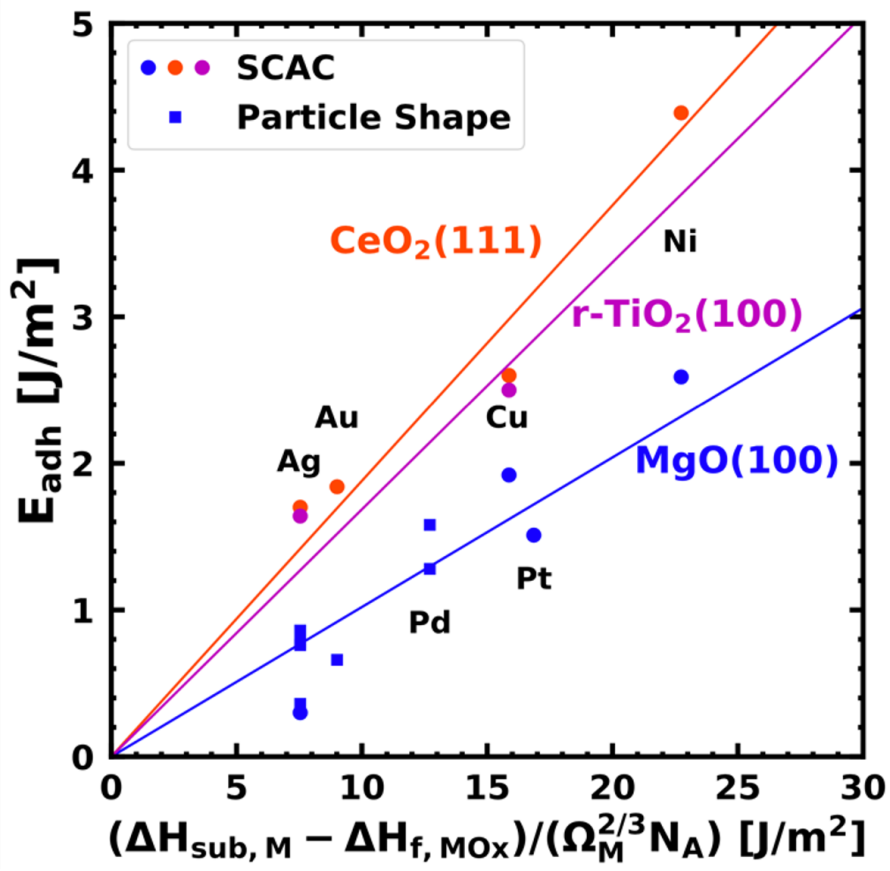

Figure 5.1. The adhesion energy of metals on CeO_2(111), rutile-TiO_2(100), and MgO(100) as a function of metal oxophilicity per unit area (Oxo). Solid lines are the best linear fits passing through (0, 0) for each oxide. Slope values are 0.188 for CeO_2(111), 0.169 for TiO_2(100), and 0.102 for MgO(100). Circular points are SCAC measurements (using the SCM or flat-disk model), and square points are particle shape measurements. For additional details on the CeO_2(111) and MgO(100) data, see ref.[38]

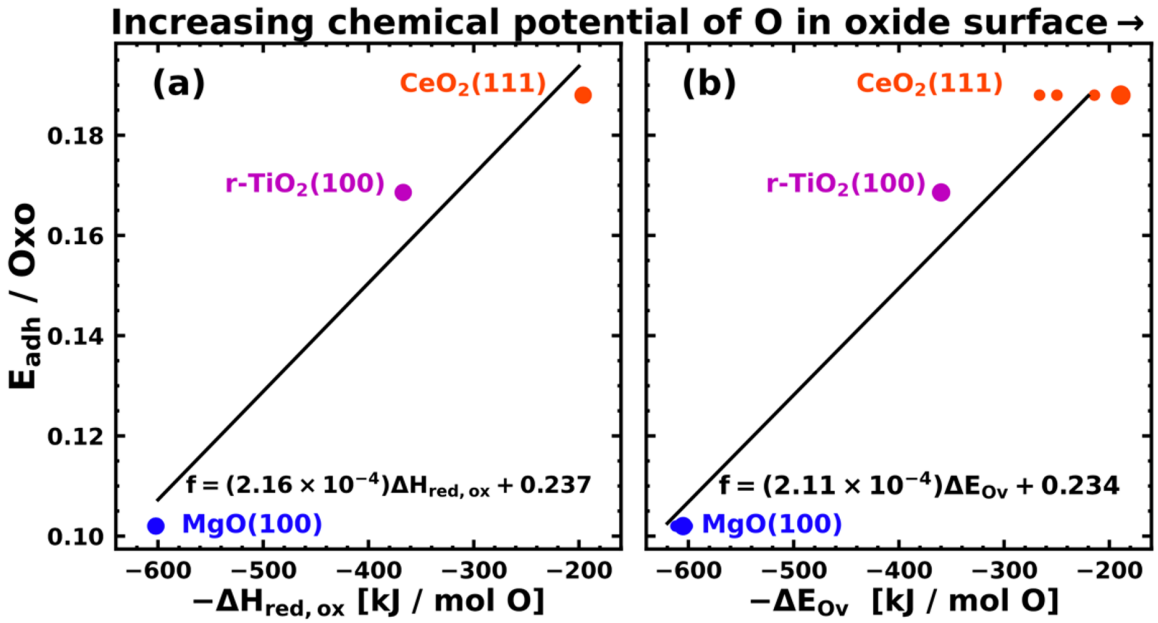

Figure 5.2. The slope for correlating adhesion energy of metals on oxides with metal oxophilicity for each of the oxides is plotted as a function of (a) the negative standard enthalpy of reduction of each oxide to its next lower oxidation state plus ½ O_2(gas), $\Delta H_{red,ox}$, and (b) DFT-calculated negative oxygen vacancy formation energies for the oxide surfaces. The larger circles are the ΔE_{Ov} values reported for CeO_2(111),[164,165] rutile-TiO_2(100),[166] and MgO(100)[165,167] which are used to calculate the line of best fit. Some DFT values (smaller circles) were excluded in this fit because they were calculated using larger or unstated vacancy concentrations or a lower level of theory. For comparison, other reported DFT values are shown as smaller circles. The data in this plot and corresponding citations are listed in Table 5.1.

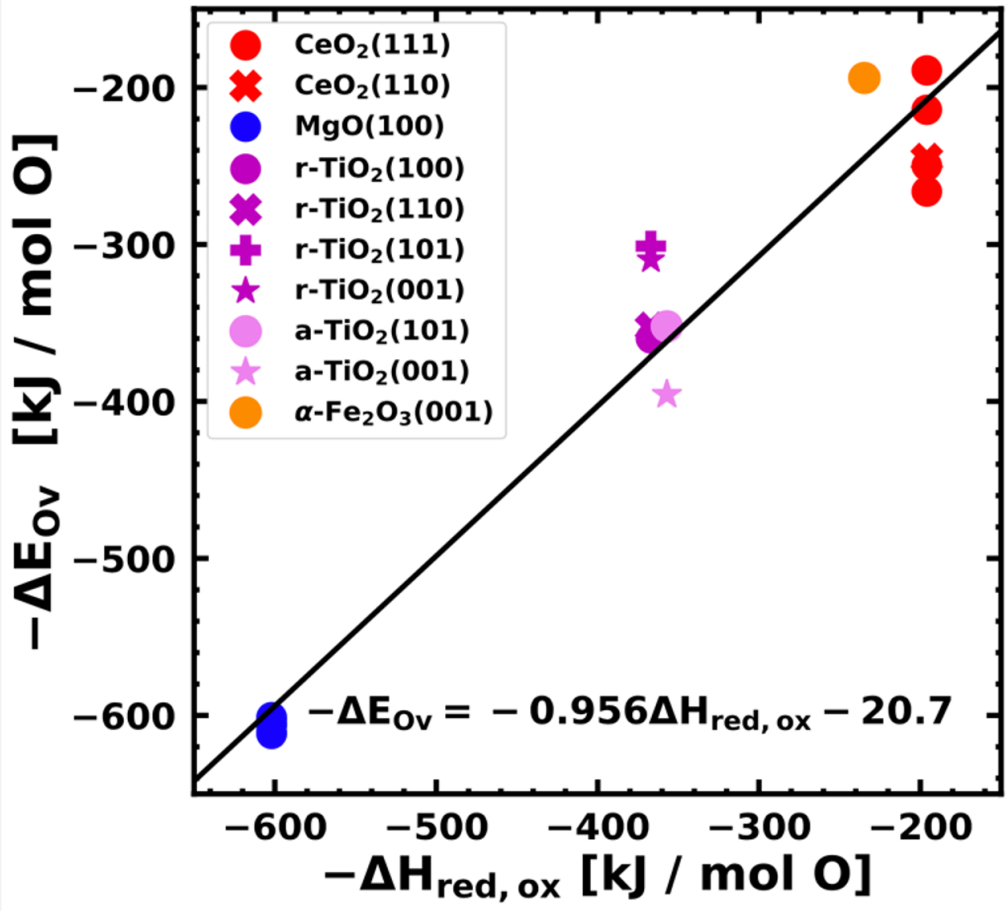

Figure 5.3. The oxygen vacancy formation energies, ΔE_{Ov}, for CeO_2, TiO_2, MgO, and Fe_2O_3 surfaces are shown as a function of the standard enthalpy of reduction of the bulk oxide to its next lower oxidation state plus ½ O_2 gas, $\Delta H_{red,ox}$. The line of best fit through the points is shown in black, with the equation of the line, showing that it is a near 1:1 proportionality. The data shown here are listed in Table 5.1.

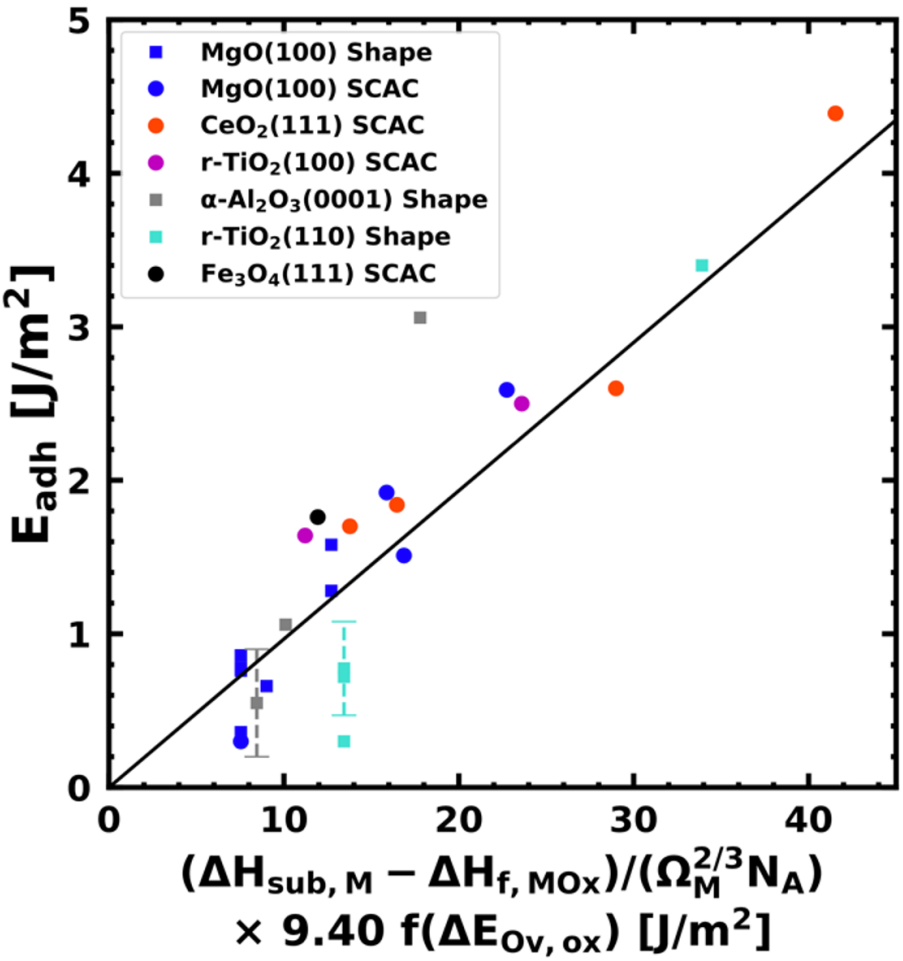

Figure 5.4. The measured adhesion energies of metals on CeO_2(111), rutile-TiO_2(100), MgO(100), rutile-TiO_2(110), Fe_3O_4(111), α-Al_2O_3(0001), and rutile-TiO_2(110) as a function of metal oxophilicity per unit area, scaled by f(oxide)/ f(MgO(100)), as in Equation 5.6. Each f(oxide) is calculated from the fit in Figure 5.2(b) (Equation 5.5), whereby f(MgO(100) = 0.106. The solid line here is the proportional line of best fit, with a slope of 0.097. The standard deviation of the measured E_{adh} values from this best fit line is 0.52 J/m^2, and its r2 score is 0.75.

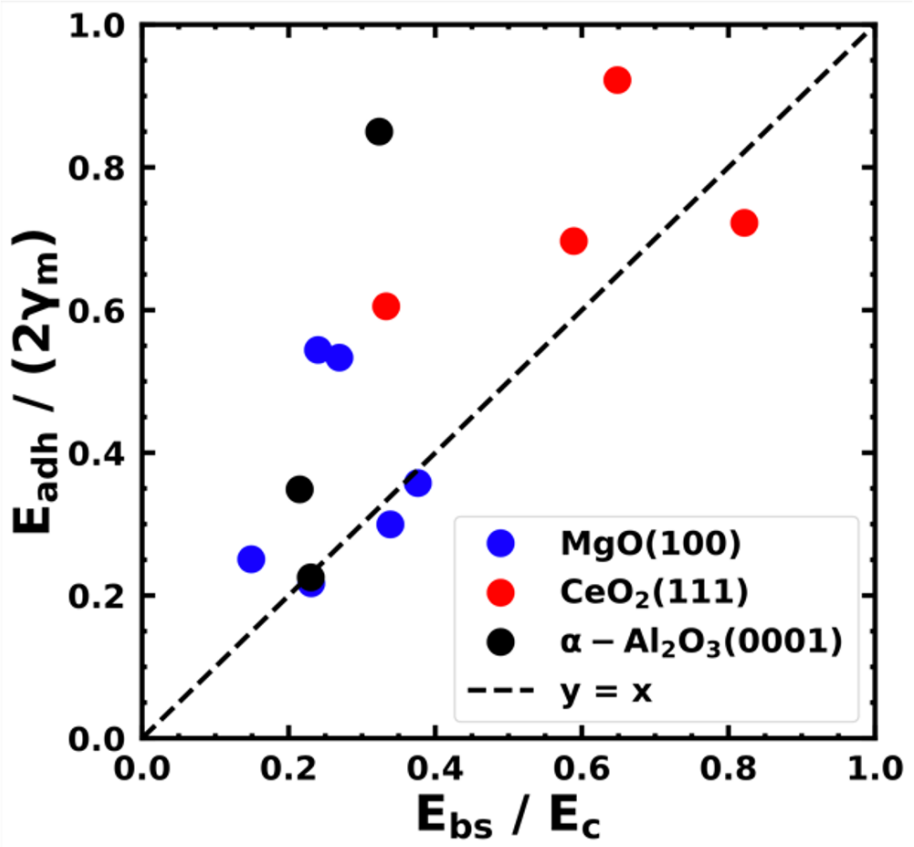

Figure 5.5. The adhesion energies for late transition metals measured on clean, well-defined oxide surfaces, normalized by twice the surface energy of the metal, plotted as a function of the DFT-calculated single metal atom binding energy to the surface, normalized by the sublimation energy of the metal. The dashed parity line (where these values would equal each other) is the correlation suggested by Hu and Li in ref.[151]. The standard deviation from and r^2 value for the parity line are 2.2 J/m^2 and 0.090, respectively. The standard deviation from and r^2 value for the line of best fit to these data (not shown) are 0.47 and 1.9 J/m^2, respectively. For plot data, see Table 5.3.

5.5. Tables

Table 5.1. The best-fit proportional slopes of the adhesion energy of metals on oxides versus the metal oxophilicity (per area) for each of the oxide surfaces (from Figure 5.1), the standard enthalpies of reduction of the bulk oxides to their next lower oxidation state plus ½ O_2(gas) ($\Delta H_{red,ox}$), and DFT-calculated oxygen vacancy formation energies for these oxide surfaces (ΔE_{Ov}). The bold values are those used to calculate the line of best fit (f) shown in Figure 5.2b.

Surface	**E_{adh} vs. Oxo slope**	**$\Delta H_{red,ox}$ [kJ / mol O]**	**ΔE_{Ov} [kJ / mol O]**	**Citation for ΔE_{Ov} value**	**f($E_{Ov,\ ox}$)**
CeO_2(111)	0.188	196	**189**	[159]	0.194
			266	[158]	
			214	[159]	
MgO(100)	0.102	602	601	[160]	
			603	[160]	
			611	[160]	
			605	Average of 3 values from Richter et al.[160] (used for fit)	0.106
			606	[158]	
			612	[160]	
r-TiO_2(100)	0.169	367	**360**	[161]	0.158
CeO_2(110)		196	**246**	[158]	
r-TiO_2(110)		367	**353**	[161]	
r-TiO_2(101)		367	**301**	[161]	
r-TiO_2(001)		367	**310**	[161]	
a-TiO_2(101)		357	**352**	[168]	
a-TiO_2(001)		357	**396**	[168]	
α-Fe_2O_3(001)		235	**194**	[169]	

Table 5.2. Adhesion energies for late transition metals on oxide surfaces, as well as the method by which they were obtained, and the scaled Oxo values via Equation 5.6, using the $f(E_{Ov,ox})$ (=f(ox)) values from Equation 5.5, which gives f(MgO(100)) = 0.106. These two values are plotted against each other in Figure 5.4.

Surface	Metal	E_{adh} Measurement Method	E_{adh} [J / m^2]	Oxo*[f(ox)/f(MgO)] [J / m^2]	Citation for E_{adh}
MgO(100)	Ag	SCAC	0.3	7.54	[31]
	Ag	SDRS	0.76 ± 0.08	7.54	[170]
	Ag	GISAXS	0.86 ± 0.2	7.54	[170]
	Ag	GISASXS	0.78 ± 0.1	7.54	[171]
	Ag	HRTEM	0.36 ± 0.08	7.54	[172]
	Au	HRTEM	0.66	9.01	[173]
	Pd	HRTEM	1.28	12.71	[174,175]
	Pd	GISAXS	1.58	12.71	[176,175]
	Cu	SCAC	1.92	15.87	[143]
	Pt	SCAC	1.51	16.86	[177]
	Ni	SCAC	2.59	22.74	[63]
CeO_2(111)	Ag	SCAC	1.7	13.76	[63]
	Au	SCAC	1.84	16.44	[63]
	Cu	SCAC	2.6	28.96	[63]
	Ni	SCAC	4.39	41.49	[112]
TiO_2(100)	Ag	SCAC	1.64	11.18	[63]
	Cu	SCAC	2.5	23.53	[178]
TiO_2(110)	Au	SDRS	0.3 ± 0.15	13.39	[179]
	Au	GISAXS	0.47 - 1.08	13.39	[138]
	Au	HRSEM	0.72 ± 0.11	13.39	[137]
	Ni	SDRS	3.4 ± 0.29	33.81	[179]
α-Al_2O_3(0001)	Ag	SDRS	0.2 - 0.9	8.40	[179,180]
	Au	SDRS	1.06 ± 0.08	10.04	[179]
	Cu	SFM	3.06 ± 0.13	17.68	[181]
Fe_3O_4(111)	Ag	SCAC	1.76	31.86	[63]

Table 5.3. Values used to make Figure 5.5. For each metal / surface combination, the metal surface energy (from [38]), bulk metal sublimation energy (ΔH_{sub}, equal to its cohesive energy, E_c), and the single metal adatom binding energy on the surface (E_{bs}, from ref.[158]) is listed. The normalized binding energy, E_{bs}/E_c, and normalized adhesion energy, $E_{adh}/(2\gamma_m)$, as plotted in Figure 5.5, are also listed, using E_{adh} values for clean oxide surfaces from Table 5.2.

Surface	Metal	Metal Surface Energy (γ_m) [J / m^2]	ΔH_{sub} (=E_c) [kJ / mol]	E_{bs} [eV]	E_{bs}/E_c	$E_{adh}/(2\gamma_m)$
MgO(100)	Ag	1.22	285	-0.44	0.149	0.251
	Au	1.52	368	-0.88	0.231	0.217
	Pd	2.00	377	-1.47	0.376	0.358
	Cu	1.80	337	-0.94	0.269	0.533
	Pt	2.52	564	-1.98	0.300	0.339
	Ni	2.38	430	-1.07	0.240	0.544
CeO_2(111)	Ag	1.22	285	-1.74	0.589	0.697
	Au	1.52	368	-1.27	0.333	0.605
	Cu	1.80	337	-2.87	0.822	0.722
	Ni	2.38	430	-2.89	0.649	0.922
α-Al_2O_3(0001)	Ag	1.22	285	-0.68	0.230	0.225
	Au	1.52	368	-0.82	0.215	0.349
	Cu	1.80	337	-1.13	0.324	0.850

Chapter 6. Continuing Small Molecule Adsorption Calorimetry: Understanding the Energetics of Solvents and Reaction Intermediates on Model Catalyst Surfaces for Applications in Catalyst Design

Overview

In 2022, a single-crystal adsorption calorimeter designed specifically to measure the adsorption energies of small molecules on solid surfaces was purchased from the Campbell Group at the University of Washington by Pacific Northwest National Laboratory (PNNL). This calorimeter has a long history of measuring and reporting important energetics that have been used as benchmarks for developing and improving DFT calculations, understanding solvent effects in heterogenous catalytic reactions, and understanding behavior of reaction intermediates on surfaces. To continue this important work, I learned to operate this calorimeter, assisted in moving the instrument to PNNL, and trained scientists there on how to operate and troubleshoot the instrument. To do this, I visited PNNL twice and have ongoing discussions with the scientists there to ensure that the instrument knowledge is passed on and that this unique calorimeter can continue to make an impact on understanding and designing better catalysts. This chapter gives a brief overview of the scientific methods of this calorimeter as well as its past impact and future plans.

6.1 Introduction

Although theoretical methods, and specifically DFT calculations, have become powerful tools for studying catalysts, the complexities of heterogeneous catalytic systems are still difficult to model theoretically, and large energy errors still exist in these calculations.[182] The lack of energy accuracy and reliability in DFT calculations is still a major limitation that still prevents these methods from being able to accelerate catalysis design to the extent that is necessary to keep up with the demand that exists for new and better catalysts, which is driven by today's pressing issues such as lack of sustainability and increasing energy demands.

Although TPD may be used to access adsorption energies for reversible processes, many important species in reactions adsorb via irreversible processes, such as dissociation, so measuring adsorption energies directly is extremely valuable not only for understanding the energetics of common reaction intermediates but also to serve as DFT benchmarks. The calorimeter for directly measuring these adsorption energies uses a PVDF ribbon to directly measure heat changes on the sample, exactly as described in Chapter 2 for the metal vapor adsorption calorimeter, except, for this calorimeter, instead of adsorbing metal vapor produced via an e-beam evaporator, a molecular beam is used to deposit small molecules (i.e., <30 atoms).

This technique has successfully been used to study many molecule / surface combinations and has had a major impact on our fundamental understanding of the energetics of small molecules on metal catalysts and on improving DFT by providing accurate adsorption-energy data on many well-defined adsorbate / metal combinations for benchmark databases.[182–192] Most SCAC studies of this type have focused on the Pt(111)[100,185,187,193–195] surface, because of its excellent catalytic characteristics, but, more recently, surfaces such as Ni(111)[183,184,189,196,197] and

Cu(111)[198] have also been studied, in an effort to expand our understanding of how these molecules behave across different metals.

6.2 Experimental Methods

Most of the principles and methods of the small molecule adsorption calorimeter are similar or identical to those described above in Chapter 2 for the metal vapor adsorption calorimeter, and the details of this calorimeter have been previously published in detail,[199–201] so, here, a brief overview of some key points and differences is given.

The calorimeter is a complex ultrahigh vacuum apparatus with many capabilities. A photograph of it is shown in Figure 6.1. It has a single main chamber which is maintained at a pressure $< 2 \times 10^{10}$ torr, with two regions. A manipulator arm holding the sample is used to move the sample between the two regions. The first region has instrumentation for surface preparation and characterization, and the second region has the calorimetry setup.

In the sample preparation and characterization region, instrumentation for XPS, AES, and LEED is available, as well as an ion gun for sputtering. The scientists at PNNL plan to also add a Knudsen cell to evaporate metal so they can grow oxide films on the single-crystal metal samples for use in future experimental studies of adsorption on well-defined oxide surfaces (see section 6.3 below).

In the calorimetry region, a PVDF heat detection exists that can be translated into contact with the back of the sample to detect heat changes on the single-crystal surface of the sample. During calorimetry, the sample is held in place by a copper block like the one described in Chapter 2. The Cu sample holder can also be cooled via copper cooling braids and a nitrogen gas cooling system to perform experiments at temperatures as low as 100 K. A molecular beam is used to generate a flux of the molecule of interest. A QCM can be translated in line with the

sample to measure the flux. The QCM must be cooled with liquid nitrogen before measuring the flux to ensure that all incident molecules stick to the surface. A laser is used to calibrate the heat measurement and a QMS is used to detect molecules that do not stick to the surface of the sample.

6.3 Future Outlook

To ensure that the calorimeter is operating properly and to help the PNNL team learn the procedures of the calorimeter, the experiments first performed after moving were a repeat of the methanol / Pt(111) system, which has previously been reported.[193] The measurement allowed us to identify issues that needed to be resolved and procedural details that needed to be conveyed.

As a first study, the team plans to use the instrument to study alcohol adsorption on Pt(111) systems, to further confirm that the calorimeter is working properly (by comparing results for methanol to the previously published study using this same apparatus to study methanol on Pt(111))[193] and then to specifically study how the chain length of the alcohol affects its adsorption energy to the Pt(111) surface.

The next main project of interest involves investigating adsorption energies on iron oxide surfaces. Iron oxides are an interesting and promising catalyst supports, which are especially attractive because they are environmentally friendly, abundant, and inexpensive. The calorimeter is currently undergoing modifications including the addition of a Knudsen cell for evaporating metal so that iron oxide may be grown. No SCAC measurements have yet been performed on an iron oxide surface, and DFT calculations particularly struggle with these surfaces, so these measurements are critical to understand adsorption energetics on this surface and to serve as benchmarks for DFT. Some important small molecules that will be studied on this surface are water, formic acid, and methanol. Because these molecules have been studied on other surfaces

with SCAC, studying them on the iron oxide surface would offer an interesting and important comparison to previously published work. Eventually, solvent effects on the adsorption energies on this surface will be investigated, because solvents can have a strong impact on the selectivity and reactivity of a catalyst and are particularly important in electrocatalysis. The small molecule adsorption calorimeter has a long history of making a huge scientific impact on catalysis research and will continue to do so with its future projects.

6.4 Figures

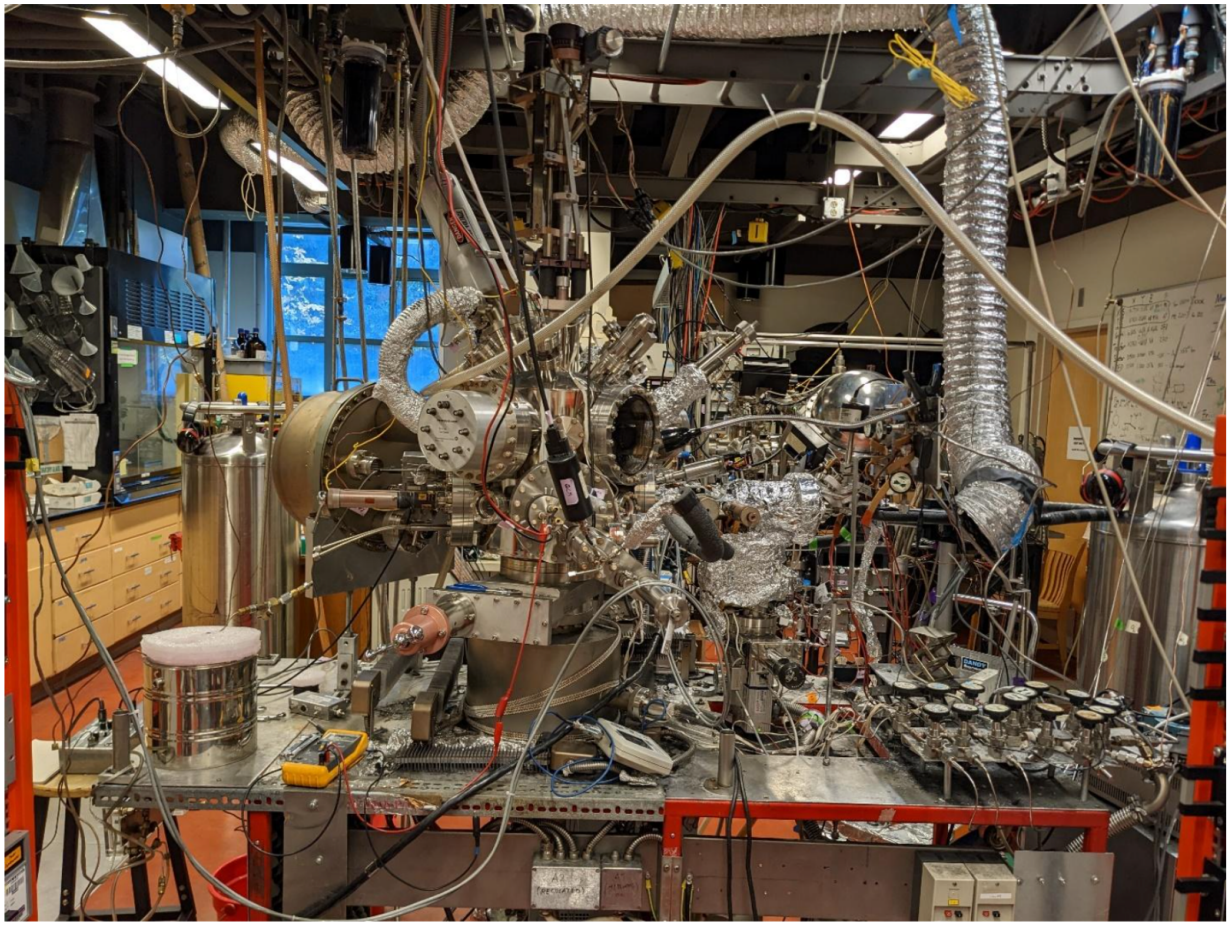

Figure 6.1. A photograph of the small molecule single-crystal adsorption calorimeter is shown. There is a single main chamber, with the sample manipulator located on top. The molecular beam is located to the right of the chamber. Instrumentation for sample preparation and characterization is located around the top region of the chamber, and the calorimetry equipment is in the lower region of the chamber. The titanium sublimation pump can be seen below the main chamber at table level. The main turbo pump is located under the titanium sublimation pump, under the table (not visible).

Chapter 7. Improving Our Understanding of Kinetics Using Degree of Rate Control Analyses: Relationship to Volcano Plots and Experimental Measurements

Overview

The degree of rate control (DRC)[202,203] is a mathematical approach that quantifies the extent to which any given species in a multistep reaction affects the net reaction rate to the product of interest. The DRC is especially valuable for understanding complex catalytic reaction mechanisms with many steps because it clarifies which species' energetics are most important in determining the rate. The DRC has been connected to several other reaction quantities and is a powerful tool for studying reaction mechanisms and screening catalysts. Although the DRC has become a popular tool, it is important to clarify and explain its connections to reaction kinetics so that scientists may understand and fully exploit the power of this tool. This chapter gives a brief overview of two in-progress projects related to this mission: thee first explores the relationship between volcano plots and DRC, and the second explores how experimental measurements can be used to determine DRCs to gain a deeper understanding of reaction mechanisms.

7.1 Degree of Rate Control Analysis of Volcano Plots for Improving Catalyst Design

7.1.1 Introduction

Volcano plots are frequently encountered in the fields of heterogenous catalysis and electrocatalysis because they link specific catalyst properties to the effectiveness of a catalyst for a given reaction. Volcano plots illustrate Sabatier's principle, which predicts that optimal catalysts must be able to bind to reaction intermediates, but not so strongly that it limits the turnover frequency of the reaction.[204,205] Descriptor values, such as the binding energy of the catalyst to some relevant reaction intermediate, plotted against some indicator of catalytic activity (e.g. turnover frequency) identify an optimal range of target descriptor values for new materials that may result in better catalytic performance (activity, selectivity, sinter resistance, etc.). These plots are often based on scaling relations, which, for multistep reactions, mathematically relate the energy of one intermediate or transition state to all other intermediates and transition states involved in the reaction. Linear scaling relations typically hold true across a range of catalysts, and they are often expressed in the form of volcano plots to show the potential efficacy of catalysts in different regions of descriptor space (i.e., materials space). Scaling relations and volcano plots are particularly valuable for analyzing multistep reactions because they simplify the system so that they are easier to understand and optimize.

Another tool that has proven particularly valuable for understanding complex multistep catalytic reactions is degree of rate control (DRC) analysis.[202] The DRC of any intermediate or transition state quantifies the extent to which the standard state free energy of that species affects the net reaction rate of forming a product or consuming a reactant of interest. The DRC, X_i, for

any species, i, in a reaction is defined using the partial derivate of the relative (or natural log of the) reaction rate, r, in forming a product of interest with respect to the standard-state Gibbs free energy (G^0) of that species, holding constant the standard-state Gibbs free energies of all other species (over RT):[206]

$$X_i = \left[\frac{\partial \ln(r)}{\partial \left(-\frac{G_i^o}{RT} \right)} \right]_{G_{j \neq i}^0} \tag{7.1}$$

R is the universal gas constant and T is the temperature. Although the DRC may be calculated for every intermediate and transition state, there are usually no more than a few species that are kinetically relevant, even for reaction mechanisms with many steps. Most species have a DRC close to zero, meaning that their exact energies are not kinetically relevant.

Degree of rate control values have simple mathematical relationships with important kinetic parameters of the reaction, such as apparent activation energy,[207] kinetic isotope effect,[208] and reaction orders.[209] These quantitative relationships can help scientists simplify and understand complex multistep catalytic reactions, which allows for mechanism discovery, efficient catalyst screening and optimization.[210] Connections between DRC and reaction properties can aid in studying reactions, quantifying reaction properties, and optimizing reactions. In this work, we explain the relationship between volcano plots and DRC and show how DRC behaves in different regions of volcano plots. We also explain how this connection between volcano plots and DRC can be used to better understand reaction kinetics and find optimal catalysts.

7.1.2 Methods

For mathematical insight into the relationship between DRC and volcano plots, consider the following derivation. Assuming that the free energy of a reaction is dominated by the enthalpy here (since standard-state entropies of these species vary little from catalyst material to material), H, then the natural log of the rate, r, is simply a function of the enthalpy of the species' involved in the reaction:

$$\ln(r) = f(H_i). \tag{7.2}$$

Species i here includes all intermediates and transition states involved in the reaction. Linear scaling correlations[211,212] relate species enthalpy, H_i, to a chosen descriptor enthalpy, H_j, using a linear scaling coefficient α_{ij}. The enthalpy of any species i can be calculated from a linear scaling coefficient, α_{ij}, and a few corresponding descriptor enthalpies, H_j:

$$H_i = \sum_j (\alpha_{ij} H_j). \tag{7.3}$$

These descriptor enthalpies are typically simple quantities such as the bond enthalpy of the surface site to a atom (C, O and N atom) or simple diatomic (like -OH). The rate of reaction can be related to the descriptor value by taking the derivative of the reaction rate (Equation 7.2) with respect to the descriptor enthalpy. If the free energies of the species are dominated by their enthalpy, the differential change in rate with respect to the differential change in species enthalpy is equal to the degree of rate control for species i, as shown in Equation 7.1. The partial derivative of the species enthalpy with respect to descriptor enthalpy is the value of the linear scaling coefficient α_{ij}. The partial derivative of the reaction rate with respect to descriptor enthalpy is then equal to the sum of the products of the DRCs for the involved species and their linear scaling coefficients, as shown:

$$\frac{\partial \ln(r)}{\partial\left(-\frac{H_j}{RT}\right)} = \sum_i \frac{\partial \ln(r)}{\partial\left(-\frac{H_i}{RT}\right)} \frac{\partial\left(-\frac{H_i}{RT}\right)}{\partial\left(-\frac{H_j}{RT}\right)} = \sum_i X_i \alpha_{ij} \tag{7.4}$$

There are rarely more than a few kinetically relevant species with non-negligible DRC values,[209] so, even for complex reactions, the sum in Equation 7.4 usually only consists of no more than a few kinetically relevant terms. Equation 7.4 directly relates the rate of reaction, which are shown in volcano plots, to the DRC of the species involved in the reaction and the linear scaling relations used to build the volcano-type relationship.

To demonstrate the relationships above, we use the methane steam reforming microkinetic model detailed by Xu et al.[213], which was also previously used by Wolcott et al.[210] to demonstrate how DRC may be used for computational catalyst screening. The turnover frequency is calculated using microkinetic modeling in CatMAP,[214] using DFT-based parameters from studies that have previously modeled methane steam reforming.[210,213] Xu et al.[213] also report the DFT energies of all transition states and intermediates for their mechanistic model of methane steam reforming reaction on metal surfaces. They also report the vibrational frequences and vibrational partition function for the species on Rh(211), which are used to calculate the heat capacities and entropic corrections to the standard-state free energies of species using the harmonic oscillator approximation, which are assumed to be the same for all metals. The Shomate equation[215] is used to calculate entropy and heat capacity contributions to the energies of gas-phase molecules. The accuracy of the DFT-derived energies in this model is not important to the conclusions that are demonstrated in this paper. The intention is to show the relationship between DRC and volcano-style plots to demonstrate the power of the DRC for understanding complex reactions and designing catalysts more efficiently.

7.1.3 Results and Discussion

Figure 7.1a shows a 2-descriptor volcano plot where carbon binding energy and oxygen binding energy of transition metals are used as descriptors and the turnover frequency (TOF) for methane steam reforming is the indicator of catalytic activity for the metal catalysts. Figure 7.1b maps the degree of rate control of high-coverage (i.e. rate-controlling) intermediates within the descriptor space where E_{C*} is between 0 and 6 eV and E_{O*} is between -2 to 3 eV. Note that the ridges of the volcano align with the boundary regions in the DRC map, which suggests that top catalysts are likely located in those boundary regions.

The relationship between DRC and catalyst activity can be understood by considering Equation 4 with the volcano plot in Figure 7.1a. Figure 7.2 shows a plot of the dotted line in Figure 7.1a, in order to demonstrate how the changes in DRC relate to changes in the TOF. Moving from point A to point B in Figure 1, the carbon binding energy, E_{C*}, is constant and, initially, the logarithm of the rate is linearly related to the oxygen binding energy, E_{O*}. Assuming linear scaling correlations hold for all regions of interest, both the DRC values, X_i, and the linear scaling coefficients, α_{ij}, are constant within the linear region between points A and B; therefore, the partial derivative in Equation 7.4 is a constant, satisfying the linear relationship observed between ln(TOF) and the descriptor enthalpy, which is E_{O*} in this case. The constant nature of the DRC values in this region may also be observed in Figure 7.1b, which maps the DRC for intermediates in the same descriptor space as the volcano plot (-2 eV< E_{O*} < 3 eV; 0 eV < E_{C*} < 6 eV). Point B is located on the ridge of the volcano and the maximum turnover frequency, when E_{c*} is constrained to 3.5 eV. As point B is approached, the linear relationship is broken and the derivative of the rate with respect to the descriptor value is no longer constant. Because we assume that linear scaling correlations hold in the region of interest, a change in the DRC values must be responsible

for the change in slope near the ridge. The ridge of the volcano is located where the changing DRC values result in a sign reversal of the partial derivative in Equation 4. Once the peak of the ridge (point B) is surpassed, there is an approximately linear decrease in the log(TOF) as E_{O*} continues to increase. This proves a key point: *optimal catalysts must be located in the region where the DRC changes*, because, otherwise, the partial derivative in Equation 7.4 can only be an approximately constant positive or negative value. This is also apparent by the fact that the rate must decrease as one moves away from the ridge/peak of the volcano.

Because of the nature of the ridge/peak regions, we can conclude that optimal catalysts are located where there is a rapid change in the rate-limiting step or the partial coverage of intermediate species. This also corresponds to a change in the reaction order and DRC values. The regions on the volcano plot where the rate-limiting step and the reaction order are stable as you move across descriptor space are not optimal regions for catalyst exploration (but are in regions where it is easiest to predict *better* materials).

Cross-sections of Figure 7.1b are plotted in Figure 7.3 and show the coverage, which is equal to the degree of rate control, for each of the three high-coverage intermediates, C^*, CO^*, and O*, when E_{C*} and E_{O*} are constant. In Figure 7.1b, in most regions, the DRC is constant; the DRC only changes in boundary regions that correspond with the ridges of the volcano plot in Figure 7.1. Optimal catalysts must be in regions where the DRC values and coverages of intermediates are changing. Figure 7.1b further demonstrates that boundaries between regions where different intermediate species dominate the reaction are very narrow and are on the order of 0.1 eV (~10 kJ/mol) wide.

Figure 7.3 shows two examples of the DRC as a function of one descriptor when the other descriptor is constant, which illustrates that DRC changes rapidly in the regions where it is

not constant. The boundaries are narrow because DRC values are only energetically sensitive when two species are in close competition to be rate-controlling. In regions where two species are in close competition, a small change in the energetics of an adsorbed species (or transition state) can cause a significant change in the DRC values and rate determining step. The most interesting material space for catalyst exploration may be narrowed down in descriptor space because DRC values are generally constant (and thus improvement is easiest to predict), except in narrow boundary regions, which also correspond to ridges of the volcano, where TOF is highest.

7.2 Studying Reaction Kinetics by Using Experimental Measurements to Determine Degrees of Rate Control

7.2.1 Introduction

Advances in computational chemistry methods, and particularly developments in DFT calculations, have improved the cost, accuracy, and popularity of generating relatively accurate reaction energy diagrams for multi-step catalytic reaction mechanisms.[203,206,210,213,216,217] Microkinetic models specify the elementary steps that are required for a multi-step catalytic reaction, and include energetic information for all intermediates and transition states. Despite recent progress, DFT-calculated microkinetic models for catalytic reactions involving many steps still result in somewhat inaccurate energies of transition states and adsorbed intermediates,[182] and more accurate levels of theory remain computationally too expensive. Developing tools for accurately understanding the kinetics of multi-step reactions without losing information through oversimplification, and without expensive computations, is an essential effort for progressing

catalysis research. Degree of rate control analysis is one such tool, which has been performed on microkinetic models and has proven valuable for understanding multi-step catalytic reaction kinetics, as well as for improving microkinetic modelling methods, improving the energies of species with high DRCs (relative to initial DFT-based estimates) and developing simplifications that still accurately capture reaction kinetics.[203,208,209]

The generalized degree of rate control, X_i, for a species, i, is defined as the relative change in the net rate to the product of interest (or to consume a reactant), r, from a differential change in the species' standard-state free energy, G^0:[203]

$$X_i = \left(\frac{-\partial \ln r}{\partial\left(\frac{G_i^0}{RT}\right)} \right)_{G_{j\neq i}^0} , \tag{7.5}$$

where R and T are, respectively, the universal gas constant and the temperature. The derivative is taken holding constant the standard-state free energies for all other species. We can use DRC values to calculate other observables. The apparent reaction order, δ_i, of fluid phase reaction intermediate, i, is simply the negative of its DRC:[218]

$$\delta_i = -X_i . \tag{7.6}$$

For a fluid-phase reactant, j, the apparent reaction order equals the negative sum of the products between the stoichiometric coefficients, $\upsilon_{j,i}$, of reactant, j, in forming of species, i, and the DRC of the species *i*:[218]

$$\delta_j = -\sum_i \left(\upsilon_{j,i} X_i\right) \tag{7.7}$$

The DRC of a catalyst-bound reaction intermediate, n, can be calculated as the product of its coverage, θ_n , and a proportionality constant, σ:[219]

$$X_n = -\sigma\theta_n \tag{7.8}$$

where σ is a weighted average of step site requirements, defined as the negative sum of the products between the DRC of transition state, i, and the number of catalyst sites, n_i, required for step i:[219]

$$\sigma = -\sum_i (X_i n_i)\,. \tag{7.9}$$

Apparent activation energy is the weighted sum of the standard-state enthalpies of all species (H_i^0) weighted by their DRCs:[207]

$$E_{app} = RT + \sum_i (X_i H_i^0), \tag{7.10}$$

where R and T are the universal gas constant and temperature, respectively.

Typically, these equations are applied by calculating the degrees of rate control via a fully developed microkinetic model and then using DRC values to solve for expected values. If the equations are considered in a reverse manner, the experimentally observed values could offer insight into the kinetics of a reaction of interest. In this work, we show how experimental information may be used to extract information on the DRCs and reaction energetics of a multistep catalytic reaction of interest.

7.2.2 Results and Discussion

Three cases are considered to clarify the relationship between reaction kinetics and solvability of these equations if certain experimentally observed values are known. Note that, even for complex reaction schemes, only a limited number of steps are rate-limiting, and previous work has shown that a generalized two-step reaction scheme very often may be used to simplify and understand most steady-state heterogeneously catalyzed reactions.[182,217]

Case 1

In the first case, we assume that a reaction of interest where this 2-step approximation is valid, so that it has only one high-coverage intermediate, and one transition state with a high DRC. We also assume that the reaction of interest has two reactants. This gives us two equations for the apparent reaction orders:

$$\delta_{R1} = -\left[\upsilon_{R1,I} X_I + \upsilon_{R1,TS} X_{TS}\right] \tag{7.11}$$

$$\delta_{R2} = -\left[\upsilon_{R2,I} X_I + \upsilon_{R2,TS} X_{TS}\right], \tag{7.12}$$

where R1 and R2 are reactants 1 and 2, TS is the rate-determining transition state, and I is the high-coverage intermediate. An additional equation may be written if coverage of this most abundant surface intermediate is known:

$$X_I = X_{TS} n_{TS} \theta_I, \tag{7.13}$$

where θ_I is the fractional coverage of the intermediate. If the apparent activation energy is also measured at the same conditions as the coverage and apparent reaction orders, it may be expressed in terms of DRCs:

$$E_{app} = RT + X_I H_I^0 + X_{TS} H_{TS}^0 . \tag{7.14}$$

Combining equations (7.7) (twice, one for each reactant) and (7.8), the degrees of rate control may be calculated directly from these three measured linetic parameters, and the number of sites required for the step involving the most rate-controlling transition state may also be extracted. The apparent activation energy has two additional unknowns: the standard-state enthalpies of the intermediate and transition state. The standard-state enthalpy of the intermediate may be measured (and often has been measured already) or calculated theoretically, in which case the standard-state enthalpy of the key transition state may be extracted. See Table 7.1 for details of the equations and solvability of this Case 1.

Case 2

The next case to consider is one in which we assume that a reaction has one high-coverage intermediate and two transition states with high DRC values. See Case 2 in Table 7.2 below for details of the equations and solvability of this case. By adding a second rate-controlling transition state, the number of apparent reaction order and coverage equations does not change; therefore, to solve for the DRCs of the intermediate and transition states, the number of catalyst sites required must be assumed for the two steps in which the transition states are involved. Because the number of transition states required for elementary may be assumed if some reaction mechanism is assumed, the DRCs of the three species of interest may be extracted based on apparent reaction order and coverage data alone. Even if the apparent activation energy is measured and the standard-state enthalpy of the intermediate is known, the standard-state enthalpies of the two transition states cannot be calculated with the single apparent activation energy equation. To solve for the transition state standard-state enthalpies, a second equation may be generated by measuring the apparent activation energy at a different temperature, where the apparent activation energy differs from the original equation. Figure 7.4 shows that, based on the Arrhenius equation, the apparent activation energy changes rapidly as a function of temperature in some regions; although, note that some temperature ranges have a nearly constant apparent activation energy. By choosing to measure the apparent activation energy at two different temperature regimes, two activation energy equations may be generated, and the standard-state enthalpies of the transition states may be extracted. Note that at different temperatures, the degrees of rate control will change, but recall that they can be determined independently using coverage and apparent reaction order data.

Case 3

In the last case, the complexity is increased by adding a second high-coverage intermediate, so that we assume a reaction of interest has two high-coverage intermediates and two transition states with high DRCs. See Case 3 in Table 7.3 for details of the equations and solvability of this case. The DRCs for all four species may be extracted based solely on apparent reaction order and coverage data. To extract standard-state enthalpies of all four species, the apparent activation energy must be measured in at least two different temperature regimes. The extracted DRC and standard-state enthalpy values offer insights into the reaction kinetics, without a large computational or experimental cost. In some cases, these experimental values may already be known or measured for a reaction, and it may be valuable to demonstrate to experimentalists how to use their data to gain deeper-level kinetic understanding about their reactions of interest.

7.3. Figures

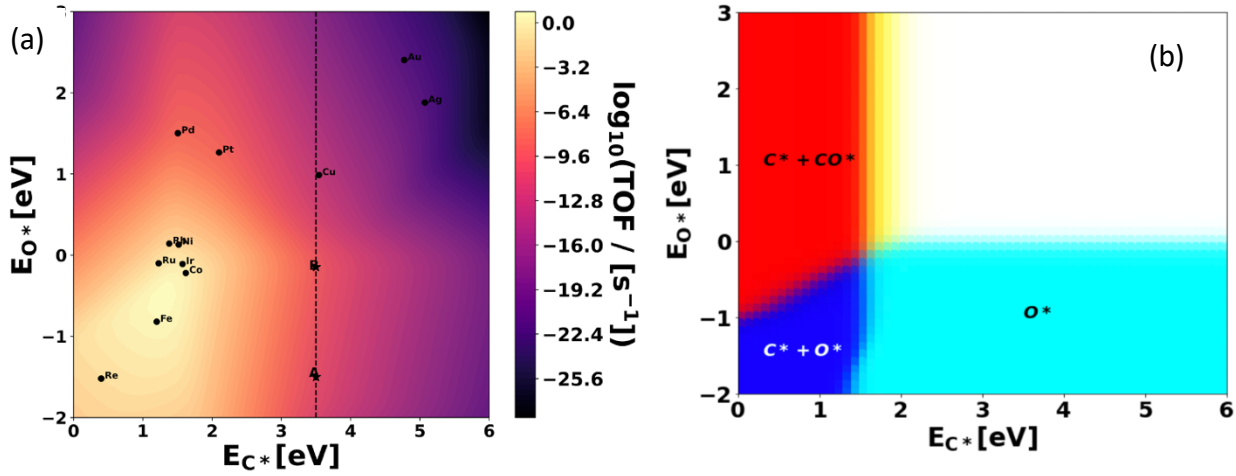

Figure 7.1. (a) A 2-descriptor volcano plot of the methane steam reforming reaction rate per surface site (TOF in s^{-1}),[210] with the specific locations of transition metal catalysts within this "materials space" marked. The dotted line indicates the location of the plot shown in Figure 7.2. (b) DRC map for high-coverage intermediates in methane steam reforming,[210] plotted in the same descriptor space as the volcano plot in part (a). The color at each point is weighted by degrees of rate control for intermediates C^*, CO^*, and O*.

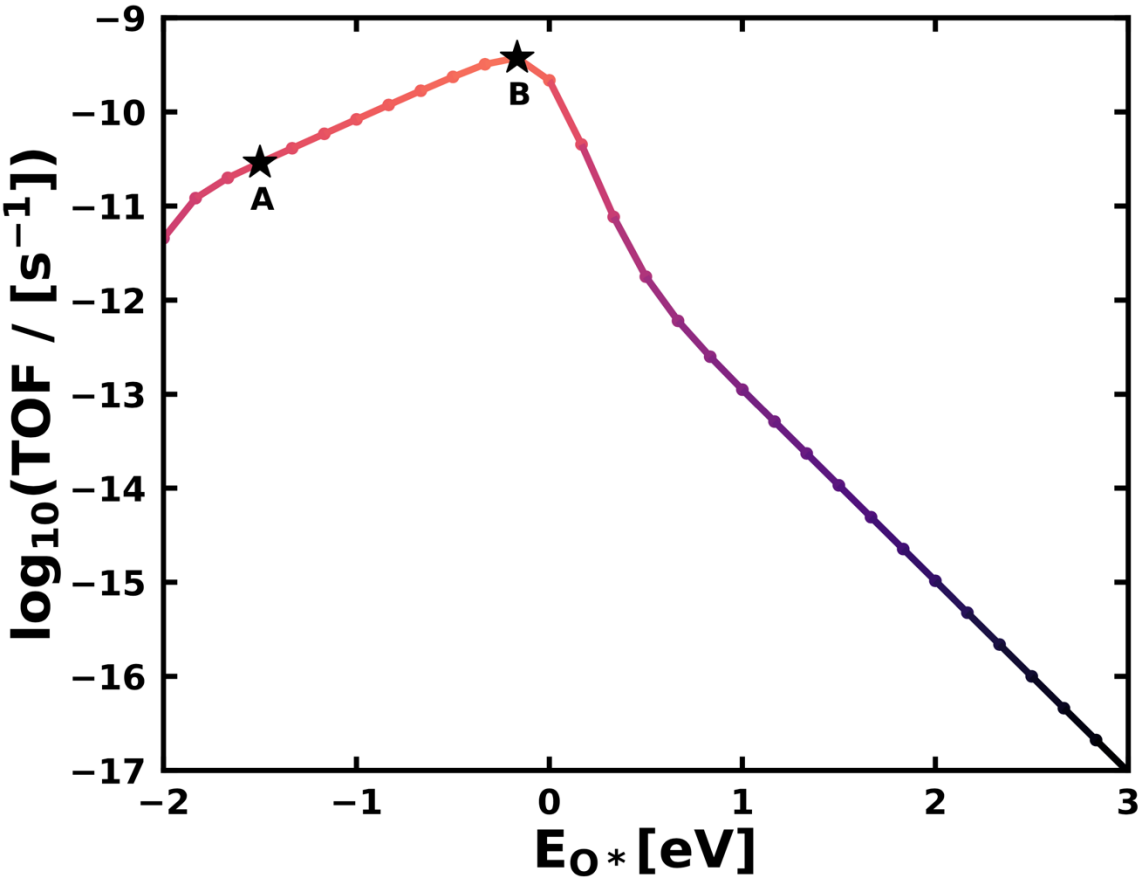

Figure 7.2. A 2D representation of the volcano plot for E_{c*} = 3.5 eV. Points A and B are marked for demonstrative purposes that are described in the text. See Figure 7.1 to see the location of this line on the volcano plot.

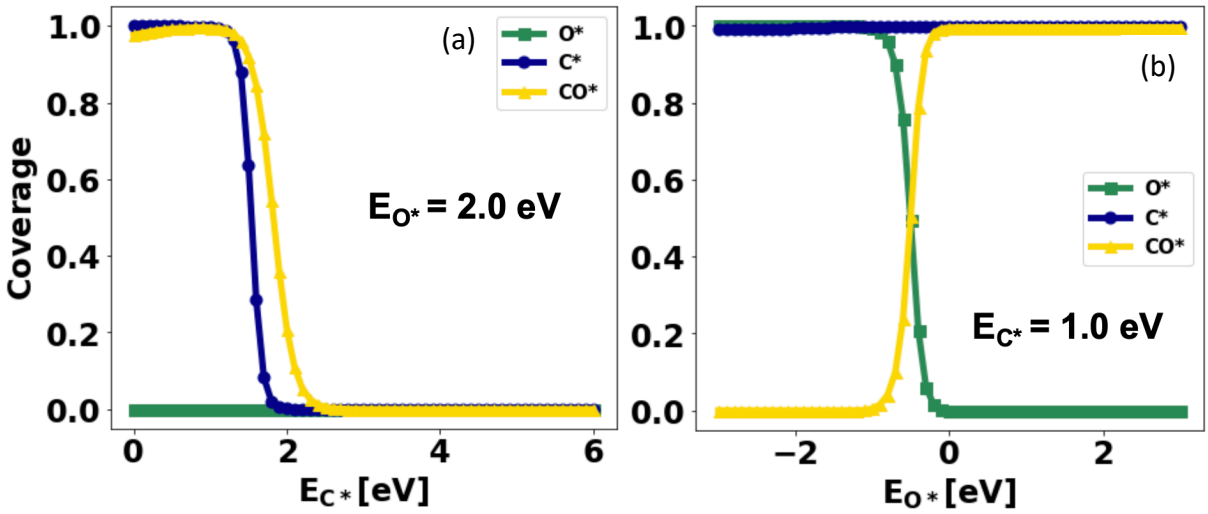

Figure 7.3. Coverage of intermediates versus one single descriptor. Plot (a) shows where E_{O*} = 2.0 eV in Figure 7.1b and plot (b) shows where E_{C*} = 1.0 eV in Figure 7.1b. Note that C* occupies different sites that CO* and O*, so that the sum of CO* and O* coverages may be as large as 1 no matter how high is the C* coverage.

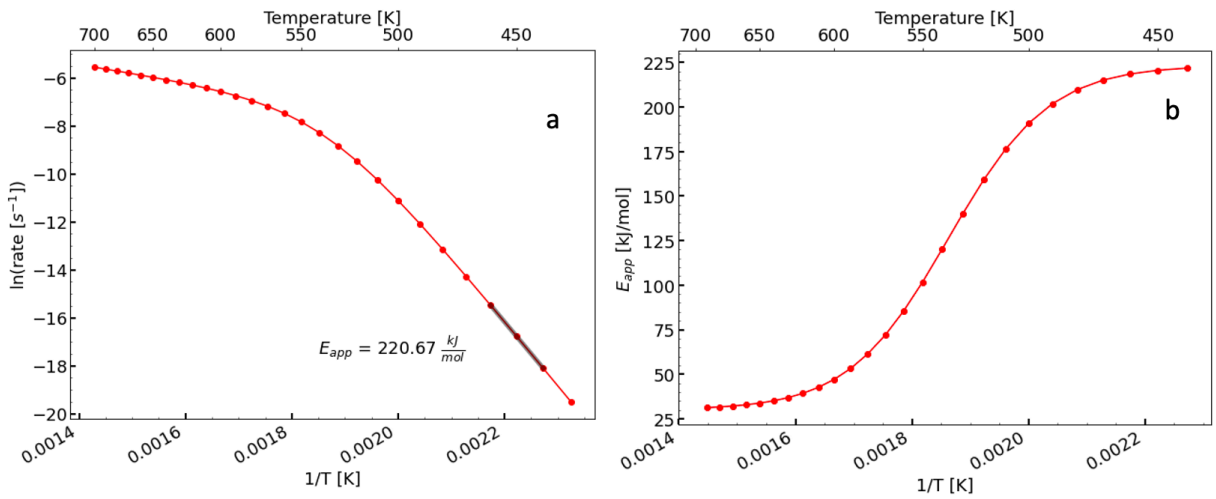

Figure 7.4. (a) Arrhenius plot for CO_2 hydrogenation on Cu(211) at 30 bar from 400 to 700 K. The apparent activation energy at 450K is shown as well as the line of best fit that was used to solve for the slope and apparent activation energy. (b) Plot of the activation energy versus 1/T for the same temperature range as shown in (a).

7.4 Tables

Table 7. 1. Case 1: One high-coverage intermediate and one transition state with high DRC

Intermediate = I; Transition state = TS; Reactants 1 and 2 = R1, R2

Reaction orders

$$\delta_{R1} = -\left[\upsilon_{R1,I} X_I + \upsilon_{R1,TS} X_{TS}\right]$$
$$\delta_{R2} = -\left[\upsilon_{R2,I} X_I + \upsilon_{R2,TS} X_{TS}\right]$$

Coverage

$$\sigma = -X_{TS} n_{TS} \rightarrow X_I = -\sigma\theta_I$$
$$X_I = X_{TS} n_{TS} \theta_I$$

Apparent Activation Energy

$$E_{app} = RT + X_I H_I^0 + X_{TS} H_{TS}^0$$

Case	Known / Measured Kinetic Parameters	Unknowns	Number of Equations	Solvability
Considering only reaction order and coverage equation	δ_{R1}, δ_{R2} $\upsilon_{R,j}$ x 4 θ_I	X_I, X_{TS} n_{TS}	3	Well-defined (Assuming 2 reactants; e.g. if 1 reactant, system is underdefined but can solve for DRCs if n_{TS} is known)
Including apparent activation energy	δ_{R1}, δ_{R2} $\upsilon_{R,j}$ x 4 θ_I E_{app}	X_I, X_{TS} n_{TS} H_I^0, H_{TS}^0	4	Underdefined, but given H_I^0,can solve for H_{TS}^0 OR use two E_{app} equations i.e. at two temps like last calc in Case 2 above

Table 7.2. Case 2: One high-coverage intermediate and two transition states with high DRC

Intermediate = I; Transition states = TS1, TS2; Reactants = R1, R2

Reaction order

$$\delta_{R1} = -\left[\upsilon_{R1,I} X_I + \upsilon_{R1,TS1} X_{TS1} + \upsilon_{R1,TS2} X_{TS2}\right]$$
$$\delta_{R2} = -\left[\upsilon_{R2,I} X_I + \upsilon_{R2,TS1} X_{TS1} + \upsilon_{R2,TS2} X_{TS2}\right]$$

Coverage

$$\sigma = -[X_{TS1} n_{TS1} + X_{TS2} n_{TS2}] \rightarrow X_I = -\sigma\theta_I$$

$$X_I = [X_{TS1} n_{TS1} + X_{TS2} n_{TS2}]\theta_I$$

Apparent Activation Energy

$$E_{app} = RT + X_I H_I^0 + X_{TS1} H_{TS1}^0 + X_{TS2} H_{TS2}^0$$

Case	Known / Measured	Unknown	Number of Equations	Solvability
Considering only reaction order and coverage equation	δ_{R1}, δ_{R2} $\upsilon_{R,j}$ x 6 θ_I	X_I, X_{TS1}, X_{TS2} n_{TS1}, n_{TS2}	3	Underdefined if n_{TS}'s not known; well-defined if given n_{TS}'s
Including apparent activation energy	δ_{R1}, δ_{R2} $\upsilon_{R,j}$ x 6 θ_I E_{app}	X_I, X_{TS1}, X_{TS2} n_{TS1}, n_{TS2} H_I^0, H_{TS1}^0 , H_{TS2}^0	4	Underdefined: even if given H_I^0,can't solve for H_{TS}^0's – may generate two E_{app} equations and use those to solve

Table 7.3. Case 3: Two high coverage intermediates and two transition states with high DRC.

Intermediates = I1, I2; Transition states = TS1, TS2 ; Reactants = R1, R2

Reaction order

$$\delta_{R1} = -\left[\upsilon_{R1,I1} X_{I1} + \upsilon_{R1,I2} X_{I2} + \upsilon_{R1,TS1} X_{TS1} + \upsilon_{R1,TS2} X_{TS2}\right]$$
$$\delta_{R2} = -\left[\upsilon_{R2,I1} X_{I1} + \upsilon_{R2,I2} X_{I2} + \upsilon_{R2,TS1} X_{TS1} + \upsilon_{R2,TS2} X_{TS2}\right]$$

Coverage

$$\sigma = -[X_{TS1} n_{TS1} + X_{TS2} n_{TS2}] \rightarrow X_I = -\sigma\theta_I$$

$$X_{I1} = [X_{TS1} n_{TS1} + X_{TS2} n_{TS2}]\theta_{I1}$$
$$X_{I2} = [X_{TS1} n_{TS1} + X_{TS2} n_{TS2}]\theta_{I2}$$

Apparent Activation Energy

$$E_{app} = RT + X_{I1} H^0_{I1} + X_{I2} H^0_{I2} + X_{TS1} H^0_{TS1} + X_{TS2} H^0_{TS2}$$

Case	Known / Measured	Unknown	Number of Equations	Solvability
Considering only reaction order and coverage equation	δ_{R1}, δ_{R2} $\upsilon_{R,j}$ x 8 θ_{I1} , θ_{I2}	X_{I1}, X_{I2} , X_{TS1}, X_{TS2} n_{TS1}, n_{TS2}	4	Underdefined if n_{TS}'s not known; well-defined if given n_{TS}'s
Including apparent activation energy	δ_{R1}, δ_{R2} $\upsilon_{R,j}$ x 8 θ_I E_{app}	X_{I1}, X_{I2} , X_{TS1}, X_{TS2} n_{TS1}, n_{TS2} H^0_{I1}, H^0_{I2}, H^0_{TS1} , H^0_{TS2}	5	Underdefined: If given H^0_I's, can solve for H^0_{TS}'s given two E_{app} equations (need 4 if H^0_I's not known)

Chapter 8. Conclusions and Future Outlook

The work presented above is motivated by the hugely important role that heterogeneous catalysts play in nearly all important chemical production processes, in enabling more environmentally-friendly chemical and energy technologies, and in combatting and mitigating the effects of unsustainable processes. The work presented above focuses on understanding the fundamental energetics of metal nanoparticles supported on oxide and carbon materials in order to enable catalyst design in two ways: (1) Measurements of model catalyst energetics in UHV serve as benchmarks for DFT calculations, in an effort to improve their accuracy in calculating theoretical energies so that they can be used and trusted for fast computational catalysis research and screening. (2) Measured adhesion energies for different metal / support system combinations can be used to predict adhesion energies (and therefore chemical potential versus size) of metal / support systems, which is a tool for tuning catalyst structure to improve its properties and performance behavior, to increase the efficiency of catalyst screening and research.

In Chapter 3, the energetics and nanoparticle growth of Pd / graphene / Ni(111) are investigated using SCAC and He^+ LEIS, respectively. Based on the measured heats of adsorption and particle sizes, the chemical potential of the nanoparticles as a function of size is calculated and reported. From the chemical potential versus size, the adhesion energy of Pd to graphene / Ni(111) is calculated to be 3.5 J/m^2 using the HCM. This adhesion energy was later updated to 2.51 J/m^2 using the SCM, and the Pd particles were calculated to have a contact angle of 73°.[38] The adhesion energy is compared to that of Ag and Ni on graphene / Ni(111), which had previously been measured using the same experimental methods. A linear trend is observed between the adhesion energy of late transition metals to graphene / Ni(111) and the carbophilicity of the metals, which can be estimated using DFT calculations. This trend allows

adhesion energies to be predicted for other late transition metals on graphene / Ni(111), which is an exciting step in the direction of predicting adhesion energies and catalyst behavior for metal nanoparticles on more carbon-based supports. As discussed above, because the graphene is only a single atom thick, the underlying Ni atoms are likely able to interact with the metal nanoparticles on the surface of the graphene (in this case, Pd), and affect the resulting adsorption and adhesion energies. Because of this, it would be particularly important and interesting to use the methods that are described in this work to study metal adhesion energies on graphite, to eliminate the effect of the underlying metal support, which would likely cause the adhesion energies to be lower than those observed on graphene / Ni(111).

Chapter 4 investigates the energetics of Cu / rutile-TiO_2(100). As in Chapter 3, the heats of adsorption and particle growth morphology is shown and used to determine the chemical potential versus size of Cu nanoparticles on this support. In this case, the adhesion energy is calculated to be 3.57 J/m^2 with the HCM, then the results of the HCM are used to determine the SCM fit to the data, which results in an updated adhesion energy of 2.50 J/m^2 with a contact angle of 67°. The procedure applied equations that had recently been published calculate the SCM from the HCM, and showed that this method, which is much simpler than determining the full SCM fit, can be used to accurately determine the best SCM fit parameters. Comparing the final adhesion energy with the previous measurements of Ag / rutile-TiO_2 shows that the adhesion energy tends to scale linearly with the oxophilicity of the metal, which is consistent with previous trends that have been observed on oxide surfaces.

In Chapter 5, the proportionality constant for this rutile-TiO_2(100) trend is reported, and shown alongside the previously-reported proportionalities on MgO(100) and CeO_2(111). These three trends can be used to predict the adhesion energies of late transition metals on these three

surfaces based only on the oxophilicity of the metal but cannot predict adhesion energies across different oxide supports. To predict adhesion energies across oxide supports, the slope of the adhesion energy versus oxophilicity proportionalities for the three oxides are correlated to two descriptors: (1) the heat of the reduction of the oxide to its next lower oxidation state, and (2) the oxygen vacancy formation energy. Both descriptors exhibit a linear correlation with the slope of the adhesion energy vs. oxophilicity proportionality. Unlike the heat of reduction, the oxygen vacancy formation energy is surface specific, so it is the preferred descriptor, but it depends on having a reliable DFT calculation. For surfaces that do not yet have reliable or reported oxygen vacancy formation energies, the heat of reduction value may be used to estimate the oxygen vacancy formation energy, because, as shown in Chapter 5, the differences in the oxygen vacancy formation energies for different surfaces of the same oxide is much smaller than the differences in the heat of reduction values for different oxides. Based on the observed correlations, the adhesion energies of six different metals on six different oxide surfaces are scaled to a single trendline, which finally allows the adhesion energies of metals to be predicted across oxide surfaces. To estimate the adhesion energy of any given late transition metal on any given oxide, the only descriptors required are the oxophilicity of the metal (reported in ref.[38]) and the oxygen vacancy formation energy or heat of reduction of the oxide to its next lower oxidation state.

The measurements reported above are excellent benchmarks for theoreticians because they are performed on systems that are clean and ordered and, therefore, simplest to model theoretically. Heterogeneous catalyst systems are still difficult to model accurately using DFT, and theoreticians rely on benchmark data like those reported in Chapters 3 and 4 to improve and verify their methods. Experimentation alone is not fast and efficient enough to keep up with the

growing demand and growing standards required of catalysts, so improving theoretical techniques is an important effort that could drastically decrease the time required to find the best catalysts for any given application. In the meantime, the trends reported in Chapters 3 and 5 can give an estimate of the adhesion energies of metals on oxides and graphene / Ni(111), which can in turn be used to estimate the chemical potential of these systems, which predicts properties such as sintering resistance and activity. The trends can be used to tune catalyst properties by tuning their composition and can also be used to screen for catalysts that might have promising properties for a given application. Due to the complex nature of heterogenous catalysts and the reactions that occur on them, a multidisciplinary approach is essential for making the best possible progress, and the work presented here is meant to be a building block in the research effort enabling more and better catalysts for critically important applications.

Chapter 6 describes the efforts to continue the important work of a unique small molecule single-crystal adsorption calorimeter. In Chapter 7, it is shown that degree of rate control analyses are very powerful tools for catalysis research, especially in understanding how kinetics are affected by the energetics of key species.

Chapter 9. Bibliography

1. Hu, X. & Yip, A. C. K. Heterogeneous Catalysis: Enabling a Sustainable Future. *Frontiers in Catalysis* **1**, (2021).
2. Hagen, J. *Industrial Catalysis: A Practical Approach*. (John Wiley & Sons, Incorporated, Berlin, 2015).
3. Friend, C. M. & Xu, B. Heterogeneous Catalysis: A Central Science for a Sustainable Future. *Acc Chem Res* **50**, 517–521 (2017).
4. Schlögl, R. Heterogeneous Catalysis. *Angewandte Chemie* **54**, 3465–3520 (2015).
5. Fechete, I., Wang, Y. & Védrine, J. C. The past , present and future of heterogeneous catalysis. *Catal Today* **189**, 2–27 (2012).
6. Bortolozzi, J. P., Banús, E. D. & Miró, E. Catalysts for Air Pollution Control: Present and Future. *Catalysts* **13**, (2023).
7. Yentekakis, I. V & Dong, F. Grand Challenges for Catalytic Remediation in Environmental and Energy Applications Toward a Cleaner and Sustainable Future. *Frontiers in Environmental Chemistry* **1**, 1–14 (2020).
8. F. J. J. G. Janssen, R. A. van S. *Catalytic Science Series: Volume 1, Environmental Catalysis*. (Imperial College Press, 1999).
9. Przegl, Ś. R. & Pów, Ą. D. P. Ę. Major advances and challenges in heterogeneous catalysis for environmental applications: a review. *Ecol. Chem. Eng.* **25**, 9–34 (2018).
10. Leach, B. E. *Applied Industrial Catalysis* . (Academic Press, New York, 1983).
11. Armor, J. N. A history of industrial catalysis. *Catal Today* **163**, 3–9 (2011).
12. Chen, B. W. J., Xu, L. & Mavrikakis, M. Computational Methods in Heterogeneous Catalysis. *Chem Rev* **121**, 1007–1048 (2021).
13. Goodman, D. W. Model Catalysts: From Extended Single Crystals to Supported Particles. *Surface Review and Letters* **2**, (1995).
14. Gao, F. & Goodman, D. W. Model Catalysts : Simulating the Complexities of Heterogeneous Catalysts. doi:10.1146/annurev-physchem-032511-143722.
15. Zhang, J. & Medlin, J. W. Catalyst design using an inverse strategy : From mechanistic studies on inverted model catalysts to applications of oxide-coated metal nanoparticles. *Surf Sci Rep* **73**, 117–152 (2018).
16. Plessow, P. N. & Campbell, C. T. Influence of Adhesion on the Chemical Potential of Supported Nanoparticles as Modeled with Spherical Caps. *ACS Catal* 2302–2308 (2022) doi:10.1021/acscatal.1c04633.
17. Campbell, C. T. & Mao, Z. Chemical Potential of Metal Atoms in Supported Nanoparticles: Dependence upon Particle Size and Support. *ACS Catal* **7**, 8460–8466 (2017).
18. Mao, Z. & Campbell, C. T. Predicting a Key Catalyst-Performance Descriptor for Supported Metal Nanoparticles: Metal Chemical Potential. *ACS Catal* **11**, 8284–8291 (2021).
19. Campbell, C. T., Parker, S. C. & Starr, D. E. The effect of size-dependent nanoparticle energetics on catalyst sintering. *Science (1979)* **298**, 811–814 (2002).

20. Campbell, C. T. & Sellers, J. R. V. Anchored metal nanoparticles: Effects of support and size on their energy, sintering resistance and reactivity. *Faraday Discuss* **162**, 9–30 (2013).
21. Dai, Y., Lu, P., Cao, Z., Campbell, C. T. & Xia, Y. The physical chemistry and materials science behind sinter-resistant catalysts. *Chem Soc Rev* **47**, 4314–4331 (2018).
22. Stuckless, J. T., Starr, D. E., Bald, D. J. & Campbell, C. T. Metal adsorption calorimetry and adhesion energies on clean single-crystal surfaces. *Journal of Chemical Physics* **107**, 5547–5553 (1997).
23. Borroni-Bird, C. E., Al-Sarraf, N., Andersoon, S. & King, D. A. Single crystal adsorption microcalorimetry. *Chem Phys Lett* **183**, 516–520 (1991).
24. Dixon-Warren, St. J., Kovar, M., Wartnaby, C. E. & King, D. A. Pyroelectric single crystal adsorption microcalorimetry at low temperatures: oxygen on Ni100. *Surf Sci* **307–309**, 16–22 (1994).
25. Brown, W. A., Kose, R. & King, D. A. Femtomole Adsorption Calorimetry on Single-Crystal Surfaces. *Chem Rev* **98**, 797–832 (1998).
26. Stuck, A. *et al.* An improved single crystal adsorption calorimeter. *Surf Sci* **349**, 229–240 (1996).
27. Stuckless, J. T., Frei, N. A. & Campbell, C. T. A novel single-crystal adsorption calorimeter and additions for determining metal adsorption and adhesion energies. *Review of Scientific Instruments* **69**, 2427–2438 (1998).
28. Farmer, J. A., Baricuatro, J. H. & Campbell, C. T. Ag adsorption on reduced CeO2(111) thin films. *Journal of Physical Chemistry C* **114**, 17166–17172 (2010).
29. Rumptz, J. R., Mao, Z. & Campbell, C. T. Size-Dependent Adsorption and Adhesion Energetics of Ag Nanoparticles on Graphene Films on Ni(111) by Calorimetry. *ACS Catal* **12**, 2888–2897 (2022).
30. Feeley, G. M., Hemmingson, S. L. & Campbell, C. T. Energetics of Au Adsorption and Film Growth on Pt(111) by Single-Crystal Adsorption Calorimetry. *Journal of Physical Chemistry C* **123**, 5557–5561 (2019).
31. Larsen, J. H., Ranney, J. T., Starr, D. E., Musgrove, J. E. & Campbell, C. T. Adsorption energetics of Ag on MgO(100). *Phys Rev B Condens Matter Mater Phys* **63**, 1954101–1954108 (2001).
32. Janulaitis, N., Zhao, K. & Campbell, C. T. Energetics of Cu Adsorption on and Adhesion to Rutile-TiO2(100) Studied by Cu Vapor Adsorption Calorimetry. *The Journal of Physical Chemistry C* **128**, 16481–16490 (2024).
33. Hemmingson, S. L., James, T. E., Feeley, G. M., Tilson, A. M. & Campbell, C. T. Adsorption and Adhesion of Au on Reduced CeO2(111) Surfaces at 300 and 100 K. *Journal of Physical Chemistry C* **120**, 12113–12124 (2016).
34. James, T. E., Hemmingson, S. L., Ito, T. & Campbell, C. T. Energetics of Cu Adsorption and Adhesion onto Reduced CeO2(111) Surfaces by Calorimetry. *Journal of Physical Chemistry C* **119**, 17209–17217 (2015).
35. Mao, Z., Rumptz, J. R. & Campbell, C. T. Energetics of Ag Adsorption on and Adhesion to Rutile TiO 2 (100) Studied by Microcalorimetry. *Journal of Physical Chemistry C* **125**, 3036–3046 (2021).

36. Rumptz, J. R., Zhao, K., Mayo, J. & Campbell, C. T. Size-Dependent Energy of Ni Nanoparticles on Graphene Films on Ni (111) and Adhesion Energetics by Adsorption Calorimetry. *ACS Catal* **12**, 12632–12642 (2022).
37. Hemmingson, S. L. & Campbell, C. T. Trends in Adhesion Energies of Metal Nanoparticles on Oxide Surfaces: Understanding Support Effects in Catalysis and Nanotechnology. *ACS Nano* **11**, 1196–1203 (2017).
38. Zhao, K., Auerbach, D. J. & Campbell, C. T. Predicting Adhesion Energies of Catalytic Metal Nanoparticles to Support Surfaces, and Relating that to a Catalyst Performance Descriptor. *ACS Catal* **14**, 12857–12864 (2024).
39. Serp, Philippe. & Figueiredo, J. L. *Carbon Materials for Catalysis* . (John Wiley & Sons, Hoboken, N.J, 2009).
40. Rodríguez-reinoso, F. The role of carbon materials in heterogeneous catalysis. *Carbon N Y* **36**, 159–175 (1998).
41. Lam, E. & Luong, J. H. T. Carbon Materials as Catalyst Supports and Catalysts in the Transformation of Biomass to Fuels and Chemicals. *ACS Catal* **4**, 3393–3410 (2014).
42. Zhai, Y., Zhu, Z. & Dong, S. Carbon-Based Nanostructures for Advanced Catalysis. *ChemCatChem* **7**, 2806–2815 (2015).
43. Zheng, Y. *et al.* Toward design of synergistically active carbon-based catalysts for electrocatalytic hydrogen evolution. *ACS Nano* **8**, 5290–5296 (2014).
44. Xie, D. *et al.* Single-layer carbon-coated FeCo alloy nanoparticles embedded in single-walled carbon nanotubes for high oxygen electrocatalysis. *Chemical Communications* **56**, 6842–6845 (2020).
45. Tavakkoli, M. *et al.* Single-Shell Carbon-Encapsulated Iron Nanoparticles: Synthesis and High Electrocatalytic Activity for Hydrogen Evolution Reaction. *Angewandte Chemie - International Edition* **54**, 4535–4538 (2015).
46. Cui, W., Liu, Q., Cheng, N., Asiri, A. M. & Sun, X. Activated carbon nanotubes: a highly-active metal-free electrocatalyst for hydrogen evolution reaction. *Chemical Communications* **50**, 9340–9342 (2014).
47. Dribinskii, A. V, Tarasevich, M. R. & Kazarinov, V. E. Electrocatalysis on carbon materials. *Mater Chem Phys* **22**, 377–400 (1989).
48. Yan, Y. *et al.* A recent trend: application of graphene in catalysis. *Carbon Letters* **31**, 177–199 (2021).
49. Machado, B. F. & Serp, P. Graphene-based materials for catalysis. *Catal. Sci. Technol.* **2**, 54–75 (2012).
50. Zhou, X., Qiao, J., Yang, L. & Zhang, J. A Review of Graphene-Based Nanostructural Materials for Both Catalyst Supports and Metal-Free Catalysts in PEM Fuel Cell Oxygen Reduction Reactions. *Adv Energy Mater* **4**, 1301523-n/a (2014).
51. Huang, C., Li, C. & Shi, G. Graphene based catalysts. *Energy Environ. Sci.* **5**, 8848–8868 (2012).
52. Geim, A.K. ; Novoselov, K. S. The rise of graphene. *Nat Mater* **6**, 183–191 (2007).
53. Lee, D. W. & Yoo, B. R. Advanced metal oxide (supported) catalysts: Synthesis and applications. *Journal of Industrial and Engineering Chemistry* **20**, 3947–3959 (2014).

54. Kim, S. S., Lee, H. H. & Hong, S. C. The effect of the morphological characteristics of TiO2 supports on the reverse water–gas shift reaction over Pt/TiO2 catalysts. *Appl Catal B* **119–120**, 100–108 (2012).
55. Lu, Q., Zhang, Y., Tang, Z., Li, W. & Zhu, X. Catalytic upgrading of biomass fast pyrolysis vapors with titania and zirconia/titania based catalysts. *Fuel* **89**, 2096–2103 (2010).
56. Tian, H., Zhang, X. L., Scott, J., Ng, C. & Amal, R. TiO2-supported copper nanoparticles prepared via ion exchange for photocatalytic hydrogen production. *J Mater Chem A Mater* **2**, 6432–6438 (2014).
57. Panayotov, D. A., Frenkel, A. I. & Morris, J. R. Catalysis and Photocatalysis by Nanoscale Au/TiO2: Perspectives for Renewable Energy. *ACS Energy Lett* **2**, 1223–1231 (2017).
58. Obregón, S., Muñoz-Batista, M. J., Fernández-García, M., Kubacka, A. & Colón, G. Cu-TiO2 systems for the photocatalytic H2 production: Influence of structural and surface support features. *Appl Catal B* **179**, 468–478 (2015).
59. Colón, G., Maicu, M., Hidalgo, M. C. & Navío, J. A. Cu-doped TiO2 systems with improved photocatalytic activity. *Appl Catal B* **67**, 41–51 (2006).
60. Zhao, K., Auerbach, D. J. & Campbell, C. T. Low-Energy Ion Scattering Intensities from Supported Nanoparticles: The Spherical Cap Model. *Journal of Physical Chemistry C* **127**, 9129–9144 (2023).
61. Campbell, C. T. & James, T. E. Ion scattering spectroscopy intensities for supported nanoparticles: The hemispherical cap model. *Surf Sci* **641**, 166–169 (2015).
62. Schrader, M. E. Young-Dupre Revisited. *Langmuir* **9**, 3585–3589 (1995).
63. Zhao, K., Auerbach, D. J. & Campbell, C. T. Calorimetric Energies and Chemical Potentials of Metal Atoms in Catalytic Nanoparticles on Oxide and Carbon Supports: Improved Size Dependencies and Adhesion Energies. *ACS Catal* **13**, 13968–13981 (2023).
64. Sellers, J. R. V., James, T. E., Hemmingson, S. L., Farmer, J. A. & Campbell, C. T. Adsorption calorimetry during metal vapor deposition on single crystal surfaces: Increased flux, reduced optical radiation, and real-time flux and reflectivity measurements. *Review of Scientific Instruments* **84**, (2013).
65. Batzill, M. The surface science of graphene: Metal interfaces, CVD synthesis, nanoribbons, chemical modifications, and defects. *Surf Sci Rep* **67**, 83–115 (2012).
66. Guo, Q., Oh, W. S. & Goodman, D. W. Titanium oxide films grown on Mo(110). *Surf Sci* **437**, 49–60 (1999).
67. King, D. A. & Wells, M. G. Molecular beam investigation of adsorption kinetics on bulk metal targets: Nitrogen on tungsten. *Surf Sci* **29**, 454–482 (1972).
68. Calle-Vallejo, F., Koper, M. T. M. & Bandarenka, A. S. Tailoring the catalytic activity of electrodes with monolayer amounts of foreign metals. *Chem. Soc. Rev.* **42**, 5210–5230 (2013).
69. Zhou, Z., Gao, F. & Goodman, D. W. Deposition of metal clusters on single-layer graphene/Ru(0001): Factors that govern cluster growth. *Surf Sci* **604**, L31–L38 (2010).
70. Ouyang, R., Liu, J.-X. & Li, W.-X. Atomistic Theory of Ostwald Ripening and Disintegration of Supported Metal Particles under Reaction Conditions. *J Am Chem Soc* **135**, 1760–1771 (2013).
71. Roling, L. T. & Abild-Pedersen, F. Structure-Sensitive Scaling Relations: Adsorption Energies from Surface Site Stability. *ChemCatChem* **10**, 1643–1650 (2018).

72. Dean, J., Taylor, M. G. & Mpourmpakis, G. Unfolding adsorption on metal nanoparticles: Connecting stability with catalysis. *Sci Adv* **5**, eaax5101 (2019).
73. Fernández, E. M. *et al.* Scaling Relationships for Adsorption Energies on Transition Metal Oxide, Sulfide, and Nitride Surfaces. *Angewandte Chemie International Edition* **47**, 4683–4686 (2008).
74. Toebes, M. L., van Dillen, J. A. & de Jong, K. P. Synthesis of supported palladium catalysts. *J Mol Catal A Chem* **173**, 75–98 (2001).
75. Charreteur, F., Jaouen, F., Ruggeri, S. & Dodelet, J.-P. Fe/N/C non-precious catalysts for PEM fuel cells: Influence of the structural parameters of pristine commercial carbon blacks on their activity for oxygen reduction. *Electrochim Acta* **53**, 2925–2938 (2008).
76. Liu, H. *et al.* A review of anode catalysis in the direct methanol fuel cell. *J Power Sources* **155**, 95–110 (2006).
77. Zhang, Y. *et al.* Metal Particle Size and Structure of the Metal−Support Interface of Carbon-Supported Platinum Catalysts as Determined with EXAFS Spectroscopy. *J Phys Chem B* **108**, 18509–18519 (2004).
78. Baturina, O. A. *et al.* CO2 Electroreduction to Hydrocarbons on Carbon-Supported Cu Nanoparticles. *ACS Catal* **4**, 3682–3695 (2014).
79. Ali, A. & Shen, P. K. Recent advances in graphene-based platinum and palladium electrocatalysts for the methanol oxidation reaction. *J. Mater. Chem. A* **7**, 22189–22217 (2019).
80. Rao, R. G. *et al.* Oxygen-Doped Carbon Supports Modulate the Hydrogenation Activity of Palladium Nanoparticles through Electronic Metal–Support Interactions. *ACS Catal* **12**, 7344–7356 (2022).
81. Lustemberg, P. G. *et al.* Nature of the Active Sites on Ni/CeO2 Catalysts for Methane Conversions. *ACS Catal* **11**, 10604–10613 (2021).
82. Sokolova, A. *et al.* Sub-Monolayer Growth of Titanium, Cobalt, and Palladium on Epitaxial Graphene. *Ann Phys* **529**, 1700031 (2017).
83. Palacios-Lidón, E., Henry, C. R. & Barth, C. Kelvin probe force microscopy in surface chemistry: Reactivity of Pd nanoparticles on highly oriented pirolytic graphite. *ACS Catal* **4**, 1838–1844 (2014).
84. Motin, Md. A., Steiger-Thirsfeld, A., Stöger-Pollach, M. & Rupprechter, G. Model Catalysis with HOPG-Supported Pd Nanoparticles and Pd Foil: XPS, STM and C2H4 Hydrogenation. *Catal Letters* **152**, 2892–2907 (2022).
85. Khannanov, A. A., Valimukhametova, A. R., Kiiamov, A. G., Vakhitov, I. R. & Dimiev, A. M. The Mechanistic Details for the Growth of Palladium Nanoparticles on Graphene Oxide Support. *ChemistrySelect* **2**, 10546–10554 (2017).
86. Soy, E., Guisinger, N. P. & Trenary, M. Growth of Pd Nanoclusters on Single-Layer Graphene on Cu(111). *Journal of Physical Chemistry B* **122**, 572–577 (2018).
87. Gotterbarm, K. *et al.* Graphene-Templated Growth of Pd Nanoclusters. *Journal of Physical Chemistry C* **118**, 15934–15939 (2014).
88. Kettner, M., Stumm, C., Schwarz, M., Schuschke, C. & Libuda, J. Pd model catalysts on clean and modified HOPG : Growth, Adsorption Properties, and Stability. *Surf Sci* **679**, 64–73 (2019).

89. Lee, S., Kahng, S.-J. & Kuk, Y. Nano-level wettings of platinum and palladium on single-walled carbon nanotubes. *Chem Phys Lett* **500**, 82–85 (2010).
90. Agarwal, V., Aruna, I., Banerjee, V. & Mehta, B. R. Growth of palladium nanoparticles: An experimental and numerical study. *Phys Rev B* **74**, 35412 (2006).
91. Wintterlin, J. & Bocquet, M. L. Graphene on metal surfaces. *Surf Sci* **603**, 1841–1852 (2009).
92. Lahiri, J. *et al.* Graphene growth and stability at nickel surfaces. *New J Phys* **13**, (2011).
93. Sicot, M. *et al.* Nucleation and growth of nickel nanoclusters on graphene Moiré on Rh(111). *Appl Phys Lett* **96**, 093115 (2010).
94. Ernst, K. H., Ludviksson, A., Zhang, R., Yoshihara, J. & Campbell, C. T. Growth model for metal films on oxide surfaces: Cu on ZnO(0001)-O. *Phys Rev B* **47**, 13782–13796 (1993).
95. Campbell, C. T. Ultrathin metal films and particles on oxide surfaces: Structural, electronic and chemisorptive properties. *Surf Sci Rep* **27**, 1–111 (1997).
96. Venables, J. A. Atomic processes in crystal growth. *Surf Sci* **299–300**, 798–817 (1994).
97. Diebold, U., Pan, J. & Madey, T. E. Growth mode of ultrathin copper overlayers on TiO2(110). **47**, 3868–3876 (1993).
98. Hemmingson, S. L., Feeley, G. M., Miyake, N. J. & Campbell, C. T. Energetics of 2D and 3D Gold Nanoparticles on MgO(100): Influence of Particle Size and Defects on Gold Adsorption and Adhesion Energies. *ACS Catal* **7**, 2151–2163 (2017).
99. Brongersma, H. H., Draxler, M., de Ridder, M. & Bauer, P. Surface composition analysis by low-energy ion scattering. *Surf Sci Rep* **62**, 63–109 (2007).
100. Lytken, O. *et al.* Energetics of cyclohexene adsorption and reaction on Pt(111) by low-temperature microcalorimetry. *J Am Chem Soc* **130**, 10247–10257 (2008).
101. Alonso, J. A. & Lopez, M. J. Palladium clusters, free and supported on surfaces, and their applications in hydrogen storage. *Royal Society of Chemistry* **24**, 2729–2751 (2022).
102. Hu, L. *et al.* Density functional calculation of transition metal adatom adsorption on graphene. *Physica B Condens Matter* **405**, 3337–3341 (2010).
103. Gong, C. *et al.* First-principles study of metal – graphene interfaces. *J Appl Phys* **108**, 123711 (2010).
104. Cabria, I., López, M. J. & Alonso, J. A. Theoretical study of the transition from planar to three-dimensional structures of palladium clusters supported on graphene. *Phys Rev B* **81**, 035403 (2010).
105. Khomyakov, P. A. *et al.* First-principles study of the interaction and charge transfer between graphene and metals. *Phys Rev B* **79**, 195425 (2009).
106. Rêgo, C. R. C., Tereshchuk, P., Oliveira, L. N. & Da Silva, J. L. F. Graphene-supported small transition-metal clusters: A density functional theory investigation within van der Waals corrections. *Phys Rev B* **95**, 235422 (2017).
107. Cabria, I., López, M. J., Fraile, S. & Alonso, J. A. Adsorption and Dissociation of Molecular Hydrogen on Palladium Clusters Supported on Graphene. *The Journal of Physical Chemistry C* **116**, 21179–21189 (2012).
108. Gao, W., Mueller, J. E., Anton, J., Jiang, Q. & Jacob, T. Nickel Cluster Growth on Defect Sites of Graphene: A Computational Study. *Angewandte Chemie International Edition* **52**, 14237–14241 (2013).

109. Zhou, X., Chu, W., Sun, W., Zhou, Y. & Xue, Y. Enhanced interaction of nickel clusters with pyridinic-N (B) doped graphene using DFT simulation. *Comput Theor Chem* **1120**, 8–16 (2017).
110. Lausche, A. C. *et al.* On the effect of coverage-dependent adsorbate-adsorbate interactions for CO methanation on transition metal surfaces. *J Catal* **307**, 275–282 (2013).
111. Linstrom, P. & Mallard, W. The NIST Chemistry WebBook: A Chemical Data Resource on the Internet. (2001).
112. Mao, Z., Lustemberg, P. G., Rumptz, J. R., Ganduglia-Pirovano, M. V. & Campbell, C. T. Ni Nanoparticles on CeO2(111): Energetics, Electron Transfer, and Structure by Ni Adsorption Calorimetry, Spectroscopies, and Density Functional Theory. *ACS Catal* **10**, 5101–5114 (2020).
113. Mao, Z., Zhao, W., Al-Mualem, Z. A. & Campbell, C. T. Energetics and Structure of Nickel Atoms and Nanoparticles on MgO(100). *Journal of Physical Chemistry C* **124**, 14685–14695 (2020).
114. Liu, L. & Corma, A. Metal Catalysts for Heterogeneous Catalysis: From Single Atoms to Nanoclusters and Nanoparticles. *Chem Rev* **118**, 4981–5079 (2018).
115. Reier, T., Oezaslan, M. & Strasser, P. Electrocatalytic oxygen evolution reaction (OER) on Ru, Ir, and pt catalysts: A comparative study of nanoparticles and bulk materials. *ACS Catal* **2**, 1765–1772 (2012).
116. van Deelen, T. W., Hernández Mejía, C. & de Jong, K. P. Control of metal-support interactions in heterogeneous catalysts to enhance activity and selectivity. *Nat Catal* **2**, 955–970 (2019).
117. Gawande, M. B. *et al.* Cu and Cu-Based Nanoparticles: Synthesis and Applications in Catalysis. *Chem Rev* **116**, 3722–3811 (2016).
118. Chen, M. S. & Goodman, D. W. The Structure of Catalytically Active Gold on Titania. *Science (1979)* **306**, 252–255 (2004).
119. Parker, S. C. & Campbell, C. T. Kinetic model for sintering of supported metal particles with improved size-dependent energetics and applications to Au on TiO2 (110). *Phys Rev B Condens Matter Mater Phys* **75**, 1–15 (2007).
120. Boccuzzi, F., Guglielminotti, E., Martra, G. & Cerrato, G. Nitric Oxide Reduction by CO on Cu/TiO2 Catalysts. *J Catal* **146**, 449–459 (1994).
121. Díaz-Pérez, M. A., Moya, J., Serrano-Ruiz, J. C. & Faria, J. Interplay of Support Chemistry and Reaction Conditions on Copper Catalyzed Methanol Steam Reforming. *Ind Eng Chem Res* **57**, 15268–15279 (2018).
122. Dandekar, A. & Vannice, M. A. Determination of the Dispersion and Surface Oxidation States of Supported Cu Catalysts. *J Catal* **178**, 621–639 (1998).
123. Pena, D. A., Uphade, B. S. & Smirniotis, P. G. TiO2-supported metal oxide catalysts for low-temperature selective catalytic reduction of NO with NH3. I. Evaluation and characterization of first row transition metals. *J Catal* **221**, 421–431 (2004).
124. Rodriguez, J. A. *et al.* Hydrogenation of CO 2 to Methanol: Importance of Metal–Oxide and Metal–Carbide Interfaces in the Activation of CO 2. *ACS Catal* **5**, 6696–6706 (2015).
125. Vaughan, O. P. H., Kyriakou, G., Macleod, N., Tikhov, M. & Lambert, R. M. Copper as a selective catalyst for the epoxidation of propene. *J Catal* **236**, 401–404 (2005).

126. Behrens, M. *et al.* The Active Site of Methanol Synthesis over Cu/ZnO/Al2O3 Industrial Catalysts. *Science (American Association for the Advancement of Science)* **336**, 893–897 (2012).
127. Gokhale, A. A., Dumesic, J. A. & Mavrikakis, M. On the Mechanism of Low-Temperature Water Gas Shift Reaction on Copper. *J Am Chem Soc* **130**, 1402–1414 (2008).
128. Grabow, L. C. & Mavrikakis, M. Mechanism of methanol synthesis on cu through CO2 and CO hydrogenation. *ACS Catal* **1**, 365–384 (2011).
129. Graciani, J. *et al.* Highly active copper-ceria and copper-ceria-titania catalysts for methanol synthesis from CO2. *Science (American Association for the Advancement of Science)* **345**, 546–550 (2014).
130. Kattel, S., Ramírez, P. J., Chen, J. G., Rodriguez, J. A. & Liu, P. Active sites for CO 2 hydrogenation to methanol on Cu/ZnO catalysts. *Science (American Association for the Advancement of Science)* **355**, 1296–1299 (2017).
131. Li, M. *et al.* The Influence of the Bulk Reduction State on the Surface Structure and Morphology of Rutile TiO2(110) Single Crystals. *Journal of Physical Chemistry B* **104**, 4944–4950 (2000).
132. Porosoff, M. D., Yan, B. & Chen, J. G. Catalytic reduction of CO 2 by H 2 for synthesis of CO, methanol and hydrocarbons: challenges and opportunities. *Energy Environ Sci* **9**, 62–73 (2016).
133. Rodriguez, J. A., Liu, P., Hrbek, J., Evans, J. & Pérez, M. Water Gas Shift Reaction on Cu and Au Nanoparticles Supported on CeO 2 (111) and ZnO(000$\bar 1$): Intrinsic Activity and Importance of Support Interactions. *Angewandte Chemie International Edition* **46**, 1329–1332 (2007).
134. Ahmadi, M., Mistry, H. & Cuenya, B. R. Tailoring the Catalytic Properties of Metal Nanoparticles via Support Interactions. (2016) doi:10.1021/acs.jpclett.6b01198.
135. Zhao, K., Janulaitis, N., Rumptz, J. R. & Campbell, C. T. Size-Dependent Energy and Adhesion of Pd Nanoparticles on Graphene on Ni(111) by Pd Vapor Adsorption Calorimetry. *ACS Catal* **13**, 2670–2680 (2023).
136. Bagheri, S., Muhd Julkapli, N. & Bee Abd Hamid, S. Titanium dioxide as a catalyst support in heterogeneous catalysis. *Scientific World Journal* **2014**, (2014).
137. Zhang, L., Cosandey, F., Persaud, R. & Madey, T. E. Initial growth and morphology of thin Au films on TiO2(110). *Surf Sci* **439**, 73–85 (1999).
138. Lazzari, R., Renaud, G., Jupille, J. & Leroy, F. Self-similarity during growth of the Au/TiO2(110) model catalyst as seen by the scattering of x-rays at grazing-angle incidence. *Phys Rev B* **76**, 125412 (2007).
139. Hemmingson, S. L., Feeley, G. M., Miyake, N. J. & Campbell, C. T. Energetics of 2D and 3D Gold Nanoparticles on MgO(100): Influence of Particle Size and Defects on Gold Adsorption and Adhesion Energies. *ACS Catal* **7**, 2151–2163 (2017).
140. Rumptz, J. R., Zhao, K., Mayo, J. & Campbell, C. T. Size-Dependent Energy of Ni Nanoparticles on Graphene Films on Ni(111) and Adhesion Energetics by Adsorption Calorimetry. *ACS Catal* **12**, 12632–12642 (2022).
141. Mao, Z., Zhao, W., Al-Mualem, Z. A. & Campbell, C. T. Energetics and Structure of Nickel Atoms and Nanoparticles on MgO(100). *Journal of Physical Chemistry C* **124**, 14685–14695 (2020).

142. James, T. E., Hemmingson, S. L. & Campbell, C. T. Energy of Supported Metal Catalysts: From Single Atoms to Large Metal Nanoparticles. *ACS Catal* **5**, 5673–5678 (2015).
143. Ranney, J. T., Starr, D. E., Musgrove, J. E., Bald, D. J. & Campbell, C. T. A microcalorimetric study of the heat of adsorption of copper on well-defined oxide thin film surfaces: MgO(100), p(2 × 1) oxide on Mo(100) and disordered W oxide. *Faraday Discuss* **114**, 195–208 (1999).
144. *CRC Handbook of Chemistry and Physics*. (CRC Press, Boston, 2014).
145. Farmer, J. A. & Campbell, C. T. Ceria Maintains Smaller Metal Catalyst Particles by Strong Metal-Support Bonding. *Science (1979)* **329**, 933–936 (2010).
146. Vitos, L., Ruban, A. V, Skriver, H. L. & Kollár, J. The surface energy of metals. *Surf Sci* **411**, 186–202 (1998).
147. Aoki, T., Mitsuhara, K. & Takizawa, M. Growth mode analysis of Cu Nanoparticles on Rutile TiO2(110). *e-Journal of Surface Science and Nanotechnology* **16**, 225–228 (2018).
148. Chen, D. A., Bartelt, M. C., Hwang, R. Q. & McCarty, K. F. Self-limiting growth of copper islands on TiO2(110)-(1×1). *Surf Sci* **450**, 78–97 (2000).
149. Zhou, J., Kang, Y. C. & Chen, D. A. Controlling island size distributions: A comparison of nickel and copper growth on TiO2(1 1 0). *Surf Sci* **537**, (2003).
150. Venables, J. A. Introduction to Surface and Thin Film Processes. *Introduction to Surface and Thin Film Processes* (2000) doi:10.1017/cbo9780511755651.
151. Hu, S. & Li, W. X. Sabatier principle of metal-support interaction for design of ultrastable metal nanocatalysts. *Science (1979)* **374**, 1360–1365 (2021).
152. Pillay, D., Wang, Y. & Hwang, G. S. A comparative theoretical study of Au, Ag and Cu adsorption on TiO 2 (110) rutile surfaces. *Korean Journal of Chemical Engineering* **21**, 537–547 (2004).
153. Giordano, L., Pacchioni, G., Bredow, T. & Sanz, J. F. Cu, Ag, and Au atoms adsorbed on TiO2(1 1 0): Cluster and periodic calculations. *Surf Sci* **471**, 21–31 (2001).
154. Winterbottom, W. L. Equilibrium shape of a small particle in contact with a foreign substrate. *Acta Metallurgica* **15**, 303–310 (1967).
155. Campbell, C. T. & Sellers, J. R. V. Anchored metal nanoparticles: Effects of support and size on their energy, sintering resistance and reactivity. *Faraday Discuss* **162**, 9–30 (2013).
156. Zhao, K., Auerbach, D. J. & Campbell, C. T. Predicting Adhesion Energies of Catalytic Metal Nanoparticles to Support Surfaces, and Relating that to a Catalyst Performance Descriptor. *ACS Catalysis. Submitted.*
157. Janulaitis, N. & Campbell, C. T. Trends for predicting adhesion energies of late transition metals on oxide surfaces. *In Progress* (2024).
158. O'Connor, N. J., Jonayat, A. S. M., Janik, M. J. & Senftle, T. P. Interaction trends between single metal atoms and oxide supports identified with density functional theory and statistical learning. *Nat Catal* **1**, 531–539 (2018).
159. Pérez-Bailac, P., Lustemberg, P. G. & Ganduglia-Pirovano, M. V. Facet-dependent stability of near-surface oxygen vacancies and excess charge localization at CeO2 surfaces. *Journal of Physics Condensed Matter* **33**, 504003 (2021).

160. Richter, N. A., Sicolo, S., Levchenko, S. V., Sauer, J. & Scheffler, M. Concentration of vacancies at metal-oxide surfaces: Case study of MgO(100). *Phys Rev Lett* **111**, 1–5 (2013).
161. Morgan, B. J. & Watson, G. W. A density functional theory + u study of Oxygen vacancy formation at the (110), (100), (101), and (001) surfaces of rutile TiO2. *Journal of Physical Chemistry C* **113**, 7322–7328 (2009).
162. Curnan, M. T. & Kitchin, J. R. Effects of concentration, crystal structure, magnetism, and electronic structure method on first-principles oxygen vacancy formation energy trends in perovskites. *Journal of Physical Chemistry C* **118**, 28776–28790 (2014).
163. Wexler, R. B., Gautam, G. S., Stechel, E. B. & Carter, E. A. Factors Governing Oxygen Vacancy Formation in Oxide Perovskites. *J Am Chem Soc* **143**, 13212–13227 (2021).
164. Pérez-Bailac, P., Lustemberg, P. G. & Ganduglia-Pirovano, M. V. Facet-dependent stability of near-surface oxygen vacancies and excess charge localization at CeO2surfaces. *Journal of Physics Condensed Matter* **33**, (2021).
165. O'Connor, N. J., Jonayat, A. S. M., Janik, M. J. & Senftle, T. P. Interaction trends between single metal atoms and oxide supports identified with density functional theory and statistical learning. *Nat Catal* **1**, 531–539 (2018).
166. Morgan, B. J. & Watson, G. W. A density functional theory + u study of Oxygen vacancy formation at the (110), (100), (101), and (001) surfaces of rutile TiO2. *Journal of Physical Chemistry C* **113**, 7322–7328 (2009).
167. Richter, N. A., Sicolo, S., Levchenko, S. V., Sauer, J. & Scheffler, M. Concentration of vacancies at metal-oxide surfaces: Case study of MgO(100). *Phys Rev Lett* **111**, 1–5 (2013).
168. Cheng, H. & Selloni, A. Surface and subsurface oxygen vacancies in anatase TiO2 and differences with rutile . *Phys Rev B* **79**, 2–5 (2009).
169. Feng, Y., Wang, N., Guo, X. & Zhang, S. Characteristics of dopant distribution and surface oxygen vacancy formation for modified Fe2O3 in chemical looping combustion. *Fuel* **276**, 117942 (2020).
170. Lazzari, R., Renaud, G., Revenant, C., Jupille, J. & Borensztein, Y. Adhesion of growing nanoparticles at a glance: Surface differential reflectivity spectroscopy and grazing incidence small angle x-ray scattering. *Phys Rev B* **79**, 125428 (2009).
171. Revenant, C., Renaud, G., Lazzari, R. & Jupille, J. Defect-pinned nucleation, growth, and dynamic coalescence of Ag islands on MgO(001): An in situ grazing-incidence small-angle x-ray scattering study. *Phys Rev B* **79**, 235424 (2009).
172. Trampert, A., Ernst, F., Flynn, C. P., Fischmeister, H. F. & Ru¨hle, M. High resolution transmission electron microscopy studies of the Ag/MgO interface. *Acta Metallurgica et Materialia* **40**, S227–S236 (1992).
173. Giorgio, S., Cabié, M. & Henry, C. R. Dynamic observations of Au catalysts by environmental electron microscopy. *Gold Bull* **41**, 167–173 (2008).
174. Graoui, H., Giorgio, S. & Henry, C. R. Shape variations of Pd particles under oxygen adsorption. *Surf Sci* **58**, 289–384 (1998).
175. Renaud, G. Real-Time Monitoring of Growing Nanoparticles by in situ Small Angle Grazing Incidence X-Ray Scattering. *AIP Conf Proc* **748**, 63–71 (2005).

176. Revenant, C., Leroy, F., Lazzari, R., Renaud, G. & Henry, C. R. Quantitative analysis of grazing incidence small-angle x-ray scattering: Pd/MgO(001) growth. *Phys Rev B* **69**, 35411 (2004).
177. Olander, J. *et al.* Size- and temperature-dependent epitaxy for a strong film-substrate mismatch: The case of $\mathrm{Pt}/\mathrm{Mg}\mathrm{O}(001)$. *Phys Rev B* **76**, 75409 (2007).
178. Janulaitis, N., Zhao, K. & Campbell, C. T. Energetics of Cu adsorption on and adhesion to rutile-TiO2(100) studied by Cu vapor adsorption calorimetry. *Journal of Physical Chemistry, In Review* (2024).
179. Lazzari, R. *et al.* Plasmonics of Supported Nanoparticles Reveals Adhesion at the Nanoscale: Implications for Metals on Dielectrics. *ACS Appl Nano Mater* **3**, 12157–12168 (2020).
180. Lazzari, R. *et al.* Surface and Epitaxial Stresses on Supported Metal Clusters. *Nano Lett* **16**, 2574–2579 (2016).
181. Jensen, M. C. R. *et al.* Morphology, dispersion, and stability of Cu nanoclusters on clean and hydroxylated α-Al2O3(0001) substrates. *Journal of Physical Chemistry C* **112**, 16953–16960 (2008).
182. Wellendorff, J. *et al.* A benchmark database for adsorption bond energies to transition metal surfaces and comparison to selected DFT functionals. *Surf Sci* **640**, 36–44 (2015).
183. Zhao, W., Carey, S. J., Morgan, S. E. & Campbell, C. T. Energetics of adsorbed formate and formic acid on Ni(111) by calorimetry. *J Catal* **352**, 300–304 (2017).
184. Carey, S. J., Zhao, W., Mao, Z. & Campbell, C. T. Energetics of Adsorbed Phenol on Ni(111) and Pt(111) by Calorimetry. *The Journal of Physical Chemistry C* **123**, 7627–7632 (2019).
185. Lew, W., Crowe, M. C., Karp, E. & Campbell, C. T. Energy of Molecularly Adsorbed Water on Clean Pt(111) and Pt(111) with Coadsorbed Oxygen by Calorimetry. *The Journal of Physical Chemistry C* **115**, 9164–9170 (2011).
186. Silbaugh, T. L., Karp, E. M. & Campbell, C. T. Energetics of Formic Acid Conversion to Adsorbed Formates on Pt(111) by Transient Calorimetry. *J Am Chem Soc* **136**, 3964–3971 (2014).
187. Lew, W. *et al.* The Energy of Adsorbed Hydroxyl on Pt(111) by Microcalorimetry. *The Journal of Physical Chemistry C* **115**, 11586–11594 (2011).
188. Campbell, C. T. Energies of Adsorbed Catalytic Intermediates on Transition Metal Surfaces: Calorimetric Measurements and Benchmarks for Theory. *Acc Chem Res* **52**, 984–993 (2019).
189. Zhao, W., Carey, S. J., Mao, Z. & Campbell, C. T. Adsorbed Hydroxyl and Water on Ni(111): Heats of Formation by Calorimetry. *ACS Catal* **8**, 1485–1489 (2018).
190. Carey, S. J., Zhao, W. & Campbell, C. T. Bond Energies of Adsorbed Intermediates to Metal Surfaces: Correlation with Hydrogen–Ligand and Hydrogen–Surface Bond Energies and Electronegativities. *Angewandte Chemie International Edition* **57**, 16877–16881 (2018).
191. Silbaugh, T. L. & Campbell, C. T. Energies of Formation Reactions Measured for Adsorbates on Late Transition Metal Surfaces. *The Journal of Physical Chemistry C* **120**, 25161–25172 (2016).

192. Bligaard, T. *et al.* Toward Benchmarking in Catalysis Science : Best Practices , Challenges , and Opportunities. *ACS Catal* **6**, 2590–2602 (2016).
193. Karp, E. M., Silbaugh, T. L., Crowe, M. C. & Campbell, C. T. Energetics of adsorbed methanol and methoxy on Pt(111) by microcalorimetry. *J Am Chem Soc* **134**, 20388–20395 (2012).
194. Ruehl, G., Harman, S. E., Árnadóttir, L. & Campbell, C. T. Acetonitrile Adsorption and Adhesion Energies onto the Pt(111) Surface by Calorimetry. *ACS Catal* **12**, 156–163 (2022).
195. Karp, E. M., Campbell, C. T., Studt, F., Abild-Pedersen, F. & Norskov, J. K. Energetics of oxygen adatoms, hydroxyl species and water dissociation on Pt(111). *Journal of Physical Chemistry C* **116**, 25772–25776 (2012).
196. Carey, S. J. *et al.* Energetics of Adsorbed Methanol and Methoxy on Ni(111): Comparisons to Pt(111). *ACS Catal* **8**, 10089–10095 (2018).
197. Carey, S. J., Zhao, W. & Campbell, C. T. Energetics of adsorbed benzene on Ni(111) and Pt(111) by calorimetry. *Surf Sci* **676**, 9–16 (2018).
198. Ruehl, G., Harman, S. E., Gluth, O. M., LaVoy, D. H. & Campbell, C. T. Energetics of Adsorbed Formate and Formic Acid on Cu(111) by Calorimetry. *ACS Catal* **12**, 10950–10960 (2022).
199. Ajo, H. M., Ihm, H., Moilanen, D. E. & Campbell, C. T. Calorimeter for adsorption energies of larger molecules on single crystal surfaces. *Review of Scientific Instruments* **75**, 4471–4480 (2004).
200. Lew, W., Lytken, O., Farmer, J. A., Crowe, M. C. & Campbell, C. T. Improved pyroelectric detectors for single crystal adsorption calorimetry from 100 to 350 K. *Review of Scientific Instruments* **81**, 1–9 (2010).
201. Lytken, O., Lew, W. & Campbell, C. T. Catalytic reaction energetics by single crystal adsorption calorimetry: hydrocarbons on Pt(111). *Chem Soc Rev* **37**, 2172–2179 (2008).
202. Campbell, C. T. Future Directions and Industrial Perspectives Micro- and macro-kinetics: Their relationship in heterogeneous catalysis. *Top Catal* **1**, 353–366 (1994).
203. Campbell, C. T. The Degree of Rate Control: A Powerful Tool for Catalysis Research. *ACS Catal* **7**, 2770–2779 (2017).
204. Che, M. Nobel Prize in chemistry 1912 to Sabatier: organic chemistry or catalysis? *Catal Today* **218**, 162–171 (2013).
205. Sabatier, P. *La Catalyse En Chimie Organique*. vol. 3 (C. Béranger, 1920).
206. Stegelmann, C., Andreasen, A. & Campbell, C. T. Degree of rate control: How much the energies of intermediates and transition states control Rates. *J Am Chem Soc* **131**, 13563 (2009).
207. Mao, Z. & Campbell, C. T. Apparent Activation Energies in Complex Reaction Mechanisms: A Simple Relationship via Degrees of Rate Control. *ACS Catal* **9**, 9465–9473 (2019).
208. Mao, Z. & Campbell, C. T. Kinetic Isotope Effects: Interpretation and Prediction Using Degrees of Rate Control. *ACS Catal* **10**, 4181–4192 (2020).
209. Campbell, C. T. & Mao, Z. Analysis and prediction of reaction kinetics using the degree of rate control. *J Catal* **404**, 647–660 (2021).

210. Wolcott, C. A., Medford, A. J., Studt, F. & Campbell, C. T. Degree of rate control approach to computational catalyst screening. *J Catal* **330**, 197–207 (2015).
211. Wang, S. *et al.* Universal transition state scaling relations for (de)hydrogenation over transition metals. *Physical Chemistry Chemical Physics* **13**, 20760–20765 (2011).
212. Montemore, M. M. & Medlin, J. W. Scaling relations between adsorption energies for computational screening and design of catalysts. *Catal Sci Technol* **4**, 3748–3761 (2014).
213. Xu, Y. *et al.* In silico search for novel methane steam reforming catalysts. *New J Phys* **15**, (2013).
214. Medford, A. J. *et al.* CatMAP: A Software Package for Descriptor-Based Microkinetic Mapping of Catalytic Trends. *Catal Letters* **145**, 794–807 (2015).
215. Howard Shomate, B. C. A Method for Evaluating and Correlating Thermodynamic Data. *J Phys Chem* **58**, 35 (1954).
216. Norskov, Jens K.; Abild-Pedersen, Frank; Studt, Felix; Bligaard, T. Density functional theory in surface chemistry and catalysis. *Proceedings of the National Academy of Sciences* **108**, 2017 (2017).
217. Motagamwala, A. H. & Dumesic, J. A. Analysis of reaction schemes using maximum rates of constituent steps. *Proc Natl Acad Sci U S A* **113**, E2879–E2888 (2016).
218. Baz, A. & Holewinski, A. Predicting macro-kinetic observables in electrocatalysis using the generalized degree of rate control. *J Catal* **397**, 233–244 (2021).
219. Mao, Z. & Campbell, C. T. The degree of rate control of catalyst-bound intermediates in catalytic reaction mechanisms: Relationship to site coverage. *J Catal* **381**, 53–62 (2020).